J. Bangladesh Acad. Sci. Volume 50, Issue 1, March 2026

ISSN 2224-7270 (Online), 0378-8121 (Print)

Journal of Bangladesh Academy of Sciences is published four times a year (March, June, September and December comprising one volume) in English. Original research articles, review articles, and short communications of all branches of Science and Technology are considered for publication in this journal. Review articles are generally by invitation.

Disclaimer

The opinions, analysis and conclusions expressed or implied in this journal are those of the authors and do not represent the views of Bangladesh Academy of Sciences.

Submission

All correspondence regarding contributions for publication in the journal should be addressed to the *Editor, Journal of Bangladesh Academy of Sciences* <jbas.editor@yahoo.com>. Authors should consult the contributor's guideline at the back of the journal before submitting their manuscripts.

Published by

Bangladesh Academy of Sciences, National Science and Technology Complex, Agargaon, Dhaka-1207.

Design and Printed by

Sucharu Desktop Publishing, 1/E/1, Paribagh, Dhaka-1000, Bangladesh

Annual Subscription: Tk. 500.00 (Bangladesh); US $ 60.00; £ 21.50 plus postage.

Single Copy: Tk. 250.00 (Bangladesh); US $ 30.00; £ 11.25 plus postage.

J. Bangladesh Acad. Sci. 46(2); 129-134: December 2022 DOI: 10.3329/jbas.v46i2.63414

Journal of Bangladesh Academy of Sciences

Journal homepage: http://www.bas.org.bd/publications/jbas.html

Review Article

Health and Environment*

Qazi Kholiquzzaman Ahmad

ABSTRACT

Bangladesh is passing through the dividend phase of demographic transition, with 45 million (over a quarter of the total population) in the age group of 15-29 years and 52.8 million (about a third) in the 15-36 age group. Young scientists belong to the upper segments of the later age group (some may be somewhat older than 36), who will in the fullness of time, take up leadership positions in their respective fields. Whatever be the field of human endeavour, the capability of the protagonists, is certainly a pivotal key to success. Indeed, human capability depends on education, skill training and health services. The better the availability of these services, the better is expected to be the ability acquired by the people concerned. One of these key services, health, is included in the theme of this conference. This paper has proposed that a universal health coverage (UHC) system be developed in Bangladesh so that people from all walks of life can access at least primary health services. The UHC can be developed centering around the 14,000 or so Community Clinics in place all around rural Bangladesh. Bangladesh is pursuing the goal of sustainable development within the UN adopted 2030 Agenda for Sustainable Development framework. This agenda is anchored on three pillars-economic, social and environmental. Sustainable development can be succinctly defined as socially acceptable, environmentally sound economic growth. Also, a basic tenet characterising sustainable development is that nobody can be left behind, i.e., everybody has to be included. The theme of this conference consist of the environmental pillar of sustainable development. In fact, the environment is the ultimate resource base of all development. Climate change, a major sub-set of environmental issues, is fast deteriorating and becoming an existential threat to humanity. This paper has discussed what has been happening in relation to climate change and what is being done to combat the menace globally and in Bangladesh. The efforts of Bangladesh in policy, programming, funding, and action in the context of responding to the increasingly adverse impacts on the country caused by the worsening climate change have been reviewed. Also, since this problem is global and cannot be adequately combatted by any one country, much less by a resource-poor country like Bangladesh, what role the international community is playing in this regard has been examined. The final section relates the lessons from the above discussions and reviews the future roles that young scientists need to play.

Introduction

Bangladesh has been making major strides over the past decade or so in terms of economic growth (GDP growth and per capita income), ICT penetration, major infrastructural development (e.g., Padma Bridge, soon to be operational Karnafuli Tunnel, soon to be operational Dhaka Metro-rail, road networks) as well as in relation to certain key social indicators such as infant, child and maternal mortality, women's empowerment, poverty reduction and spread of education. These achievements are widely recognized internationally. Bangladesh is also one of the few countries in the world which have managed covid-19 pandemic fairly well, both health-wise and in addressing the economic upheavals it caused. A potential food crisis was averted and, after initial fumbling, vaccination, testing for corona, hospitalization and treatment services improved fast and significantly. The pandemic has been almost completely overcome as all who, including children of 6 years, should be vaccinated have received at least one dose and mostly two doses. Also, a notable proportion has received a third (booster) dose.

Post-covid-19 economic recovery started strongly, with the GDP growth rate reaching 7.25 percent in fiscal 2022 and the rural economy (agriculture and non-agriculture) starting to rejuvenate. A dampening impact of the global economic turmoil caused by the Ukraine War occurring on the heels of the covid-19 pandemic is faced by Bangladesh and other countries

*The author may be reached at <qk_ahmad@yahoo.com>

Theme Lecture of 5th Young Scientist Congress, organized by Bangladesh Academy of Sciences, 25th November, 2022

worldwide. Policy and action programmes are afoot in the country to address the issues faced at both micro and macro levels, designed with a view to responding to the realities unfolding. An example is the various steps taken to boost foreign exchange receipts, such as boosting exports and inward remittances on the one hand and appropriately reducing foreign exchange use through cutting down unnecessary or less important imports, the incidence of foreign travel that can be avoided, controlling over-invoicing and under-invoicing practices by certain importers and exporters. Also, there are policy and financial support being provided to encourage increased food production.

Our development goals include achieving sustainable development, particularly the 39+1 targets prioritized by the government by 2030 and reaching higher-middle income status by 2031 and a developed country status by 2041. It may be noted here that sustainable development is socially acceptable, environmentally sound economic growth. A basic tenet of the process is that everybody has to be included.

These goals can be achieved if we can effectively address the problems now faced, some of which have been indicated above, and others that may exist or arise as we go forward. And one of the key elements for the trajectories underpinned by the goals envisaged to be successfully pursued is the availability of adequately qualified, trained, and motivated work forces for various sectors. That is, human capabilities of various levels for each sector need to be developed based on needs assessment in each sector as of now and projected for future years as we move forward.

Human capabilities are dependent on education, skill training and health services. Therefore, access to quality education, skill training and appropriate health services must be ensured for all concerned, particularly the youth, to ensure the supplies of the capabilities required in various sectors as we move forward.

Demographic Dividend

Demographic dividend in terms of economic growth potential is obtainable when the share of the working-age population is larger than the share of the non-working-age population. It is particularly potent when youth preponderates in the population's age structure. This is still the reality in Bangladesh, although the proportion of the youth will start declining soon and will, by 2050, be lower than that of the elderly population (aged 60 and above).

The working-age population (15-64 years of age) currently constitutes about 66% of the total population. About 24 percent of the total population (about 45 million) in Bangladesh is aged between 15 and 29 years and about a third is aged between 15 and 36 (about 52.8 million) (BBS, 2022).

Today in this conference, we are focusing on youth scientists who belong to the age group which is the highest potential segment of the population in terms of demographic dividend.

The young scientists are likely to be aged 24 to 36, and some may be a little older than 36. There are, millions more belonging to this age group who are either poorly and scantly educated or illiterate or have received education and have skills that do not correspond to the human capabilities required in different sectors of the economy and society. Hence, there is widespread youth unemployment and underemployment in the country, including educated youth. For the economy to benefit from the dividend phase of the demographic transition till it lasts, it is crucial that the youths are properly trained and facilitated to find worthwhile jobs to contribute to their own and national development. The government has several programmes in this context. There are also some private sector undertakings. But, these are altogether grossly inadequate for the task at hand. Much more attention in terms of facilitating and enabling the youth is needed to make the best possible use of the high potential that exists. Let me turn to the issue of health services, which is included in theme of this conference.

Health Services in Bangladesh: A Brief Review and a Proposal

A remarkable improvement in private health services has occurred in the country, particularly in urban

areas, over the past two decades. But, not infrequently, these services are of uncertain quality. Being very expensive, these services are usually beyond the reach of ordinary people.

Public health services have also expanded in the country regarding diagnostic and hospital facilities in urban and rural areas, for example, Upazila Health Complexes and Community Clinics. But, still, public health services in the country are grossly inadequate and fragmented. A study has found that, even in Dhaka city, of those who sought healthcare services, 39 percent sought it from pharmacies, 34 percent from private providers, only 13.6 percent from public healthcare facilities, and others went to traditional or different non-registered sources (Sarker et. al., 2022). In fact, the majority of health service expenses are borne by the people (patients), often referred to as out-of-pocket or OOP expenses. The OOP expenses account for 67 percent of total medical expenses in Bangladesh as of 2015. Poor and low-income households cannot meet such expenses. They cannot, therefore, avail of essential health services or manage the required expenses by borrowing from others, using family savings, donations from relatives and others, or taking bank loans when possible. An estimated five million people face dire consequences on account of not being able to avail of essential medical services or doing so by incurring heavy debts. (Sarker et al., 2022)

To strengthen and universalize the country's healthcare system, the Government of Bangladesh prepared a proposal in 2012 for expanding social protection for health towards universal coverage by 2032 (MoH&FW, 2012)

To meet the challenges and increase financial protection for the entire population and reduce OOP, the following three strategies were proposed:

a) Generate more resources for effective health services;

b) Improve equity and increase healthcare access, especially for the poor and vulnerable; and

c) Enhance efficiency in resource allocation and nationalization.

The proposal was to start with the poor and the formal sector and then expand the coverage to informal sectors leading to universal coverage by 2032. It may be recalled here that Prime Minister Sheikh Hasina reiterated her commitment to establish Universal Health Coverage (UHC) in Bangladesh at a High Level UN meeting on UHC in New York in 2019.

But, the 2012 proposal clearly has not been acted upon. Also, the Prime Minister's commitment is yet to be put on stream. In reality, an annual budgetary allocation to the health sector has remained well below one percent of the GDP. Moreover, the management capacity of the government has remained so limited that even this meager allocation could not usually be spent over the past years. Then there is also often a question mark regarding the quality of spending.

The covid-19 pandemic has brought home sharply the gross inadequacy of public health services, particularly primary healthcare services, in the country, reinforcing the need for UHC. I strongly suggest that the UHC process be started on an urgent basis. There is already an infrastructural basis in terms of the 14,000 or so Community Clinics in rural areas across the country. Also, there are Upazila Health Complexes to be taped.

For a UHC process to be perused, mobilization of financial resources and strengthening of government health sector management capacity as well as the availability of an adequate number of medical doctors, nurses, technicians, and other health workers will be essential. Moreover, it will need to be ensured through appropriate incentives and administrative steps that doctors and other health services providers work in urban and rural areas, as required. However, above all, it is crucial that there is a political will to follow through on the commitment of the Prime Minister to UHC and that the process is initiated without further delay of time.

It will be more efficient and politically prudent to cover the total population simultaneously rather than starting with the poor and formal sector people and

then extend to the informal sector as proposed in the strategy proposed in 2012.

At the present level of GDP in Bangladesh, the establishment of UHC is affordable. Available estimates show that an additional annual budgetary allocation of one percent of the GDP will suffice to pursue the establishment of UHC in the country (Chowdhury and Yates, 2022).

Now let us briefly discuss aspects of the environment which are also included in the conference's theme.

Environment and Climate Change

The environment is one of the three pillars of the UN-adopted 2030 Agenda for Sustainable Development – the other two being economical and social development.

The broad areas of concern here are environmental degradation (deterioration in the integrity of the environment as a result of concentrations of various pollutants and other activities and processes such as deforestation, improper land use, and natural disasters), bio-diversity loss (losses in the number, genetic variety, variety of species, biological communities in given access-on land and in water bodies and oceans) and climate change (long term, at least 30 years) shifts in temperatures and weather patterns, which may be natural such as through variations in the solar cycle but also, as a result of human activities, such as the burning of fossil fuels, emitting greenhouse gases (GHGs), which constitute the main driver of the ongoing climate change.

These are now burning and further worsening natural phenomena causing upheavals in human lives and living and economic prospects around the world. In particular, climate change has assumed the proportion of existential threat to humanity and even to the planet earth.

As a consequence of the increasing concentration of GHGs in the atmosphere, the earth has been warming (global warming) causing increasing (both in terms of frequency and devastation) natural disasters such as floods, cyclones, sea level rise, and storm surges, heat waves, droughts and so on. These are happening worldwide in both developed and developing countries. But certain countries are particularly vulnerable due to their geographical location and poor ability to respond. Bangladesh is at the forefront of the countries in this category. But, Bangladesh is not at all responsible for global climate change as it emits an insignificant amount GHGs in the global context. Yet, it's one of the worst sufferers due to natural disasters attributable to climate change.

Since climate change is a global issue, it can be effectively addressed by an effective corporative regime globally based on the principle of common but differentiated responsibilities and respective capabilities. Otherwise, the downward slide will continue to intensify, imperiling humanity.

A country like Bangladesh with limited climate adaptive capacity (financial and technological) needs support from the international community to address the climate change impacts. But very little financial support is available not only for Bangladesh but for developing countries in general. The international community promised to provide climate finance of US$ 100 billion annually with effect from 2020. But even now, an Oxfam study shows, only about US$ 20 billion is now provided annually, although EU sources claim it to be US$ 80 billion.

Moreover, the emission of GHGs, particularly by the developed countries and certain large and industrializing developing countries, has kept increasing. Intergovernmental Panel on Climate Change (IPCC) 6th Assessment WG-2 Report indicates that the GHG concentration in the atmosphere is now the highest in two million years and rising. As a result, climate change is fast intensifying. A country like Bangladesh cannot go on adapting if it faces climate change impacts of ever-increasing proportions. Hence, it is urgently required that the main emitting countries reduce their emissions quickly and in large quantities. There is a small window of opportunity, up to 2030, to act accordingly. Otherwise, the situation may be catastrophic for not only the climate-vulnerable countries but for the world as a whole.

Yet, despite negotiations every year at world climate conferences (Conference of the Parties or COP under the United Nations Convention on Climate Change-UNFCCC). The 27th, the latest, COP held in Egypt concluded a few days ago with precious little to slow achievements in relation to the reduction of GHGs as required to keep global warming at 1.5°C or well below 2^0C by the end of the century, the global goal set in the Paris Agreement (at COP21), compared to pre-1st industrial revolution levels. Available estimates suggest the world is on course for at least a warming of 2.8^0C if all the commitments (conditional and unconditional) made by all countries through their nationally determined contributions (NDCs) are delivered. But, past experiences relating to meeting commitments concerning climate change management suggest, and also due to the unlikely availability of financial support as required to developing countries to help them fulfill their conditional commitments, it appears that global warming will be much more than 2.8^0C.

Note that the IPCC 6th Assessment WG-2 Report describes the devastations caused by climate change-induced natural disasters now faced by countries around the world that are threatening the lives and livelihoods of millions upon millions of people while the world is now only 1^0C warmer. It can easily be gauged that if the warming is 3^0C or more, humanity and the earth could face disastrous consequences. In this context, the UN Secretary-General Antonio Guterres said at COP27: "We need all hands on deck for faster, bolder climate action. A window of opportunity remains open, but only a narrow shelf of light remains. We are getting dangerously close to the point of no return. The global climate fight will be won or lost in this crucial decade on our watch. One thing is certain: those that give up are sure to lose. So, let us fight together-and let's win." He also crisply said: 'the world is on a highway to climate hell' and 'Humanity has a choice: cooperate or perish.' Apparently, the world, particularly the developed world is not about to listen. Thus, COP27 has, by and large, ended with a whimper.

The Government of Bangladesh, led by Prime Minister Sheikh Hasina, has been very active in international negotiations and domestic climate actions. Internationally, in COPs and others for dealing with climate change, for example, Bangladesh has been strongly demanding individually or collectively along with other developing countries through G77 and LDC groupings and Climate Vulnerable Forum drastic and fast reduction of GHGs consistent with the Paris Agreement goal of 1.5^0C warming by the end of this century and adequate climate financing by developed countries for adaptation needs of the developing countries, especially the LDCs and climate vulnerable countries. But, so far, the outcome is grossly disappointing. Any significant improvement, particularly in actions, does not look like being on the cards at present.

But, as noted earlier, Bangladesh is one of the worst sufferers of climate change impacts while not being at all responsible for this intensifying menace. However, bereft of any meaningful support from the international community, Bangladesh is trying its best to combat climate change. The impacts suffered by the country include economic and infrastructural damages and losses due to result of more frequent and generally more devastating floods, cyclones, storm surges, salinity ingress, drought, river erosion, and so on. The food security of the affected people is often compromised due to production and income losses. Also, large numbers of people are being displaced every year, particularly due to river erosion.

Bangladesh has been implementing policy and climate action responses mainly using its own financial and other resources. In 2009, the government adopted Bangladesh Climate Change Strategy and Action Plan (BCCSAP), which has recently been updated. Bangladesh Climate Change Trust was set up in 2010, to which budgetary allocations are made annually for specific climate actions, mostly for adaptation. Five-Year Development Plans and Annual Development Programmes include climate change responses. In fiscal 2020, the government spent a total of US$ 5 billion from its own resources for climate actions through various government ministries. Prime Minister Sheikh Hasina is leading from the front in combatting climate change domestically and in helping shape appropriate international climate policies and action programmes.

But, given limited resources, Bangladesh cannot make much headway in combatting climate change impacts through adaptive actions. More can be achieved if the available resources are used more purposefully by prioritizing climate actions and avoiding wastage and corruption. This must be done. However, even so, not a great deal could be achieved in relation to the needs.

As noted earlier, overall, the future of Bangladesh and the world at large remains on course for disastrous consequences, given persisting intransigence on the part of the world leaders, particularly of developed countries and industrializing large developing countries, leading to their failure to undertake drastic and cooperative climate actions as called for by science.

Young Scientists for Health and Environment

I have tried to give, in broad outlines, the health service status in Bangladesh and proposed the setting up of UHC in Bangladesh to be initiated without further loss of time as well as global and Bangladesh-specific environment and climate change issues and the way these are being addressed or not addressed. It has been indicated that humanity is likely heading to a climate catastrophe unless science-dictated actions on mitigation and adaptation are taken while time remains.

The two issues-health and environment and climate change-are of crucial importance in the context of sustainable development. Young scientists can find it worthwhile and rewarding from their professional point of view as well as because of the potential contributions they can make to human progress by either working on health issues or on environmental and climate change issues. I have outlined the state of play with regard to both fields. Some challenges and the urgency of addressing them effectively have been highlighted. Yong scientists may be interested in taking up one or the other field, given their background and interest, as the major area of their work-research, dialogue, innovation, and management. Make their best possible contributions to ensuring at least adequate primary healthcare services for all or, if their choice is environment and climate change, towards environmentally sound development.

References

Bangladesh Bureau of Statistics (BBS), Government of the People's Republic of Bangladesh. *Preliminary Report on Population and Housing Census* 2022, Bangla Version, September 2022.

Chowdhury AMR and R Yates. Universal Health Coverage: A Strategy to tackle the Pandemic and Deliver Health, Economic and Political Benefits, *Asia Pacific Journal on Environment and Development*, Special Issue. BUP and DScE, Dhaka, June 2022.

Ministry of Health and Family Welfare (MoH&FW)..*Expanding Social Protection for Health: Towards Universal Coverage: Healthcare Financing Strategy 2012-2032*: Government of the People's Republic of Bangladesh September 2012.

Sarker AR, Ali SMZ, Ahmed M, Chowdhury SMZI and Ali N. Out-of-pocket payment for healthcare among urban citizens in Dhaka, Bangladesh. *Plos One* 2022; 17(1): e0262900.

J. Bangladesh Acad. Sci. 46(2); 135-145: December 2022 DOI: 10.3329/jbas.v46i2.59895

Journal of Bangladesh Academy of Sciences

Journal homepage: http://www.bas.org.bd/publications/jbas.html

Research Article

Optimization of the cupric oxide nanoparticles synthesis by novel *spondias mombin* peel extract exhibited excellent peroxidase activity

Md. Rajibul Akanda,* Umme Habiba Ema, M. Aminul Haque, Md. Mehedi Hasan and Md. Al-amin Miah

Department of Chemistry, Jagannath University, Dhaka, Bangladesh

ARTICLE INFO

Article History

Received: 19 May 2022
Revised: 1 August 2022
Accepted: 5 December 2022

Keywords: Green synthesis, Cupric oxide nanoparticles, *Spondias mombin* peel extract, Peroxidase activity.

ABSTRACT

This study describes a straightforward protocol for synthesizing cupric oxide nanoparticles from the peel extract of *Spondias mombin*. The CuO NPs were produced in a basic H_2O solution as cubic-shaped, homogenous nanoparticles with excellent peroxidase activity without taking any special precautions. The influence of the concentration of the peel extract, temperature as well as the synthesis medium on CuO NPs production has been investigated extensively. The typical UV-visible absorption maxima observed at wavelengths of 279 and 383 nm observed in spectrophotometry confirmed the formation of CuO NPs. Moreover, the homogeneity, shape (cubic), and size (approximately averaged ~31nm (29nm~38nm)) of the synthesized CuO nanoparticles under optimum conditions were confirmed through the SEM technique. Besides, its elemental compositions, capping agent, and crystallinity were investigated through EDS, FT-IR and XRD. Finally, in the presence of hydrogen peroxide (H_2O_2), the as-prepared CuO NPs demonstrated excellent peroxidase activity against 3,3',5,5'-tetramethylbenzidine (TMB).

Introduction

Recently, copper oxide nanoparticles (CuO NPs) have received much interest, particularly due to their antibacterial and biocide properties (Nations et al., 2015; Perreault et al., 2012 and Nguyen, 2014), distinctive electrical). Being in nano size and semiconducting character with narrow bandgap, super thermal conductivity, photovoltaic properties, high stability, potent antimicrobial activity (Tran, optical, and magnetic properties and has been employed in a wide range of applications, including catalysis (Yecheskel et al., 2013), energy conversion, and storage (Kumar et al., 2013), magnetic storage (Rashad et al., 2013), gas sensors (Aslani and Oroojpour, 2011; Yang et al., 2011; Li et al., 2008), thermites (Wang and Xu, 1999), as well as optoelectronics (Gupta et al., 2018). Copper oxide nanoparticles demonstrated excellent performance as nanofluids in heat transfer applications. For instance, it has been found that adding of 4% CuO improves water's thermal conductivity by 20% (Lee et al., 1999) and photoconductive and photothermal applications (Rakhshni, 1986). Besides, it has diverse applications in dye removal (Phang et al., 2021), photovoltaic devices (Jiang et al., 2015), waste-water treatment (Das et al., 2018), batteries (Zhao et al., 2016), agriculture (Dimkpa et al., 2012), textiles (Shaheen et al., 2021), food preservation (Kazemian et al., 2019). Therefore, it is highly desirable to synthesize copper oxide nanoparticles with defined, controllable size, shape, and morphology.

The fabrication of copper and copper oxide nanoparticles (CuO NPs) has been reported using a

*Corresponding author: <rhakanda@gmail.com, rhakanda@chem.jnu.ac.bd>

variety of methods until now, including chemical vapor deposition (Eisermann et al., 2012), chemical reduction method (Sarker et al., 2021), electrochemical methods (Zhang and Hua, 2014), photochemical (Nishino et al., 2017; Jung et al., 2011), solvothermal route (Sarker et al, 2022a, b), and polyol (Ramyadevi et al., 2012). Most of those methods negatively impact the environment since they utilize harsh, hazardous, and poisonous substances. They are also costly and do need expensive reaction conditions. According to Akintelu et al. (2020), additional research is needed to reduce the toxicity of the CuO NPs process of production while retaining and/or enhancing their performance in environmental or healthcare applications. Therefore, eco-friendliness, ease of synthesis, safety, time efficiency, non-toxicity, and versatile applications have established green chemistry or biological pathways of synthesis as a research focus.

According to literature, CuO NPs have been synthesized by different biological species such as fungi (Saravanakumar et al., 2019), algae (Bhattacharya et al., 2019), etc. and green plants such as *Catha edulis* leaf (Gebremedhn et al., 2019), *Calotropis gigantea* leaf (Sharma et al., 2015), *P. acerifolium* (leaf) (Saif et al., 2016), *gum karaya* (gum) (Padi and Černík, 2013), *Gundelia tournefortii* (stems) (Nasrollahzadeha et al., 2015a), *Thymus vulgaris L* (leaf) (Nasrollahzadeha, 2016), *Citrus lemon* (juice) (Mohan et al., 2015), *Gloriosa superba L* (leaf) (Naika et al., 2015), *Tinospora cordifolia* (leaf) (Udayabhanu et al., 2015), *Punica granatum* (peels) (Ghidan et al., 2016), *Carica papaya* (leaf) (Sankar et al., 2014), *Anthemis nobilis* (flowers) (Nasrollahzadeh et al., 2015b), Tamarix gallica (leaf) (Nasrollahzadeh et al., 2015c), *Coffee Powder* (beans) (Fardood, and Ramazani 2016), *Bifurcaria bifurcate* (alga) (Abboud et al., 2014), *Aloe barbadensis* (leaf) (Gunalan et al., 2012), *Aloe vera* (leaf) (Kumar et al., 2015), *Tea and Coffee* (leaf) (Sutradhar et al., 2014) etc.

According to the literature report on the phytochemical contents of *S. mombin* leaves and their feasibility towards nanoparticle synthesis, Recently, our research team investigated the phytochemical constituents of *S. mombin* peel extract and found its suitability as well (Njoku, and Akumefula 2007, Mohammad et al., 2014, Engels et al., 2012). And we used *S. mombin* peel extract successfully for Pd NP synthesis (Akanda et al., 2021). Our research group recently compared the synthesis of CuO nanoparticles by *S. mombin* peel extract in a buffer system Vs an H_2O system and investigated the synthesis in a PBS buffer system (Akanda et al., 2022). To the author's knowledge, no studies have been conducted on the facile synthesis of CuO NPs in the H_2O system by *S. mombin* peel extract. Additionally, according to Yugandhar et al. (2017), the green extract's ascorbic acid is principally responsible for the production of CuO NPs, while the yellowish part of ripe *S. mombin* contains a significant amount of ascorbic acid (de Carvalho et al., 2015). Therefore, ripe *S. mombin* was harvested for this study, and its yellowish peel was chosen for extract preparation and CuO NPs production in H_2O.

The peel extract of *S. mombin* fruits in H_2O was employed as the green reductant in this work, while $CuSO_4.5H_2O$ was used as the precursor. The peel extract functioned both as a capping agent and a reducing agent. The peel extract prepared at room temperature was employed for the synthesis of our CuO NPs. Furthermore, a thorough investigation of the effects of peel extract concentration, solvent system medium, and temperature on the synthesis of CuO NPs was undertaken systematically. CuO NPs produced a maintained cubic shape, appeared homogenous and crystalline, and under optimal settings demonstrated high peroxidase activity.

Materials and Apparatus

Chemicals and reagents

S. mombin peels were obtained from Shahbagh, Dhaka, Bangladesh. From Scharlau, Spain, we purchased copper sulfate ($CuSO_4.5H_2O$), di-Sodium monohydrogen phosphate dihydrate ($Na_2HPO_4.2H_2O$),

and H_2O_2. We received sodium hydroxide pellets & mono-sodium dihydrogen phosphate dihydrate ($NaH_2PO_4.2H_2O$) from Duksan. China's Hangzhou Xinhua Paper Industry supplied the double-ring filter paper. The experiment was carried out entively with distilled water.

Instrumentation

The UV-1800 model double-beam spectrophotometer came from Shimadzu of Japan. The magnetic stirrer was manufactured by Daihan Labtech of Korea, (model LMS-1003). Distilled water plant we used (Basic/PH4 Pure-HIT still type) was provided by Glassco in the UK. The Energy-dispersive X-ray spectroscopic (EDS) instrument (model (SUPRA 55)-CARL ZEISS) and the scanning electron microscopic (SEM) system (model JSM-7600F) were both made by JEOL, Japan.

preparation of peel extract of *S. mombin* and synthesis of CuO nanoparticles

Ripe *S. mombin* fruits were obtained from a nearby market, thoroughly cleaned using distilled water, and allowed to air dry for a couple of hours. The fruit peel was then removed and washed once more. The peels were then mashed with distilled water to make a paste.

Following that, 10 g of the peel paste was diluted by adding to 20 mL of distilled water in a 100 mL beaker and stirred using a magnetic stirrer for 10 min at room temperature. The extract was then filtered and collected with double filter paper; after that, it was stored at 4 °C for subsequent experiments. In our previous study, the phytochemical contents of peel extract were also determined. We found that the total phenolic content of peel extract was calculated to be approximately 26.035 g/mL GAE per mg of plant material, the total flavonoid content was estimated at 76.871 g/mL, and the total condensed tannin amounted to approximately 21.581 g/mL QE per mg of plant material, respectively (Akanda et al., 2021). Although the particular reducing agent for the formation of CuO NPs from peel extract is uncertain, it was proposed that the ascorbic acid of the peel extract (which was not determined) was accountable for NPs production (Yugandhar et al., 2017). The precursor $CuSO_4.5H_2O$ solution for the production of CuO NPs was prepared in water in a beaker. A 0.01 M 10 mL $CuSO_4.5H_2O$ solution was prepared in a different beaker using distilled water. In a different beaker, 10 mL of 0.01 M $CuSO_4.5H_2O$ solution was transferred before 10 mL of the peel extract was quickly added. The Cu^{2+} concentration in the solution has been determined to be at a final concentration of 2.5 mM, and the solution's color changed to a brownish color.

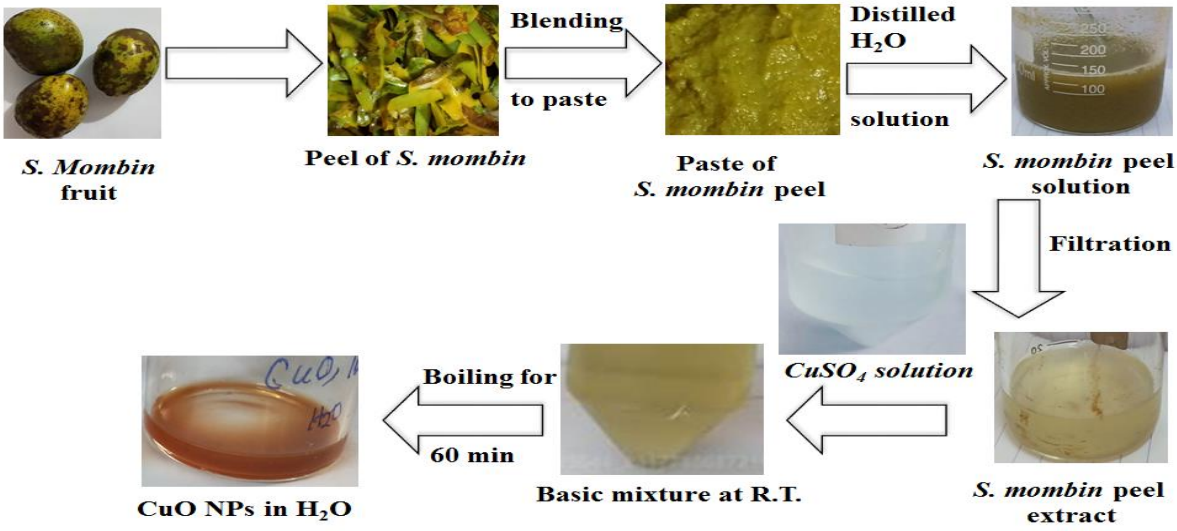

Scheme. Schematic representation for forming CuO NPs from *S. mombin* peels extracts in the water system.

CuO NPs were generated by heating the resultant solution to boiling for 60 minutes while vigorously stirring. The generation of CuO NPs was confirmed by the solution's deep reddish color following heating. The **scheme** provides a brief schematic depiction of the whole process.

Results and discussions

Confirmation and optimization of the CuO NPs synthesis

Fig. 1 illustrates the UV-Visible spectra of CuO NPs produced from *S. mombin* peel extract and 0.0025M $CuSO_4$ solution. The generated CuO NPs were dispersed in an alkaline H_2O system, subsequently sonicated to ensure uniform dispersion, and then sent straight away for UV-Visible spectrophotometric studies. The spectrum shows typical CuO NP absorption maxima at wavelengths of 279 and 383 nm, which is evident from the curve in Fig. 1A (green curve) and Fig. 1B and is not present in the curves of the other components of Fig. 1A. The electronic transitions via the intrinsic band-gap of CuO are what cause this pattern of absorption (Zak et al., 2012 and 2013). As the concentration of *S. mombin* peel extract is raised, Fig. 1B demonstrates rising absorbance while keeping the same band-gap as a sign of the higher peel extract concentration. Additionally, the existence of sharp peaks denotes a state that is evenly distributed and stable. For this work, 10 mL (0.1250 g/mL) of the peel extract from Fig. 1B's (blue curve) peel was taken into account since a concentration of peel extract that is too high might inhibit the activity of CuO NPs by obstructing their active sites.

Optimization of medium and temperature conditions for CuO NPs synthetic

We have studied the optical study by the addition of 0.1250 g/mL peel extract in 0.0025M precursor solution to realize the effect of medium and temperature. Fig. 2A and B show the optical images of the precursor $CuSO_4.5H_2O$ and peel extract respectively. The reaction system's medium was controlled by adding hydrochloric acid, and sodium hydroxide, respectively, and the medium was confirmed through pH in all three mediums. It was found that only the basic medium showed color changes (Fig. 2C). Indicating reaction can occur in the basic medium only. The mixed solution was left at room temperature, 60 ^{0}C, and boiling temperature to confirm synthesis Fig. 2D.

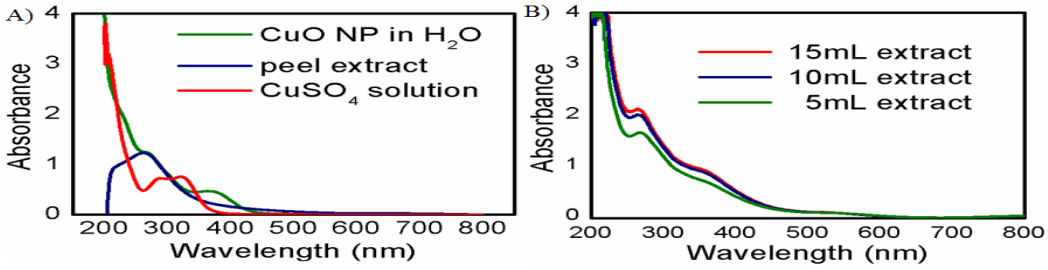

Fig. 1. (A) UV-Visible spectra of the synthesized CuO NPs in H_2O (green curve), precursor 0.0025M $CuSO_4.5H_2O$ (red curve) and 0.1250 g/mL peel extract (blue curve) and (B) UV-Visible spectra of the synthesized CuO NPs on 5mL (0.1875 g/mL-red curve), 10 mL (0.1250 g/mL-blue curve) and 15mL (0.0625 g/mL-green curve) concentration of peel extract, respectively, in H_2O.

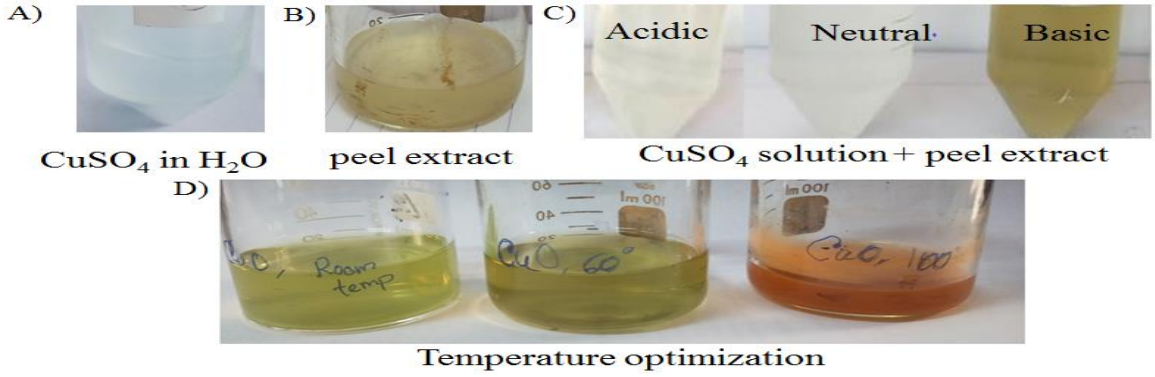

Fig. 2. Optical image of (A) 0.0025M $CuSO_4$ solution, (B) 0.1250 g/mL *S. mombin* peel extract in water systems (C) reaction of 0.0025M $CuSO_4$ solution with 0.1250 g/mL *S. mombin* peel extract in acidic, neutral and basic medium respectively and (D) temperature effect nanoparticles formation.

It was found that only boiling temperature can synthesize CuO NPs. Thus, basic medium and boiling temperature was considered the optimum conditions for the synthesis of CuO NPs.

Characterization of the synthesized CuO NPs in the basic water system

CuO nanoparticles were synthesized and characterized by SEM and EDS study after optimizing the synthetic conditions as shown in Figure 3(A-C). The SEM data was analyzed, and it was revealed that Fig. 3A, where the magnification is 50,000, appears to have few aggregations but a mostly homogeneous synthesis of nanoparticles. The produced CuO NPs appear to have a cubic shape in Fig. 3B, which has a magnification of 100,000. Their average size is around 31 nm (29 nm–38 nm). Most greenly synthesized CuO NPs are spherical (Amin et al., 2021, Alhalili, 2022), but quasi-spherical (Okpara et al. 2021) and rod-shaped CuO (Tavakoli et al., 2019) are also found. It is anticipated that an increased number of edges, corners, and faces on cubic-shaped CuO NPs might be responsible for their excellent peroxidase activity (Ni and Wang, 2015). Importantly the elemental composition of CuO NPs was validated by its EDS analysis, which is shown in Fig. 3C. The existence of the green species on artificially generated CuO NPs as a capping agent and stabilizing agents was confirmed through its FT-IR analysis in Fig. 4(A).

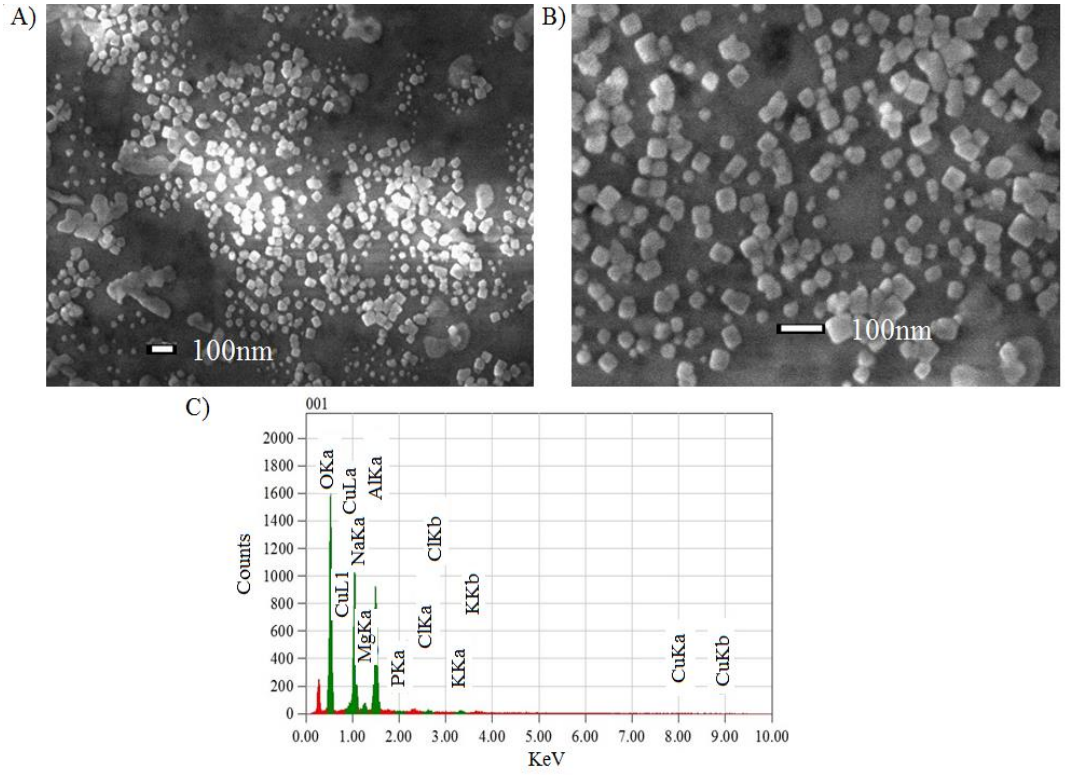

Fig. 3. SEM images of the synthesized CuO NPs in 100 nm scale bar with (A) x50,000, (B)x100,000 magnification from the mixture of 0.0025 M $CuSO_4.5H_2O$ and 0.1250 g/mL peel extract in basic H_2O system. And (C) EDS, spectra of the as-synthesized CuO NPs from the mixture of 0.0025 M $CuSO_4.5H_2O$ and 0.1250 g/mL peel extract in a basic H_2O system.

The O-H groups of phenols cause a broad and strong peak to arise at around 3450 cm^{-1}. Stretching of the C-H caused the band at 2860 cm-1. The stretching vibration of the C-O group of primary and secondary phenols (C-O) was responsible for the absorption peak at 1074.0 cm-1, whereas the aromatic bending vibration of the C-H group was responsible for the smaller peaks at 1722 and 1475 cm-1. The above analysis confirmed that these functional groups were from peel extract as a stabilizing as well as a capping agent for the nanoparticles. Additionally, a prominent peak in the spectra at 484.13 cm-1 is seen due to the characteristic properties of Cu-O bond formation in CuO. (Khan et al., 2011) Furthermore, the absence of a peak at 610 cm^{-1}, the frequency mode caused by Cu_2O in Fig. 4(A), further demonstrates that the as-prepared nanoparticles consist entirely of the CuO phase with no traces of Cu_2O. (Botsa et al., 2018). In Fig. 5, the self-assembled CuO sample's characteristic XRD pattern was displayed. Its cubic shape and crystallinity were confirmed by the detection of three diffraction peaks that correspond to the (-111), (111), and (002) lattice planes. These results were congruent with published values (JCPDS 80-1268). (Gou et al., 2012). We assume that pure CuO nanostructures were produced since no observable contaminant signals were observed. It discovered several other crystalline peaks that it was unable to identify. Additional crystallinity is believed to promote high peroxidase activity.

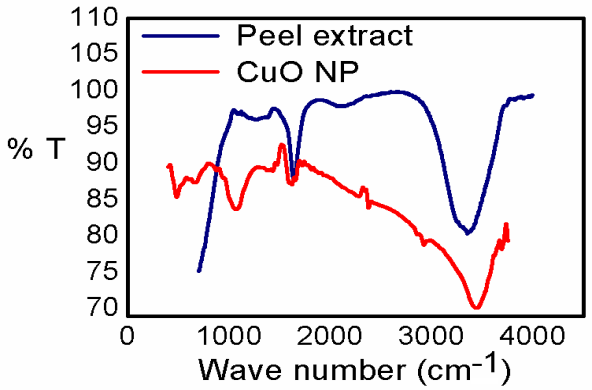

Fig. 4. FT-IR spectra of the synthesized CuO NPs from the mixture of 0.0025 M $CuSO_4.5H_2O$ and 0.1250 g/mL peel extract in basic H_2O system.

Peroxidase activity of the synthesized CuO NP

It is known from the literature that if the synthesized NPs are in CuO form in H2O, it shows peroxidase activity (Chen et al., 2011 and 2012). Therefore, the TMB oxidation in the presence of H2O2 has been applied using the as-synthesized CuO NPs under optimal basic H2O operating conditions to test its peroxidase activity. Interestingly, no green method-mediated produced CuO NPs have had their peroxidase activity tested up to now. As a result, the study's findings are extremely significant. TMB was found to not be oxidized with H2O2 alone but to be easily oxidized when CuO NPs were added, demonstrating its peroxidase activity. This is shown schematically in Fig. 6A. The addition of CuO NPs to a mixed solution of TMB solution (red curve), H2O2 (blue curve), and oxygen (UV-visible spectra in Fig. 6B) resulted in the creation of oxidized TMB (purple curve, peak at 652 nm) (green curve). The peak of the oxidized TMB (purple curve) at 652 nm represents the oxidation kinetics of TMB with a single electron transfer (Dahal et al., 2015). Interestingly, optimization of the basic H2O systems for CuO NPs synthesis shows significant peroxidase activity and is completed within 10 minutes. In this instance, additional prolongation of time did not result in any alteration of absorbance (data not shown). The reaction was extremely sluggish and finished in 30 minutes compared to prior studies on un-optimized basic H2O-assisted produced CuO NPs (Akanda et al., 2022). Therefore, it can be claimed that the CuO NPs produced under optimized conditions were more homogeneous, had single (cubic) morphologies, and were approximately the same size.

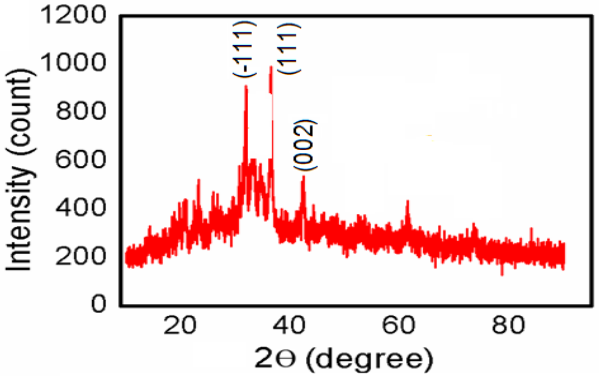

Fig. 5. XRD spectra of the synthesized CuO NPs from the mixture of 0.0025 M $CuSO_4.5H_2O$ and 0.1250 g/mL peel extract in Basic H_2O system.

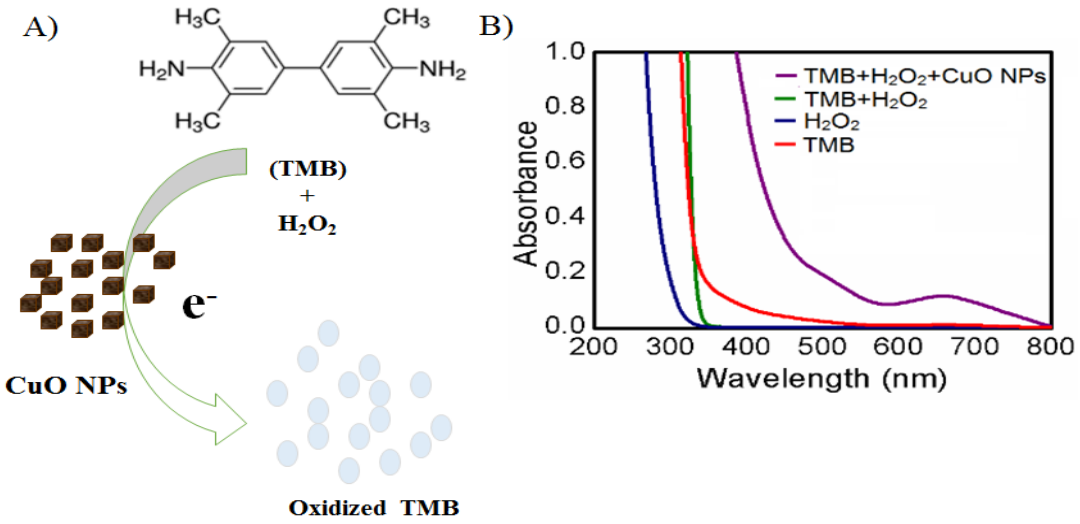

Fig. 6. (A) Schematic representation of TMB oxidation by CuO NPs in the presence of H_2O_2. (B) UV-Visible spectra of the synthesized CuO in basic H_2O with 0.00208M TMB and 0.1M H_2O_2.

Conclusion

We conclude that the basic method of synthesizing CuO NPs with H_2O was thoroughly optimized in this study, and their superiority over unoptimized methods has been proved. The basic H_2O-assisted synthetic conditions were optimized with regard to the temperature, medium of the synthesis, and concentration of *S. mombin* peel extract. CuO NPs of about 31 nm in size were produced under optimal conditions for a basic H_2O-assisted system.

These NPs were homogeneous, well-dispersed, single-shaped (cubic), and well-stabilized. The remarkable peroxidase activity found in this study within the shortest amount of time (10 minutes) when applied to TMB oxidation is very beneficial for the bio-medicine industry. As a consequence, biomedical and green technology applications will be significantly impacted by the findings of this study.

Acknowledgments

This work was supported by the Jagannath University Research grant (2018-19) under the title "Green Synthesis of Copper Oxide (II) Nanoparticle Using Plant Extract for Biomedical Application".

Conflict of Interest The authors declared that they have no conflict of interest.

Author's contribution

M.R. Akanda contributed to the conceptualization, supervision, and manuscript drafting, U.M. Ema and M. Hasan carried out the whole experiment, M.A. Haque contributed to the conceptualization, and MA Miah contributed to data collection and preliminary drafting.

References

Abboud Y, Saffaj T, Chagraoui A, El Bouari A, Brouzi K, Tanane O, and Ihssane B. Biosynthesis, characterization and antimicrobial activity of copper oxide nanoparticles (CONPs) produced using brown alga extract (*Bifurcaria bifurcata*). *Appl. Nanosci.* 2014; 4(5): 571-576.

Akanda MR, Ema UH, Hauqe MA and Hasan MH. Comparative study on cupric oxide nanoparticles synthesis in saline buffer versus basic water by *Spondias mombin* peel extract for biocatalysis. *Inorg. Nano-Met. Chem.* 2022. https://doi.org/10.1080/24701556.2022.2068587.

Akanda MR, Hasan MH, Ema UH and Haque MA, Optimization of *Spondias mombin* peel extract mediated synthesis of palladium nanoparticles as nanozyme exhibits potent multienzyme activity. *J. Iran. Chem. Soc.* 2021; 18: 3407-3415.

Akintelu SA, Folorunso AS, Folorunso FA, and Oyebamiji AK. Green synthesis of copper oxide nanoparticles for biomedical application and environmental remediation. *Heliyon* 2020; 6: e04508.

Alhalili Z. Green synthesis of copper oxide nanoparticles CuO NPs from *Eucalyptus globulous* leaf extract: Adsorption and design of experiments. *Arab. J. Chem.* 2022; 15: 103739.

Amin F, Fozia, Khattak B, Alotaibi A, Qasim M, Ahmad I, Ullah R, Bourhia M, Gul A, Zahoor S and Ahmad R. Green synthesis of copper oxide nanoparticles using *Aerva javanica* leaf extract and their characterization and investigation of in vitro antimicrobial potential and cytotoxic activities. *Evid. Based Complement. Altern. Med.* 2021; 2021: 5589703.

Aslani A and Oroojpour V. CO gas sensing of CuO nanostructures, synthesized by an assisted solvothermal wet chemical route. *Phys. Rev. B Condens. Matter*. 2011; 406(2): 144-149.

Bhattacharya P, Swarnakar S, Ghosh S, Majumdar S and Banerjee S. Disinfection of drinking water via algae mediated green synthesized copper oxide nanoparticles and its toxicity evaluation. *J. Environ. Chem. Eng.* 2019; 7(1): 102867.

Botsa SM, Ramadevi D and Basavaiah K. A Facile synthesis of copper oxide nanorods for photocatalytic degradation of organic pollutant and inactivation of pathogens. *J. Nanosci. Tech.* 2018; 4(5): 467-470.

Chen W, Chen J, Feng YB, Hong L, Chen QY, Wu LF, Lin XH and Xia XH. Peroxidase-like activity of water-soluble cupric oxide nanoparticles and its analytical application for detection of hydrogen peroxide and glucose. *Analyst*, 2012; 137: 1706-1712.

Chen W, Chen J, Liu A-L, Wang L-M, Li G-W and Lin XH. Peroxidase-like activity of cupric oxide nanoparticle. *Chem. Cat. Chem*, 2011; 3:1151-1154.

Dahal E, Curtiss J, Subedi D, Chen G, Houston JP and Smirnov S. Evaluation of the catalytic activity and cytotoxicity of palladium nanocubes: The role of oxygen. *ACS Appl. Mater. Interfaces* 2015; 7(18): 9364-9371.

Das P, Ghosh S, Ghosh R, Dam S and Baskey (Sen) M. *Madhuca longifolia* plant mediated green synthesis of cupric oxide nanoparticles: A promising environmentally sustainable material for waste water treatment and efficient antibacterial agent. *J. Photochem. Photobiol. B: Biol.* 2018; 189: 66-73.

de Carvalho JM, Maia GA, da Fonseca AVV, de Sousa PHM and Rodrigues S. Effect of processing on physicochemical composition, bioactive compounds and enzymatic activity of yellow mombin (*Spondias mombin L.*) tropical juice. *J. Food Sci. Technol.*, 2015; 52(2): 1182-1187.

Dimkpa CO, McLean JE, Britt DW, and Anderson AJ. Bioactivity and biomodification of Ag, ZnO, and CuO nanoparticles with relevance to plant performance in agriculture. *Ind. Biotechnol.* 2012; 8(6): 344-357.

Eisermann S, Kronenberger A, Laufer A, Bieber J, Haas G, Lautenschläger S, Homm G, Klar PJ and Meyer BK. Copper oxide thin films by chemical vapor deposition: Synthesis, characterization and electrical properties. *Phys. Status Solidi A* 2012, 209(3), 531-536.

Engels C, Gräter D, Esquivel P, Jiménez VM, and Gänzle MG, Characterization of phenolic compounds in jocote (Spondias purpurea L.) peels by ultra high-performance-liquid chromatography/ electrospray ionization mass spectrometry. *Food Res. Int.* 2012; 46: 557-562.

Fardood ST and Ramazani A. Green synthesis and characterization of copper oxide nanoparticles using coffee powder extract. *J. Nanostruct.* 2016; 6(2): 167-171.

Gebremedhn K, Kahsay MH and Aklilu M. Green synthesis of CuO nanoparticles using leaf extract of *Catha edulis* and its antibacterial activity. *J. Pharm. Pharmacol.* 2019; 7: 327-342.

Ghidan AY, Al-Antary TM and Awwad AM. Green synthesis of copper oxide nanoparticles using *Punica granatum* peels extract: Effect on green

peach Aphid. *Environ. Nanotechnol. Monit. Manag.* 2016; 6: 95-98.

Gou L, Tong F, Liu H, Yang H and Li J. Shape-controlled synthesis of self-assembly cubic CuO nanostructures by microwave. *J. Mater. Lett.* 2012; 71: 32-35.

Gunalan S, Sivaraj R and Venckatesh R. Aloe barbadensis Miller mediated green synthesis of mono-disperse copper oxide nanoparticles: optical properties. *Spectrochim. Acta A Mol. Biomol. Spectrosc.* 2012; 97: 1140-1144.

Gupta D, Meher SR, Illyaskutty N and Alex ZC. Facile synthesis of Cu_2O and CuO nanoparticles and study of their structural, optical, and electronic properties. *J. Alloys Compd.*, 2018; 743: 737-745.

Jiang T, Wang Y, Meng D, and Yu M. Facile synthesis and photocatalytic performance of self-assembly CuO microspheres. *Superlattice. Microst.* 2015; 85: 1-6.

Jung S, Jeon S and Yong K. Fabrication and characterization of flower-like CuO–ZnO heterostructure nanowire arrays by photochemical deposition. *Nanotechnology* 2011; 22: 015606.

Kazemian S, Zarrinnia V, Khosroshahli M and Hasanzadeh N. Investigation on the control effects of green copper oxide (CuO) nanoparticles on the tomato gray mold disease caused by *Botrytis cinerea*. *Iranian J. Med. Arom. Plants* 2019; 35: 54-67.

Khan MAM, Kumar S, Ahamed M, Alrokayan SA, and AlSalhi MS. Structural and thermal studies of silver nanoparticles and electrical transport study of their thin films. *Nanoscale Res. Lett.* 2011; 6: 434.

Kumar PPNV, Shameem U, Kollu P, Kalyani RL and Pammi SVN. Green synthesis of copper oxide nanoparticles using *Aloe vera* leaf extract and its antibacterial activity against fish bacterial pathogens. *J. Bio. Nano. Sci.* 2015; 5(3): 135-139.

Kumar V, Masudy-Panah S, Tan CC, Wong TKS, Chi DZ, and Dalapati GK. Copper oxide based low cost thin film solar cells. *Proceedings of the IEEE 5th International Nanoelectronics Conference (INEC '13)*, 2013; 443-445.

Lee S, Choi US, Li S and Eastman JA. Measuring thermal conductivity of fluids containing oxide nanoparticles. *J. Heat Transfer* 1999; 121: 280-289.

Li Y, Liang J, Tao Z, and Chen J. CuO particles and plates: Synthesis and gas-sensor application. *Mater. Res. Bull.*, 2008; 43(8-9): 2380-2385.

Mohammad NAN, Arham NA, Jai J, and Hadi A. Plant extract as reducing agent in synthesis of metallic nanoparticles: A review. *Open J. Adv. Mater. Res.*, 2014; 832: 350-355.

Mohan S, Singh Y, Verma DK, and Hasan SH. Synthesis of CuO nanoparticles through green route using *Citrus limon* juice and its application as nanosorbent for Cr (VI) remediation: Process optimization with RSM and ANN-GA based model. *Process Saf. Environ. Prot.* 2015; 96: 156-166.

Naika HR, Lingaraju K, Manjunath K, Kumar D, Nagaraju G, Suresh D and Nagabhushana H. Green synthesis of CuO nanoparticles using gloriosa superba L. extract and their antibacterial activity. *J. Taibah Univ. Sci.* 2015; 9(1): 07-12.

Nasrollahzadeh M, Sajadi SM, Rostami-Vartooni A and Hussin SM. Green synthesis of CuO nanoparticles using aqueous extract of *Thymus vulgaris L.* leaves and their catalytic performance for N-arylation of indoles and amines. *J. Colloid Interface Sci.* 2016; 466: 113-119.

Nasrollahzadeha M, Maham M, and Sajadi SM. Green synthesis of CuO nanoparticles by aqueous extract of *Gundelia tournefortii* and evaluation of their catalytic activity for the synthesis of N-monosubstituted ureas and reduction of 4-nitrophenol. *J. Colloid Interface Sci.* 2015a: 455: 245-253.

Nasrollahzadeh M, Sajadi SM and Vartooni AR. Green synthesis of CuO nanoparticles by aqueous extract of *Anthemis nobilis* flowers and their catalytic activity for the A3 coupling reaction. *J. Colloid Interface Sci.* 2015b; 459: 183-188.

Nasrollahzadeh M, Sajadib SM, and Maham M. *Tamarix gallica* leaf extract mediated novel route for green synthesis of CuO nanoparticles and their application for N-arylation of nitrogen-containing heterocycles under ligand-free conditions. *RSC Adv.* 2015c; 5(51): 40628-40635.

Nations S, Long M, Wages M, Maul JD, Theodorakis CW, and Cobb GP. Subchronic and chronic developmental effects of copper oxide (CuO) nanoparticles on *Xenopus laevis*. *Chemosphere* 2015; 135: 166-174.

Ni B. and Wang X. Face the Edges: Catalytic active sites of nanomaterials. *Adv. Sci.* 2015; 2: 1500085.

Nishino F, Jeem M, Zhang L, Okamoto K, Okabe S and Watanabe S. Formation of CuO nano-flowered surfaces via submerged photo-synthesis of crystallites and their antimicrobial activity. *Sci. Rep*. 2017; 7: 1063.

Njoku PC and Akumefula MI. Phytochemical and nutrient evaluation of *Spondias mombin* leaves. *Pakistan J. Nutr*. 2007; 6(6): 613-615.

Okpara EC, Ogunjinmi OE, Oyewo OA, Fayemi OE and Onwudiwe DC. Green synthesis of copper oxide nanoparticles using extracts of *Solanum macrocarpon* fruit and their redox responses on SPAu electrode. *Heliyon* 2021; 7: e08571.

Padi VVT and Černík M. Green synthesis of copper oxide nanoparticles using gum karaya as a biotemplate and their antibacterial application. *Int. J. Nanomed.* 2013; 8: 889-898.

Perreault F, Melegari SP, Da Costa CH, Rossetto ALdOF, Popovic R, and Matias WG. Genotoxic effects of copper oxide nanoparticles in Neuro 2A cell cultures. *Sci. Total Environ.* 2012; 441: 117-124.

Phang YK, Aminuzzaman M, Akhtaruzzaman M, Muhammad G, Ogawa S, Watanabe A and Tey LH. Green synthesis and characterization of CuO nanoparticles derived from papaya peel extract for the photocatalytic degradation of palm oil mill effluent (POME). *Sustainability* 2021; 13(2): 796.

Rakhshni AE. Preparation, characteristics and photovoltaic properties of cuprous oxide-a review. *Solid State Electron.* 1986; 29: 7-17.

Ramyadevi J, Jeyasubramanian K, Marikani A, Rajakumar G and Rahuman AA. Synthesis and antimicrobial activity of copper nanoparticles. *Mater. Lett.* 2012; 71: 114-116.

Rashad MM, Rayan DA, and Ramadan AA. Optical and magnetic properties of $CuO/CuFe_2O_4$ nanocomposites. *J. Mater. Sci.: Mater. Electron.* 2013; 24(8): 2742-2749.

Saif S, Tahir A, Asim T, and Chen Y. Plant mediated green synthesis of CuO nanoparticles: comparison of toxicity of engineered and plant mediated CuO nanoparticles towards daphnia magna. *Nanomaterials* 2016; 6(11): 205.

Sankar R, Manikandan P, Malarvizhi V, Fathima T, Shivashangari KS and Ravikumar V. Green synthesis of colloidal copper oxide nanoparticles using *Carica papaya* and its application in photocatalytic dye degradation. *Spectrochim. Acta A Mol. Biomol. Spectrosc.* 2014; 121: 746-750.

Saravanakumar K, Shanmugam S, Varukattu NB, Ali DM, Kathiresan K and Wanga M-H. Biosynthesis and characterization of copper oxide nanoparticles from indigenous fungi and its effect of photothermolysis on human lung carcinoma. *J. Photochem. Photobiol. B: Biol.*, 2019; 190: 103-109.

Sarker MZ, Rahman MM, Minami H., Suzuki T, Rahman MA, Khan A, Hoque SM, and Ahmad H. Magnetite incorporated amine-functional SiO_2 support for bimetallic Cu-Ni alloy nanoparticles produced highly effective nanocatalyst. *Colloids Surf. A Physicochem. Eng.* 2022a; 647: 129044.

Sarker MZ, Rahman MM, Minami H., Suzuki T., and Ahmad H. Amine functional silica–supported bimetallic Cu-Ni nanocatalyst and investigation of some typical reductions of aromatic nitro-substituents. *Colloid Polym. Sci.* 2022b; 300: 279-296.

Sarker MZ, Rahman MM, Minami H., Suzuki T., Hossain MK, and Ahmad H. Mesoporous amine functionalized SiO_2 supported Cu nanocatalyst and a kinetic-mechanistic degradation study of azo dyes. *Colloids Surf. A Physicochem. Eng.* 2021; 617: 126403.

Shaheen TI, Fouda A, and Salem SS. Integration of cotton fabrics with biosynthesized CuO nanoparticles for bactericidal activity in the terms of their cytotoxicity assessment. *Ind. Eng. Chem. Res.* 2021; 60(4): 1553-1563.

Sharma JK, Akhtar MS, Ameen S, Srivastava P and Singh G. Green synthesis of CuO nanoparticles with leaf extract of *Calotropis gigantea* and its dye-sensitized solar cells applications. *J. Alloys Compds.* 2015; 632: 321-325.

Sutradhar P, Saha M and Maiti D. Microwave synthesis of copper oxide nanoparticles using tea leaf and coffee powder extracts and its antibacterial activity. *J. Nanostruct. Chem.* 2014; 4: 86.

Tavakoli S, Kharaziha M and Ahmadi S. Green synthesis and morphology dependent antibacterial activity of copper oxide nanoparticles. *J. Nanostruct.* 2019; 9(1):163-171.

Tran TH and Nguyen VT. Copper oxide nanomaterials prepared by solution methods, some properties, and potential applications: A brief review. *Int. Sch. Res. Notices*, 2014;2014: 856592.

Udayabhanu, Nethravathi PC, Kumar MAP, Suresh D, Lingaraju K, Rajanaika H, Nagabhushana H, and Sharma SC. *Tinospora cordifolia* mediated facile green synthesis of cupric oxide nanoparticles and their photocatalytic, antioxidant, and antibacterial properties. *Mater. Sci. Semicond. Process.* 2015; 33: 81-88.

Wang X and Xu X. Thermal conductivity of nanoparticle-fluid mixture. *J. Thermophys. Heat Trans.*, 1999; 13(4): 474-480.

Yang M, He J, Hu X, Yan C and Cheng Z. CuO nanostructures as quartz crystal microbalance sensing layers for detection of trace hydrogen cyanide gas. *Environ. Sci. Technol.* 2011; 45(14): 6088-6094.

Yecheskel Y, Dror I, and Berkowitz B. Catalytic degradation of brominated flame retardants by copper oxide nanoparticles. *Chemosphere*, 2013; 93(1): 172-177.

Yugandhar P, Vasavi T, Devi PUM and Savithramma N. Bioinspired green synthesis of copper oxide nanoparticles from *Syzygium alternifolium (Wt.) Walp*: characterization and evaluation of its synergistic antimicrobial and anticancer activity. *Appl. Nanosci.* 2017; 7(7): 417-427.

Zak AK, Majid WHA, Mahmoudian MR, Darroudi M, and Yousefi R. Starch-stabilized synthesis of ZnO nanopowders at low temperature and optical properties study. *Adv. Powder Technol.* 2013; 24: 618-624.

Zak AK, Yousefi R, Majid WHA, and Muhamad MR. Facile synthesis and X-ray peak broadening studies of Zn1-xMgxO nanoparticles. *Ceram. Int.* 2012; 38: 2059-2064.

Zhang Q and Hua Y. Electrochemical synthesis of copper nanoparticles using cuprous oxide as a precursor in choline chloride-urea deep eutectic solvent: nucleation and growth mechanism. *Phys. Chem. Chem. Phys.* 2014; 16: 27088-27095.

Zhao Y, Mu S, Sun W, Liu Q, Li Y, Yan Z, Huo Z and Liang W. Growth of copper oxide nanocrystals in metallic nanotubes for high performance battery anodes. *Nanoscale* 2016; 8: 19994-20000.

J. Bangladesh Acad. Sci. 46(2); 147-154: December 2022 DOI: 10.3329/jbas.v46i2.60172

Journal of Bangladesh Academy of Sciences

Journal homepage: http://www.bas.org.bd/publications/jbas.html

Research Article

Pressure-induced valence changes of cerium in some cerium-based compounds

Md Shafiqul Islam, Md. Tarek Hossain and Abdul Hannan*

Department of Physics, Shahjalal University of Science and Technology, Bangladesh

ARTICLE INFO

Article History

Received: 12 June 2022
Revised: 8 August 2022
Accepted: 5 December 2022

Keywords: Effects of pressure, Cerium monochalcogenides, Cerium monopnictides, Birch equation of state, Valence change.

ABSTRACT

In the present work, we investigate how pressure affects the valence change of cerium in cerium-based compounds Ce*X* (*X*= O, S, Te, P, As, Sb, and Bi). The valence of cerium at a certain high pressure is estimated by comparing the experimentally observed unit cell volume and the calculated unit cell volume of stable trivalent cerium ion in the compound. The change in unit cell volume with pressure is estimated by employing the Birch equation of state. It is found that the valence of Ce in the Ce*X* is significantly influenced by both the applied pressure as well as the chemical environment around the Ce ion.

Introduction

Appling hydrostatic pressure on materials can change the properties of the materials. The extra-nuclear electronic states, especially the electronic states of localized *f* electrons in the compounds are responsible for altering the properties. The importance of high pressure work is increasing daily as materials exhibit variety of effects under high pressure. Application of high pressure on compounds produces numerous effects, namely, structural phase transition (Léger, 1993), uncommon resistivity (Okayama et al., 1992), the complicated structure of the magnetic phase (Hannan et al., 2002; Osakabe et al., 2002), change of Kondo effect (Hayashi et al., 2016), pressure-induced valence transition (Hossain et al., 2015), etc. In recent work, Ubukata et al., (2022) investigated the structural change of BaHCl at high-pressure up to 30 GPa using an in-situ high-intensity (synchrotron) X-ray diffraction. They reported that the tetragonal PbFCl-type structure (*P*4/*nmm*) of BaHCl changes into an orthorhombic structure at around 29 GPa.

In this work, the valence alterations of Ce in the two series of compounds, cerium monochalcogenides Ce*X* (*X*=O, S, and Te) and cerium monopnictides Ce*X* (*X*=P, As, Sb and Bi), have been calculated with pressure. Vedel et al. (1986), Léger et al. (1987), and Léger (1993) reported in detail the experimentally observed unit cell volume (V) with pressure (P) and also the structural phase transitions of these materials. They observed an unusual trend in the $P-V$ curves of these compounds in the high pressure up to 25 GPa. The pressure-volume relationships of the compounds (Léger, 1993) may be reproduced by adopting the Birch equation of state (Birch, 1947; Mito et al., 2007) using appropriate parameters in the equation. This reproduction is necessary to estimate of the valence change with the pressure. A part of this work has already been published (Hossain et al., 2015; Hossain and Hannan, 2017). This paper is dedicated to presenting the more precise calculated results of valence change with pressure for more compounds.

Let us focus on the experimentally observed (Léger, 1993) $P-V$ behavior of Ce*X* (*X*=O, S, and Te). The volume of the cerium oxide (CeO) decreases acutely with the applied pressure of up to 3 GPa and then falls slowly with a further increase in pressure. The NaCl-type structure of this compound remains

*Corresponding author: <ahannan-phy@sust.edu>

unchanged up to the pressure of 25 GPa. The volume drops gradually with pressure for cerium sulphide (CeS) and maintains a NaCl-type structure up to 27 GPa. The volume of CeTe decreases gradually up to 8 GPa, and afterward a structural phase transition occurs from NaCl to CsCl-type.

Among the series Ce*X* (*X*=P, As, Sb and Bi), the compound CeP shows a continuous decrease of volume with pressure, but at around 10 GPa, a large isostructural sudden transition is observed and then continues its continuous volume decrement with further increase of pressure up to about 20 GPa (Léger, 1993; Vedel et al., 1987). This isostructural transition arises due to the valence change (transition) of Ce ions with pressure, as Svane et al. (2001) reported in their theoretical work. Above 20 GPa, this compound shows a structural transition from NaCl to a CsCl-type layout. The volume of CeAs also decreases continuously with pressure until the pressure of 18 GPa is reached, and then the structural transition from NaCl to CsCl-type is occurred at around 18 GPa. CeSb shows a first-order structural conversion from NaCl-type to body central tetragonal structure occurs at 11 GPa. CeBi, on the other hand, shows the structural conversion from NaCl to coexisted CsCl-type and body central tetragonal structures with equal proportion at 13GPa.

Other reported phenomena of these compounds are as follows. Hannan et al., (2000) reported a notable decrease in the crystal lattice of CeSb below a certain temperature T_L at high pressure in the paramagnetic area. This temperature is approximately equal to the resistivity abnormality temperature T_R that appeared in the work of Okayama et al. (1992). Chattopadhyay *et al*. (1994) and Osakabe et al. (2002) reported the complicated magnetic pressure (P)−temperature (T) phase diagram in CeSb at low temperatures. The magnetic *P-T* phase diagram of CeP (Hannan et al., 2002) is more complicated than that of CeSb. The pressure-dependent electrical resistivity (ρ) of CeP is more anomalous than CeAs (Okayama et al., 1992). At pressures above 3 GPa applied on CeSb, an extraordinary rise of ρ while decreasing the temperature is obtained around 30 K (Okayama et al., 1992). It is seen that the peak resistivity increases with the increase of pressure, and it becomes nearly 23 times large at 7 GPa compared with that at ambient pressure. Additionally, CeBi exhibits a sharp peak of ρ at around 30 K coupled with the magnetic phase. Above 3 GPa, this peak converts into a hump and disappears gradually with the increase of pressure.

Hayashi et al. (2016) studied the pressure dependences of various parameters, such as the antiferromagnetic ordering temperature T_N, crystal-field splitting, and the ln$T$ anomaly of the Kondo effect in CeS, CeSe, and CeTe. They studied those from the measurement of electrical resistivity under various constant high pressures up to 8 GPa. It is observed that the ln$T$ term in the temperature dependence of ρ in each compound generally increases with the rise of pressure. This result indicates that *c–f* hybridization is increased by applying pressure. The authors discovered two ln T regions in these compounds. The first one is at high temperatures, where both Γ_7 and Γ_8 states are involved, which reflects crystal electric field (CEF) splitting, and the second one is at low temperatures, where the Γ_7 ground state has mainly appeared. From the ln$T$ term in the low-temperature region, Hayashi et al. (2016) found that the *c-f* hybridization strength, J_{cf} is largest in CeS and smallest in CeTe.

Svane et al. (2001) discussed the pressure-induced valence transitions in cerium monopinictides and monochalcogenides associated with isostructural or structural phase transition. De and Chatterjee (1989) studied this electronic band structure of CeS at high pressure using a self-consistent linear augmented plane-wave method in the local-density approximation to assess the change in valence with pressure.

Svane et al. (1999) also studied the electronic structure of CeS, CeSe, and CeTe using the self-interaction corrected local spin-density approximation. They found that the pressure-induced phase transitions are responsible for the delocalization of the *f* electrons, *i. e.*, for the valence change of Ce atoms from trivalent towards tetravalent. So far, we know, work on the

systematic change of valence of cerium in cerium-based compounds in a wide pressure range has yet to be reported except in our previous work, where we reported for several compounds.

To estimate the valence change of Ce of the compounds CeX (X=O, S, Te, P, As, Sb, and Bi) with pressure, we performed the following tasks. The experimentally observed pressure (P) −volume (V) relationships of those compounds were reproduced by adopting the Birch equation of state (Birch, 1947; Mito et al., 2007) with the bulk modulus (B_0) and its first pressure derivative (B^*) as fitting parameters. The $P-V$ relationship of those compounds for stable trivalent cerium ions has also been calculated using the same Birch equation but with appropriate bulk modulus and its first pressure derivative. The effect of pressure on the valence of cerium of those compounds has been realized clearly.

Calculation of relative volume

Experimental relative volume

Experimental $P-V$ curves (Léger, 1993) of CeX (X=O, S, Te, P, As, Sb and Bi) can be fitted (reproduced) well (or approximately) adopting the Birch equation (Birch, 1947; Mito et al., 2007) as written below:

$$P\left(\frac{V}{V_0}\right)=\frac{3}{2}B_0\left(\left(\frac{V}{V_0}\right)^{-\frac{7}{3}}-\left(\frac{V}{V_0}\right)^{-\frac{5}{3}}\right)\left[1-\frac{3}{4}(B^*-4)\left(1-(V/V_0)^{-2/3}\right)\right] \quad \text{..... (1)}$$

Here, V/V_0, B_0, and B^* are the relative volume, the Bulk modulus and the pressure derivative of the Bulk modulus, respectively. B_0 and B^* are used as fitting parameters during the reproduction of relative volume at each high pressure. IGOR Pro software, Version 8.0 has been used for all calculations to reproduce experimental data.

Relative volume of CeO

The reproduced experimental V/V_0 against P for CeO is shown in Fig. 1 by filled circles. The experimental data has been reproduced perfectly in the pressure range 0 to 3 GPa, utilizing the parameters $B_0=30$ GPa and $B^*=5$. B_0 and B^* in the pressure range of about 3 to 23.6 GPa are taken at 1.58 GPa and 679, respectively. It is seen that the reproduction of V/V_0 in the pressure range of about 3 to 6 GPa is not consistent with the experimental data of Léger (1993).

Relative volume of CeS and CeTe

Fig. 2 shows the variation of the reproduced experimental relative volume of CeS with pressure. The experimental data of Léger (1993) has been reproduced using 83.5 GPa and 2.2 for B_0 and B^*, respectively.

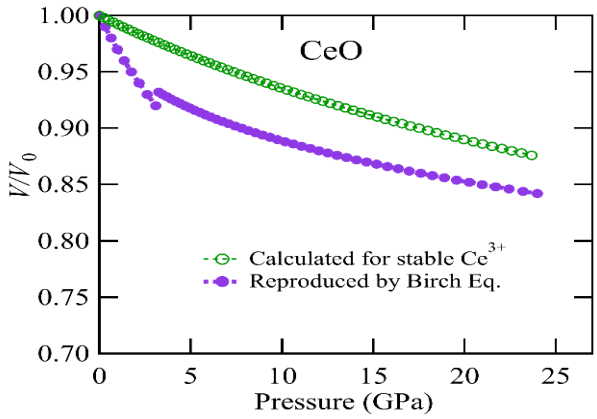

Fig. 1. Relative volume versus pressure curves for CeO. Filled circles represent experimental data (Léger, 1993) reproduced by Birch equation and open circles represent the data for stable Ce^{3+} ion.

The variation of the reproduced experimental relative volume of CeTe with pressure is also shown in Fig. 2. The Birch equation has exactly reproduced the experimental data with the parameters $B_0=58$ GPa and $B^*=8$.

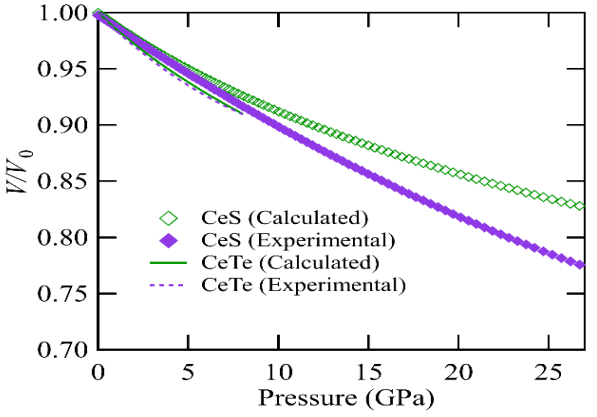

Fig. 2. Reproduced (experimental) relative volume versus pressure curves for CeS and CeTe (solid diamonds and dashed line) and their estimated curves (open diamonds and solid line) for the existence of stable Ce^{3+} ions in the materials.

Relative volume of CeP and CeAs

Fig. 3 shows the reproduced (experimental) relative volumes with pressure for CeP and CeAs. In the case of CeP, the exact reproduction has been attained using the parameters (B_0 and B^*) 64 GPa and 3 in all pressures between 0 and 9 GPa. The parameters B_0 and B^* are chosen to be 30 GPa and 9.2, respectively, to reproduce the experimental data in the pressure from about 9 to 22 GPa. For CeAs, the experimental data has been accurately reproduced through the Birch equation using the parameters 69 GPa and 2.6 as reported (Léger, 1993).

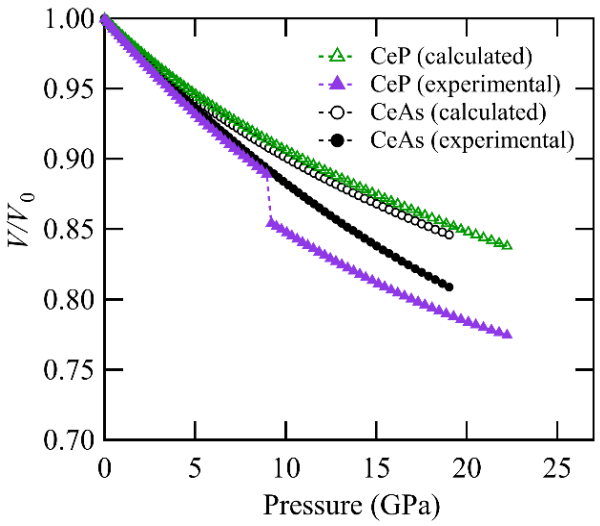

Fig. 3. Reproduced (experimental) relative volume versus pressure curves of CeP and CeAs (filled triangles and filled circles) and their estimated curves (open triangles and open circles) for the existence of stable Ce^{3+} ions in the materials.

Relative volume of CeSb and CeBi

The variation of reproduced experimental relative volume with pressure for CeSb and CeBi is shown in Fig. 4. For CeSb, the experimental data has exactly been reproduced through the Birch equation by using the parameters 71.5 GPa and 2.5 as reported by Léger (1993).

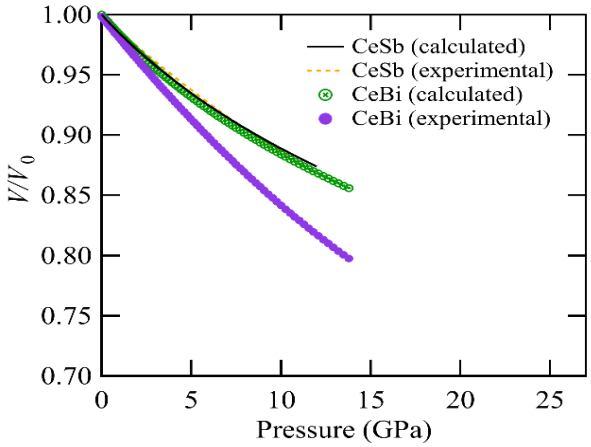

Fig. 4. Reproduced (experimental) relative volume versus pressure curves of CeSb and CeBi (dashed line and filled circles) and the analogous calculated curves (solid line and crossed circles) for Ce^{3+} ions in the materials.

In the case of CeBi, the reproduced data using the parameters $B_0 = 50$ GPa and $B^* = 2.1$ in Eq. (1) precisely corresponds with the experimental data of Léger (1993). The parameters B_0 and B^* used to reproduce the experimental relative volume with pressure for the compounds mentioned earlier are listed in Table 1, along with their lattice parameters at ambient pressure.

Theoretical relative volume for Ce^{3+}

The relative volumes as a function of the pressure of the compounds CeO, CeS, and CeTe from the category of cerium monochalcogenides and the compounds CeP, CeAs, CeSb, and CeBi from cerium monopnictides have been calculated using the Birch equation for the stable trivalent cerium ions in them. The values of the parameters, the bulk modulus B_0 and its first pressure derivative B^*, as mentioned in Eq. (1), are required to know for performing the calculation described above.

The bulk modulus of any stable trivalent rare-earth compound can be obtained from the linear variations of the bulk moduli with the inverse of the volumes of unit cells of the compounds as reported (Léger, 1993). The parameters B_0 and B^* for the calculation of relative volumes with stable Ce^{3+} ions in the mentioned compounds are also listed in Table 1. Values of B_0 and B^*, listed in Table 1 against the mentioned pressure range were used in the calculation

Table 1. Lattice parameter (a), bulk modulus (B_0) and its first pressure derivative (B^*) of some selected compounds

Compound	a (Å)	For the reproduction of experimental relative volume			For the calculation of relative volume with stable Ce^{3+} ions in the compound		
		Pressure Range (GPa)	B_0 (GPa)	B^*	Pressure Range (GPa)	B_0 (GPa)	B^*
CeO	5.089[a]	0 - 3	30	5	All	125.0[a]	5.4[a]
		3 - 23.6	1.58	679			
CeS	5.766[a]	All	83.5	2.2	All	85.0[a]	5.4
	5.780[b]					96.0[b]	4.70[b]
	5.730[c]					87.0[c]	4.83[c]
CeTe	6.360[a]	All	58	8	All	66.0[a]	5.15
	6.360[c]					58.2[c]	5.15[c]
CeP	5.920[a]	0 - 9	64	3	All	78.0[a]	5.4[a]
		9 - 22	30	9.2			
CeAs	6.080[a]	All	69	2.6	All	72.4[a]	5.4
CeSb	6.420[a]	All	71.5	2.5	All	61.8[a]	5.4
CeBi	6.550[a]	All	50	2.1	All	58.2[a]	5.4

[a]Reference (Léger, 1993)

[b]Reference (Svane et al., 1999)

[c]Reference (Bouhemadou et al., 2005)

The calculated relative volumes of CeO, CeS, and CeTe for stable Ce^{3+} ions in them are shown in Fig.1 and Fig. 2 by open circles, open diamonds, and solid lines, respectively. Fig. 3 and Fig. 4 show the calculated relative volumes for CeP, CeAs, CeSb and CeBi by open triangles, open circles, solid lines, and crossed circles, respectively.

Calculation of valence change

The valence of Ce in CeX (X = O, S, Te, P, As, Sb, and Bi) is assumed to vary linearly with the lattice parameter, a (Léger, 1993). According to this idea for a change in lattice parameter of $\{a^{3+}_{\text{calc}}(P_0) - a^{4+}_{\text{calc}}(P_0)\}$, the increase in valence is 1, where $a^{3+}_{\text{calc}}(P_0)$ and $a^{4+}_{\text{calc}}(P_0)$ are the estimated lattice constants at normal pressure with cerium valence 3+ and 4+, respectively. So, the increase in valence, x ($x < 1$) above 3+ can be estimated by the equation,

$$x = \frac{\{a^{3+}_{\text{calc}}(P) - a^{3+x}_{exp}(P)\}}{\{a^{3+}_{\text{calc}}(P_0) - a^{4+}_{\text{calc}}(P_0)\}} \quad (2)$$

where $a^{3+}_{\text{calc}}(P)$ and a^{3+x}_{exp} represent the calculated and experimentally observed lattice constants with cerium valence 3+ and 3+x, respectively.

Cerium monochalcogenides and monopnictides have *fcc* crystal structures, and each cerium ion has a coordination of six. In our calculation, the radii of Ce^{3+} and Ce^{4+} ions at ambient pressure are used as $r^{3+}_{\text{Ce}}(P_0)$=1.034Å, and $r^{4+}_{\text{Ce}}(P_0)$=0.85 Å, respectively, as reported (Léger, 1993). The calculated lattice parameter for a compound with Ce^{3+} ions at ambient pressure P_0 can be expressed as $a^{3+}_{\text{calc}}(P_0) = 2r^{3+}_{\text{Ce}}(P_0) + 2r_X(P_0)$, where X = O, S, Te, P, As, Sb, Bi and $r_X(P_0)$ is the ionic radius of the concern anion. So, the change in lattice parameter between its two ionic states (Ce^{3+} and Ce^{4+}) of cerium in a compound is written as

$$a^{3+}_{\text{calc}}(P_0) - a^{4+}_{\text{calc}}(P_0) = 2\{r^{3+}_{\text{Ce}}(P_0) - r^{4+}_{\text{Ce}}(P_0)\} = 2(1.034 - 0.85)\ \text{Å} = 0.368\ \text{Å}$$

Thus, Eq. (2) becomes,

$$x = \frac{\{a^{3+}_{\text{calc}}(P) - a^{3+x}_{exp}\}}{0.368} \quad (3)$$

$$\text{Or, } x = \frac{a^{3+}_{\text{calc}}(P_0)\left\{\frac{a^{3+}_{\text{calc}}(P)}{a^{3+}_{\text{calc}}(P_0)} - \frac{a^{3+x}_{exp}}{a^{3+}_{\text{calc}}(P_0)}\right\}}{0.368}, \quad (4)$$

$$\text{Or, } x = \frac{a^{3+}_{\text{calc}}(P_0)\left[\left\{\frac{V_{\text{calc}}(P)}{V(P_0)}\right\}^{\frac{1}{3}} - \left\{\frac{V_{\text{exp}}(P)}{V(P_0)}\right\}^{1/3}\right]}{0.368}, \quad (5)$$

where $V(P_0) = \left\{a^{3+}_{\text{calc}}(P_0)\right\}^3$, $V_{\text{calc}}(P) = \left\{a^{3+}_{\text{calc}}(P)\right\}^3$ and $V_{\text{exp}}(P) = \left\{a^{3+x}_{\text{exp}}(P)\right\}^3$ are the estimated volume of the unit cell at ambient pressure with Ce^{3+} ion, the estimated volume at pressure P with Ce^{3+} ion and the experimentally found volume at pressure P with Ce^{3+x} ion, respectively.

The Ce valence at any pressure P is calculated by the relation

$$\text{Valence} = 3 + \frac{a^{3+}_{\text{calc}}(P_0)\left[\left\{\frac{V_{\text{calc}}(P)}{V(P_0)}\right\}^{1/3} - \left\{\frac{V_{\text{exp}}(P)}{V(P_0)}\right\}^{1/3}\right]}{0.368} \quad (6)$$

Results and Discussion

The calculated valences, using Eq. (6), of Ce in CeO, CeS, and CeTe with pressure are shown in Fig. 5. To calculate the valence number of the Ce in CeO, the experimental relative volume $V_{\text{exp}}(P)/V(P_0)$ has been reproduced by the Birch Eq. (1) as shown in Fig. 1. As the reproduction is incompatible with experimental data as reported by Léger (1993) in the pressure range about 3 to 6 GPa, the valence has been calculated up to 23.6 GPa except for the mention pressure range. As represented by solid triangles, the valence of Ce rises spectacularly with the increase of pressure up to 3 GPa, where the valence is 3.26+. As the pressure increases above 6 GPa, the valence decreases slowly with the pressure and reaches 3.16+ at 23.6 GPa. For CeS, the valence remains almost constant with pressure up to about 4 GPa, but above this pressure, the valence increases almost steadily and reaches 3.27+ at about 26 GPa. Starting from 3.0+ at ambient pressure, the valence of cerium in CeTe exhibits a slightly upward trend with increasing pressure but falls again to 3.0+ at around 8 GPa.

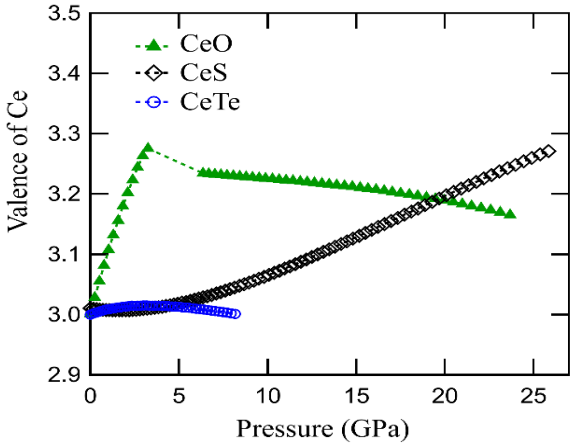

Fig. 5. Calculated valence of Ce as a function of pressure in CeO, CeS, and CeTe.

Fig. 6 shows the calculated valences of Ce in CeP, CeAs, CeSb, and CeBi as a function of pressure. The valence of Ce in CeP grows almost consistently with the increase of pressure until it reaches 3.14+ at nearly 9 GPa. After that, the valence rises dramatically to 3.33+ at about 9.2 GPa because of the isostructural valence-phase transition. From 9.2 to 22.2 GPa, the valence of Ce exhibits no significant change with pressure. For CeAs, the valence of Ce increases non-linearly with pressure from 0 to about 5 GPa. Later, the valence increases almost linearly with further increasing pressure, and at pressure 19 GPa the valence is 3.22+. The valence of Ce, in the case of CeSb, decreases slightly and then grows with pressure. At a pressure of about 12 GPa, the valence is 3.02+. For CeBi, the valence of Ce increases gradually with pressure, and the valence is 3.39+ at around 14 GPa.

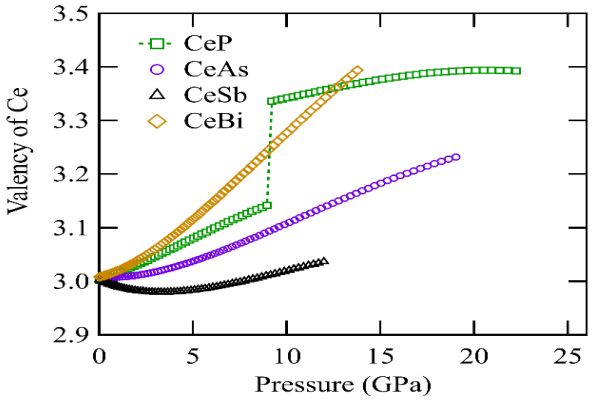

Fig. 6. Calculated valence of Ce as a function of pressure in CeP, CeAs, CeSb, and CeBi.

Our analysis reveals that the distinction between the experimental and calculated pressure-volume curves, as presented in section 2, is due to the valence change of Ce in cerium compounds with pressure. The valence of Ce in any group of compounds does not always increase with the increase of pressure but is also seen to decrease with pressure, as in the cases of CeO, CeTe, and CeSb. The overall trend of the valence changes of Ce in CeAs and CeBi is similar, but the rate of enhancement of valence with pressure in CeBi is much higher than that of CeAs. For the Ce-based compounds Ce*X*, either cerium monochalcogenides or cerium monopnictides, the valence change of Ce does not follow any unique rule, but depends on the constituted *X* ion, i.e., the particular environment around the Ce ion.

In the case of CeO/CeS/CeTe, the average electron transfer from $4f^1$ orbital of Ce to $3s^1/4s^1/6s^1$ orbital of O/S/Te with a certain increase of pressure gives the valence change of Ce at that pressure. In the case of CeP/CeAs/CeSb/CeSb, the average transfer of an electron from $4f^1$ orbital of Ce to $4s^0/5s^0/6s^0/7s^0$ orbital of P/As/Sb/Bi with a certain increase of pressure gives the valence change of Ce at that pressure. That means the valence change of Ce at any high pressure depends on the amount of the mixing of $4f^1$ orbital of the cation Ce^{3+} with the s orbital of the anion at that pressure.

Our finding of the valence change of Ce in cerium monochalcogenides and monopnictides may be useful to the theoreticians to interpret the various properties of these compounds.

Conclusions

The valence change of Ce in Ce*X* (*X*=O, S, Te, P, As, Sb, and Bi) with pressure has been successfully investigated by employing the Birch equation of state. For both CeP and CeBi, the maximum valence change is 0.39+ for the pressure change of 22.2 GPa and 13.8 GPa, respectively. It is found that the valence of Ce in the majority of the compounds increases with the increase of pressure. However, cerium-based compounds cannot ensure a proportionate increase or decrease of cerium valence with pressure. The valence change behavior of cerium with pressure in cerium-based compounds is a unique feature that depends only on the environment around the Ce ion.

Authors' Contributions

Conceptualization: A.H. and M.T.H.; calculation: A.H., M.T.H. and M.S.I.; analysis: A.H., M.T.H. and M.S.I.; original draft preparation: M.S.I. and A.H.; reviewing and editing: A.H., M.T.H. and M.S.I; funding acquisition: A.H. All authors read and approved the final manuscript.

Conflict of Interest

The authors declared that they have no conflict of interest.

Acknowledgment

The corresponding author acknowledges the support of the SUST Research Center for the research grant under project ID PS/2019/1/27.

References

Birch F. Finite Elastic Strain of Cubic Crystals. *Phys. Rev.* 1947; 71**:** 809-824.

Bouhemadou A, Khenata R, Sahnoun M, Baltache H and Kharoubi M. First-principles study of structural, elastic and high-pressure properties of cerium chalcogenides. *Physica B.* 2005; 363: 255-261.

Chattopadhyay T, Burlet P, Rossat-Mignod J, Bartholin H, Vettier C and Vogt O. High-pressure neutron and magnetization investigations of the magnetic ordering in CeSb. *Phys. Rev. B.* 1994; 49(21): 15096.

De SK and Chatterjee S. Electronic and optical properties of CeS under pressure. *Phys. Rev. B.* 1989; 40(18): 12304-12311.

Hannan A, Iwasa K, Kohgi M and Suzuki T. Crystal-lattice anomaly of CeSb under high pressure induced by magnetic polaron formation. *J. Phys. Soc. Japan*. 2000; 69(7): 2358-2359.

Hannan A, Osakabe T, Kohgi M and Iwasa K. High-pressure magnetic phase diagram of CeP studied

by neutron diffraction. *Appl. Phys. A*. 2002; 74 [Suppl.]: S565-S567.

Hayashi Y, Takai S, Matsumura T, Tanida H, Sera M, Matsubayashi K, Uwatoko Y and Ochiai A. Kondo effect in CeX_c (X_c = S, Se, Te) studied by electrical resistivity measurements under high pressure. *J. Phys. Soc. Japan*. 2016; 85: 034704.

Hossain MT and Hannan A. Pressure induced structural phase transition and valence change. *Am. J. Condens. Matter Phys*. 2017; 7(1):1-5.

Hossain MT, Hannan A and Parvin SR. Effect of pressure on the valency of cerium in cerium monochalcogenides and cerium monopnictides. *J Natn Sci. Found. Sri Lanka.* 2015; 43(4)**:** 313-317.

IGOR Pro Version 8.0, WaveMetrics Inc., PO Box 2088, Lake Oswego, OR 97035, USA. https://www.wavemetrics.com/software/igor-pro-800

Léger JM, Vedel I, Redon AM and Rossat-Mignod J. Pressure-volume relationships of cerium monochalcogenides and monopnictides. *J. Magn. Magn. Mater*. 1987; 63 & 64: 49-51.

Léger JM. Chalcogenides and pnictides of cerium and uranium under high pressure. *Physica B*. 1993; 190: 84-91.

Mito T, Nakamura M, Otani M, Koyama T, Wada S, Ishizuka M, Forthaus MK, Lengsdorf R, Abd-Elmeguid MM, and Sarrao JL. Magnetic properties of the pressure-induced ordering state in $YbInCu_4$ investigated with NMR, magnetization, and X-ray diffraction measurements. *Phys. Rev. B.* 2007; 75**:** 134401.

Okayama Y, Takahashi H, Môri N, Kwon YS, Haga Y and Suzuki T. Pressure induced electrical and magnetic properties in Ce-monopnictides; CeX (X = P, As, Sb and Bi). *J. Magn. Magn. Mater*. 1992; 108: 113-114.

Osakabe T, Hannan A, Tachi N, Kohgi M and Kitazawa H. Magnetic *P–T* phase diagram and magnetic structures of CeSb. *Appl. Phys. A*. 2002; 74[Suppl.]: S799-S801.

Svane A, Temmerman M and Szotek Z. Theory of pressure-induced phase transitions in cerium chalcogenides. *Phys. Rev. B*. 1999; 59: 7888.

Svane A, Strange P, Temmerman; WM, Szotek Z, Winter H and Petit L. Pressure-induced valence transitions in rare earth chalcogenides and pnictides. *Physica Status Solidi*. 2001; 223: 105-116.

Ubukata H, Ishida K, Higo Y, Tange Y, Broux T, Tassel Cé and Kageyama H. Pressure-induced structural phase transition in BaHCl. *J. Solid State Chem.* 2022; 312: 123253.

Vedel I, Oki K, Redon AM and Léger JM. Electronic transitions induced by pressure in cerium monochalcogenides and monopnictides. *Physica B*. 1986; 139 & 140: 361-363.

Vedel I, Redon AM, Rossat-Mignod J, Vogt O and Léger JM. Electronic and crystallographic transitions induced by pressure in CeP. *J. Phys. C: Solid State Physic*. 1987; 20: 3439.

J. Bangladesh Acad. Sci. 46(2); 155-164: December 2022 DOI: 10.3329/jbas.v46i2.62168

Journal of Bangladesh Academy of Sciences

Journal homepage: http://www.bas.org.bd/publications/jbas.html

Research Article

Optimization of interval cost multi-objective transportation problem in uncertain parameters: A modified least-cost method

Md. Tariqul Islam and Md. Musa Miah*

Department of Mathematics, Mawlana Bhashani Science and Technology University, Santosh, Tangail, Bangladeshs

ARTICLE INFO

Article History

Received: 12 October 2022
Revised: 28 November 2022
Accepted: 5 December 2022

Keywords: Transportation problem, Multi-objective decision making, Interval cost, Uncertain parameters.

ABSTRACT

This research aims to focus on multi-objective transportation problems, to reduce the cost of transporting goods from various sources or origins to a range of destinations while adhering to a predetermined mathematical framework. By using interval values, the policy maker indicated the source and destination parameters. This work presents a novel approach for finding initial basic feasible solutions (IBFS) that are extremely near to the best ones for a variety of transportation problems is presented. The proposed method can become a milestone in resolving the constraints to solve the transport problem, making the decision-makers regarding logistics and supply chains quite profitable. The prediction model is supported by an illustration drawn from a mathematical view. All the LPPs are evaluated with the help of LINGO.

Introduction

The Transportation Problem (TP) can be treated as a unique mathematical programming issue that seeks to reduce the cost of conveying an item from numerous sources or origins to different destinations. A certain mathematical structure underlies this issue. The standard, straightforward technique is inappropriate for dealing with transportation challenges due to its unique structure. While the supply criteria a_i could be manufactural plants, services, major shipping containers, etc. the destination factors b_j may comprise minor stores, selling stores, etc., Transportation costs, the typical time it takes for goods to be carried, unmet requirements, and other things can all be represented by penalty factors c_{ij} or components of decision variables. The primary goal of the vehicle routing problem is to establish the variety of quantities of a service that should be conveyed from numerous supply sites to diverse transfer stations, while decreasing the overall cost of transportation and lowering the price per unit of merchandise for users. The factors of the transportation problem are the unit costs, or the cost of moving a single entity from one supply location to another, the numbers possible at the supply sites, and the volumes needed at the active nodes.

The following sequences are typically included in the solution process for the transportation issue:

Sequence 1: The transportation problem is expressed mathematically.

Sequence 2: Represent the problem in the form of a matrix.

Sequence 3: Obtaining an outcome of an initial basic feasible solution.

For this study, we have concentrated on sequence 3 to identify effective initial basic workable solutions to the transportation problem. Several researchers have thoroughly studied multi-objective transportation issues. A study entitled "The Delivery of a Material from Numerous Producers to Multiple Communities" (Hitchcock, 1941) initially identified the core

*Corresponding author: <mmusa@mbstu.ac.bd>

transportation issue. The fuzzy convex programming technique for multi-criteria decision making with set-inclusive constraints was later refined by (Soyster, 1973; Chanas and Kuchta, 1996; Bit et al., 1992) with applications to inexact linear programming. Goal programming has been established (Miah et al., 2022; (Uddin et al., 2021) for multi-objective enhancement of the transportation issue in an unpredictable environment utilizing ambiguous non-linear transfer functions. An interactive explanation of the transportation issue with many objectives is shown by Ringuest and Rinks (1987) and Pandian and Natarajan (2010). Using interval cost, source, and destination factors, Das et al. (1999) and Hong (2009) established a model for optimizing a multi-objective transportation issue. In a different piece of work, Akilbasha et al. (2018) developed an original, accurate approach for resolving the complete interval integer transportation problem. Yu et al. (2015) and Ishibuchi and Tanaka (1990) generalized the existing idea of the interactive approach's solution to the multi-objective issue of traffic congestion using interval factors. The collection of all prehistoric solutions was enumerated using Isermann (1979) and Ahmed et al. (2016) approaches for solving a linear multi-objective transportation issue.

The fuzzy time - series network model has a new, ideal solution Murugesan and Kumar, 2013 that have put forth. Heuristic-based modifications (Shimshak et al., 1981; Kirca and Satir, 1990) to Vogel's approximation method that have undergone experimental study and are also part of the modern study's extension by Balakrishnan (1990), Shore (1970), Mathirajan and Meenakshi (2004), Korukoğlu and Balli (2011) and so on.

In this study, we postulate a model for dealing with the multi-objective shipping problem everywhere the origin and location criteria, as well as the decision variables co-efficient, take the shape of intervals. To create an appropriate mathematical model for the multi-objective issue of traffic congestion using periodic coefficients, we made use of various principles. To recognize an initial basic workable solution to a vehicle routing problem, we have utilized certain approaches such as Northwest Corner Method (NWCM), Least Cost Method (LCM), Vogel's Approximation Method (VAM), Row Minimum Method (RMM) and Column Minimum Method (CMM). In order to illustrate the proposed solution method, numerical examples are provided.

Nomenclature

m = Number of sources.

n = Number of destinations.

z = Total transportation cost.

a_i = Supply quantities for source i.

b_j = Demand quantities for destination j.

x_{ij} = Allocation units from origin i to location j.

c_{ij} = TP cost for source i to location j.

Materials and Methods

Interval-based multi-objective transportation issues

The multi-objective transportation problem is when the optimization function coefficient takes the form of closed intervals, namely, $c_{ij} = [c_{Lij}, c_{Uij}]$ and the constraints or parameters are in the deterministic, closed and open intervals.

$$\text{Minimize, } Z = \sum_{i=1}^{m}\sum_{j=1}^{n}[c_{Lij}, c_{Rij}]\ x_{ij}$$

Case-I: Deterministic parameters

Subject to

$$\left.\begin{aligned} &\sum_{i=1}^{m} x_{ij} = a_i, i = 1,2,3....m \\ &\sum_{j=1}^{n} x_{ij} = b_j, j = 1,2,3....n \\ &x_{ij} \geq 0,\ \ i = 1,2...m \ \ and \ \ j = 1,2...n \end{aligned}\right\} . (1)$$

With $\sum_{i=1}^{m} a_i = \sum_{j=1}^{n} b_j$

Case-I1: Closed interval parameters

Subject to

$$\left.\begin{aligned} &\sum_{i=1}^{m} x_{ij} = [a_{Li}, b_{Uj}], \quad i = 1,2,3....m \\ &\sum_{j=1}^{n} x_{ij} = [a_{Li}, b_{Uj}], \quad j = 1,2,3....n \\ &x_{ij} \geq 0, \;\; i = 1,2...m \;\; and \;\; j = 1,2...n \end{aligned}\right\} .....(2)$$

With $\sum_{i=1}^{m} a_{Li} = \sum_{j=1}^{n} b_{Lj} \quad and \quad \sum_{i=1}^{m} a_{Ui} = \sum_{j=1}^{n} b_{Uj}$

Case-III: Open interval parameter

Subject to

$$\left.\begin{aligned} &\sum_{i=1}^{m} x_{ij} = (a_{Li}, b_{Uj}), \quad i = 1,2,3....m \\ &\sum_{j=1}^{n} x_{ij} = (a_{Li}, b_{Uj}), \quad j = 1,2,3....n \\ &x_{ij} \geq 0, \;\; i = 1,2...m \;\; and \;\; j = 1,2...n \end{aligned}\right\} .....(3)$$

With $\sum_{i=1}^{m} a_{Li} = \sum_{j=1}^{n} b_{Lj} \quad and \quad \sum_{i=1}^{m} a_{Ui} = \sum_{j=1}^{n} b_{Uj}$

To derive the comparable conventional multi-objective transportation issue:

$$\text{Minimize. } Z_L(x) = \sum_{i=1}^{m}\sum_{j=1}^{n} c_{Lij}\, x_{ij}$$

$$\text{Minimize. } Z_U(x) = \sum_{i=1}^{m}\sum_{j=1}^{n} c_{Uij}\, x_{ij}$$

Subject to

$$\sum_{j=1}^{n} x_{ij} \leq a_{Ri}, \qquad \sum_{j=1}^{n} x_{ij} \geq a_{Li}$$

$$\sum_{i=1}^{m} x_{ij} \leq b_{Rj}, \qquad \sum_{i=1}^{m} x_{ij} \geq b_{Lj}$$

Procedure for Defining the Transportation Problem

The steps listed below are included in the procedurefor solving a transpiration problem:

1. Create a matrix for the problem and formulate it.

The structure of the vehicle routing problem is correlated to that of LP issues. The price and quantity conditions for each transmitter and the receiver, respectively, serve as the constraints in this model, with the transportation expense acting as the objective function.

2. Find an initial basic feasible solution

To reach this initial basic solution, you can use one of the bellowing approaches:

i. North West Corner Method (NWCM)
ii. Least Cost Method (LCM)
iii. Vogel Approximation Method (VAM)
iv. Row Minima Method (RMM)
v. Column Minima Method (CMM)

Any of the current strategies must produce a solution that satisfies the requirements listed below:

i. A feasible solution is one that satisfies all supply and demand restrictions. The rim condition refers to this.

If m is the number of rows and n is the number of columns, the number of positive allocations must satisfy m + n – 1. A non-degenerate basic viable solution is one that satisfies the requirements above.

Construct an Initial Basic Feasible Solution: The Proposed Method

Step 1: Represent the problem as an original table, a matrix of the problem.

Step 2: Transportation problem must be balanced. If not balanced, have to do.

Step 3: The minimum odd cost is to be determined from all the costs in the original table. Nothing will happen if the original table's cost column does not include an odd cost until the cost cell contains an odd value. All costs must be divided by 2.

Step 4: Create a new table that stores the minimum odd cost as it was in the corresponding cost cell in the table, which will be called the allocation table, and from each cell containing an odd value in the original table, only deduct the chosen lowest odd cost.

Step 5: Using the smallest supply and demand at the beginning of the allocation procedure, place this lowest of price and quantity in the initial allocation cells of the table created in Step 4 instead of the values of the allocation cells with odd values. The column should be removed if the demand is fulfilled, and when it supplied remove the row.

Step 6: Assign the lowest supply or demand at the location that was selected in the allocation cost values table by determining the minimal allocation cost values. To make the smallest allocation, a different allocation cost value should be selected rather than the same allocation cost values and deleted column again, if the demand is satisfied. Supply can end the row.

Step 7: Step 6 should be repeated until supply or demand is no longer.

Step 8: Every allocation should be returned to the original table.

Step 9: Therefore, the total of the original table's cost and matching assigned value may be determined.

3. Check the original answer for optimality

Numerical Illustrations

Example-1 (Closed Interval Parameters)

A firm has three manufacturing plants (origins) with a capacity of [5, 7], [0, 2], and [8, 12] units each. These facilities are A1, A2, and A3. There are a requirement of [6, 8], [4, 6], [2, 4], and [1, 3] units for each of these units to be delivered to the four storerooms B1, B2, B3, and B4. Following are the shipping costs and times from firms to storerooms:

$$\mathbf{C} = \begin{bmatrix} [2,4] & [3,5] & [11,15] & [7,9] \\ [1,5] & [0,2] & [6,8] & [1,3] \\ [5,9] & [8,12] & [15,17] & [9,13] \end{bmatrix}$$

Solution

Mathematical example 1 has been used to demonstrate the solution process.

$$\text{Minimize,} \quad Z = \sum_{i=1}^{3}\sum_{j=1}^{4}[c_{Lij}, c_{Rij}]\ \mathrm{x_{ij}}$$

Subject to

$$\sum_{j=1}^{4} x_{1j} = [5,7], \quad \sum_{j=1}^{4} x_{2j} = [0,2], \quad \sum_{j=1}^{4} x_{3j} = [8,12],$$

$$\sum_{i=1}^{3} x_{i1} = [6,8], \quad \sum_{i=1}^{3} x_{i2} = [4,6], \quad \sum_{i=1}^{3} x_{i3} = [2,4],$$

$$\sum_{i=1}^{3} x_{i4} = [1,3], \qquad x_{ij} \geq 0, \ \ i = 1,2,3 \ \ and \ \ \ j = 1,2,3,4.$$

With the equivalent cases

Subject to

$$\sum_{j}^{4} x_{1j} \leq 7, \quad \sum_{j}^{4} x_{1j} \geq 5, \quad \sum_{j}^{4} x_{1j} \leq 2, \quad \sum_{j}^{4} x_{1j} \geq 0,$$

$$\sum_{j}^{4} x_{3j} \leq 12, \quad \sum_{j}^{4} x_{3j} \geq 8, \sum_{i}^{3} x_{i1} \leq 8, \quad \sum_{i}^{3} x_{i1} \geq 6,$$

$$\sum_{i}^{3} x_{i2} \leq 6, \quad \sum_{i}^{3} x_{i2} \geq 4, \quad \sum_{i}^{3} x_{i3} \leq 4,$$

$$\sum_{i}^{3} x_{3i} \geq 2, \quad \sum_{i}^{4} x_{i4} \leq 3, \quad \sum_{i}^{4} x_{i4} \geq 1.$$

We consider the lower cost of intervals of the matrices as one metric, i.e., C_L, and similarly consider the matrices for the upper intervals i.e.; C_U.

$$C_L = \begin{bmatrix} 2 & 3 & 11 & 7 \\ 1 & 0 & 6 & 1 \\ 5 & 8 & 15 & 9 \end{bmatrix}$$

And

$$C_U = \begin{bmatrix} 4 & 5 & 15 & 9 \\ 5 & 2 & 8 & 3 \\ 9 & 12 & 17 & 13 \end{bmatrix}$$

Firstly, we find the lower cost of an interval of the transportation problem.

Utilizing the algorithm of the suggested approach:

The provided problem is discovered to be balanced. Since the total supplies are equal to the total demands.

All price cells in transportation (Table 1) have the lowest odd cost of 1, shown in cost cells (2, 1) and (2, 4).

The transportation's least odd cost is still in cells (2, 1) and (2, 4), but all other odd-valued price cells are removed from this odd expense in table 2. For example, in Transportation Table 1's cost cell (1, 2), the value is 3, but in Table 2, it is 2 = (3 - 1).

Table 1. Data of the lower cost of interval

Facilities	Warehouses				Capacity
	B_1	B_2	B_3	B_4	
A_1	2	3	11	7	5
A_2	1	0	6	1	0
A_3	5	8	15	9	8
Requirement	6	4	2	1	13

Table 2. All the cost cells are subtracted by the minimum odd cost

Facilities	Warehouses				Capacity
	B_1	B_2	B_3	B_4	
A_1	2	2	10	6	5
A_2	1	0	6	1	0
A_3	4	8	14	8	8
Requirement	6	4	2	1	13

Table 3. Several cells in the Allocation table are assigned

Facilities	Warehouses				Capacity
	B_1	B_2	B_3	B_4	
A_1	1	4	10	6	5/1/0
	2	2			
A_2				0	0/0
	1	0	6	1	
A_3	5		2	1	
	4	8	14	8	8/3/2/0
Requirement	6/5/0	4/0	2/0	1/1/0	13

According to step 5 of the proposed method, the smallest amount of either supply or demand that has been provided in cells (2, 4) is 0. This value is assigned, and it is established that the supply is fulfilled. Whatever row in A_2 needs to be used up.

The only cells to be considered are those in rows A_1 and A_3. If cell (1, 1) and (1, 2) has the weakest cell value 2. However, of these two cells, 4 can only receive the least allocation (1, 2). After assigning this sum, column B_2 has now been destroyed.

Once more, it is discovered that cell value 2 is the lowermost cost in the follicular cells that occur in the cells (1, 1). Therefore, there is a minimum allocation of 1 created in cell (1, 1). Therefore, no additional calculations should take row A_1 cells into account.

One cell from row A3 alone needs to be taken into account. The least expensive options are 4,8,14, respectively, in Table 3's cells (3, 1), (3, 4), and (3, 3). Finally finish the allocation by distributing 5, 1, and 2 to cells in table 3 marked (3, 1), (3, 4), and (3, 3), respectively, in Table 3.

All these transfers are made to transportation (Table 1), which is included in the final allocation Table 4. The initial basic feasible solution in line with the provided approach is shown by the discovery that there are 6 fundamental cells in this table, indicating the number of fundamental cells.

Table 4. Lower Initial basic feasible solution according to proposed method

Facilities	Warehouses				Capacity
	B_1	B_2	B_3	B_4	
A_1	1	4	11	7	5
	2	3			
A_2	1	0	6	0	0
				1	
A_3	5	8	2	1	8
	5		15	9	
Requirement	6	4	2	1	13

The solution to a given problem is

$$x_{11}=1, \quad x_{12}=4, \quad x_{24}=0,$$
$$x_{31}=5, \quad x_{33}=2, \quad x_{34}=1.$$

The total lower cost, Z_L

$$= 1\times2+4\times3+0\times1+5\times5+2\times15+1\times9$$
$$=2+12+25+30+9=78$$

Secondly, we find to the upper cost of interval of the transportation problem.

Table 5. Data of the upper cost of interval

Facilities	Warehouses				Capacity
	B_1	B_2	B_3	B_4	
A_1	4	5	15	9	7
A_2	5	2	8	3	2
A_3	9	12	17	13	12
Requirement	8	6	4	3	21

Utilizing the algorithm of the suggested approach:

The provided problem is discovered to be balanced. Due to the fact that the total supplies are equal to the total demands.

All price cells in transportation (Table 5) have the lowest odd cost of 3, shown in cost cells (2, 4).

The transportation's least odd cost is still in cell (2, 4), but all other odd-valued price cells are removed from this odd expense in Table 6. For example, in Transportation Table 5's cost cell (1, 2), the value is 5, but in Table 6, it is 2 = (5 – 3).

Table 6. All the cost cells are subtracted by the minimum odd cost

Facilities	Warehouses				Capacity
	B_1	B_2	B_3	B_4	
A_1	4	2	12	6	7
A_2	2	2	8	3	2
A_3	6	12	14	10	12
Requirement	8	6	4	3	21

Table 7. Several cells in the Allocation table are assigned

Facilities	Warehouses				Capacity
	B_1	B_2	B_3	B_4	
A_1	1 4	6 2	12	6	7/1/0
A_2	2	2	8	2 3	2/0
A_3	7 6	12	4 14	1 10	12/5/4/0
Requirement	8/7/ 0	6/0	4/ 0	3/1/ 0	21

According to step 5 of the proposed method, the smallest amount of either supply or demand that has been provided in cells (2, 4) is 1. This value is assigned, and it is established that the supply is fulfilled. Whatever row in A_2 needs to be used up.

The only cells to be considered are those in rows A1 and A3. If the cell (1, 1) and (1, 2) has the weakest cell value 2. However, of these two cells, 5 can only receive the least allocation (1, 2). After assigning this sum, column B_2 has now been destroyed.

Once more, it is discovered that cell value 2 is the lowermost cost in the follicular cells that occur in the cells (1, 1). Therefore, there is a minimum allocation of 1 created in cell (1, 1). Therefore, no additional calculations should take row A_1 cells into account.

One cell from row A_3 alone needs to be taken into account. The least expensive options are 6, 10, and 14, respectively, in Table 7's cells (3, 1), (3, 4), and (3, 3). Finally, finish the allocation by distributing 6, 1, and 3 to the cells (3, 1), (3, 4), and (3, 3), respectively, in Table 7.

All these transfers are made to transportation (Table 5), which is included in the final allocation Table 8. The initial basic feasible solution in line with the provided approach is shown by the discovery that there are 6 fundamental cells in this table, indicating the number of fundamental cells.

Table 8. Upper Initial basic feasible solution according to the proposed method

Facilities	Warehouses				Capacity
	B_1	B_2	B_3	B_4	
A_1	1 4	6 5	15	9	7
A_2	5	2	8	2 3	2
A_3	7 9	12	4 17	1 13	12
Requirement	8	6	4	3	21

The solution to a given problem is

$$x_{11} = 1, \quad x_{12} = 6, \quad x_{24} = 2,$$
$$x_{31} = 7, \quad x_{33} = 4, \quad x_{34} = 1.$$

The total upper cost, Z_U

$= 4\times1+5\times6+3\times2+9\times7+4\times17+1\times13$
$=4+30+6+63+68+13$
$=184$

Finally, the total transportation cost is Z = [78,184].

Example-2 (Deterministic Parameters)

A firm has three manufacturing plants (origins) with a capacity of **6, 1**, and **10** units each. These facilities are A1, A2, and A3. There is a requirement of **7, 5, 3,** and **2** units to be delivered to the four storerooms B1, B2, B3, and B4. Following are the shipping costs and times from firms to storerooms:

$$C = \begin{bmatrix} [2,4] & [3,5] & [11,15] & [7,9] \\ [1,5] & [0,2] & [6,8] & [1,3] \\ [5,9] & [8,12] & [15,17] & [9,13] \end{bmatrix}$$

Example-3 (Open Interval Parameters)

A firm has three manufacturing plants (origins) with a capacity of (6, 8), (8, 10), and (17, 19) units each. These facilities are A1, A2, and A3. There are a requirement of (4, 6), (7, 9), (6, 8), and (13, 15) units for each of these units to be delivered to the four storerooms B1, B2, B3, and B4. Following are the shipping costs and times from firms to storerooms

$$C = \begin{bmatrix} [10,12] & [30,32] & [50,54] & [10,12] \\ [70,74] & [30,32] & [40,42] & [60,62] \\ [40,42] & [8,10] & [70,74] & [20,24] \end{bmatrix}$$

Result Comparison and Graphical Interpretation

The entire transportation costs for the suggested strategy, the existing approaches, and the optimal solution are compared in Table 9. The optimal algorithm that provides a solution at the lowest cost is used in the comparison to determine which option has the lowest cost.

Table 9 shows that the new method provides the best IBFS when compared to other ways now in use since, on average, it provides the best price for the transportation issue. The achievement of IBFS is often displayed in Table 10. This data demonstrates the proposed method's superior performance. Our suggested approach has been used in several examples, and the solution results were superior to those of the other ways already used to address the transportation issue.

Table 9. Comparative Analysis of Initial Basic Feasible Solution

Methods	Total cost, Z		
	Ex-1	**Ex-2**	**Ex-3**
North-West Corner	[86,202]	[116,166]	[970,1074]
Least Cost	[86,196]	[112,160]	[734,822]
Vogel's Approximation	[78,186]	[102,151]	[734,822]
Row Minima	[86,196]	[112,160]	[1010,1114]
Column Minima	[86,202]	[116,166]	[734,822]
Proposed Approach	**[78,184]**	**[102,150]**	**[734,822]**
Optimal Solution	[77,184]	[100,150]	[698,790]

Table 10. Difference between IBFS and optimal solution

Methods	Difference between IBFS and optimal solution		
	Ex-1	**Ex-2**	**Ex-3**
NWCM	[9,18]	[16,16]	[92,284]
LCM	[9,12]	[12,10]	[36,32]
VAM	[1,2]	[2,1]	[36,32]
RMM	[9,12]	[12,16]	[312,324]
CMM	[9,20]	[16,16]	[36,32]
Proposed	**[1,0]**	**[2,0]**	**[36,32]**

Figures 1, 2, and 3 shows that the initial basic feasible solutions superior to the results obtained by conventional algorithms, which are either optimal or near to optimal. Another time, the performance of the solution changes in different ways, which is also possible in the case of the proposed method.

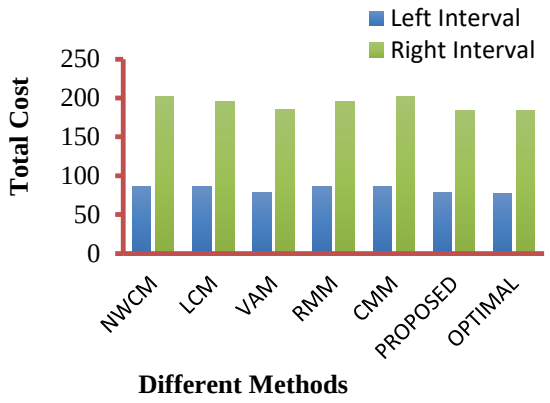

Fig. 1. Graphical Illustration of Various Solutions of Example-1

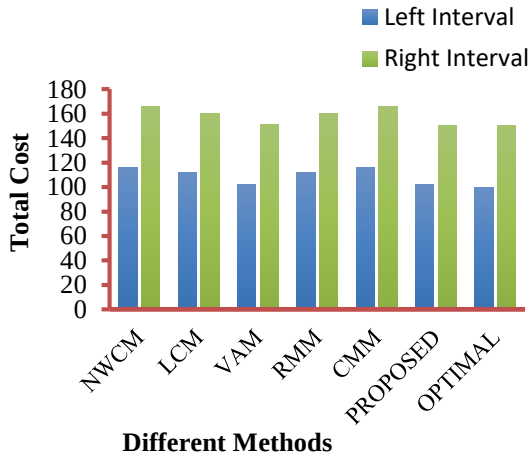

Fig. 2. Graphical Illustration of Various Solutions of Example-2

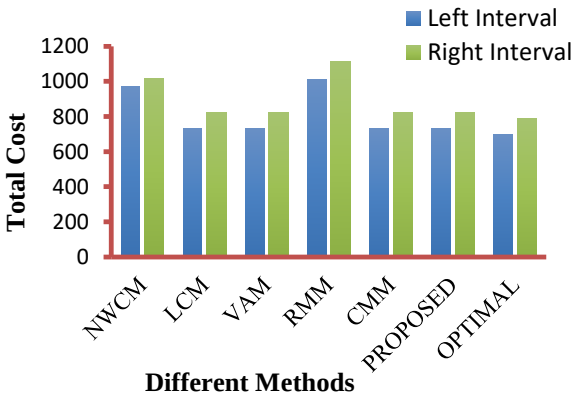

Fig. 3. Graphical Illustration of Various Solutions of Example-3

This research is conducted to support the method's typical performance. During such an approach, it was discovered that the suggested model performed better than some of the other procedures in the chart, as indicated in Figures 4 and 5, correspondingly.

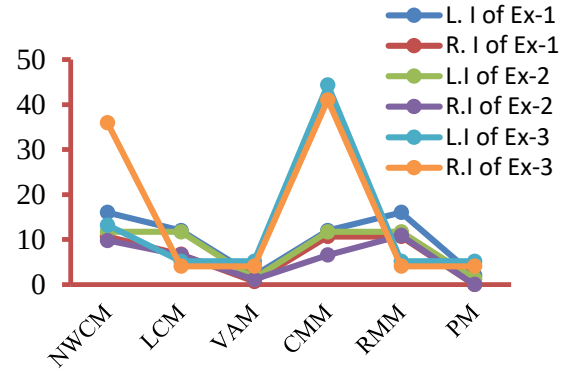

Fig. 4. Graphical Represented of Performance of IBFS

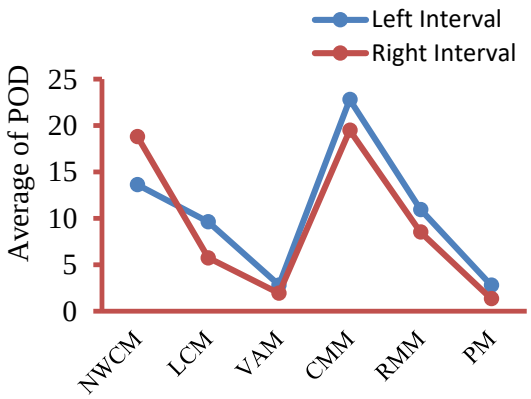

Fig. 5. Graphical Representation of Mean of POD

Table 11. Percentage of Disparity (POD) and Mean of POD

0Methods	Percentage of Disparity (POD)			Mean of POD
	Ex-1	Ex-2	Ex-3	
NWCM	[11.69,9.79]	[16,10.67]	[13.19,35.95]	[13.63,18.8]
LCM	[11.69,6.53]	[12,6.67]	[5.16,4.05]	[9.62,5.75]
VAM	[1.3,1.09]	[2,0.67]	[5.16,4.05]	[2.82,1.93]
RMM	[11.69,6.53]	[12,10.67]	[44.7,41.02]	[22.8,19.5]
CMM	[11.69,10.87]	[16,10.67]	[5.16,4.05]	[10.95,8.53]
Proposed	**[1.3,0]**	**[2,0]**	**[5.16,4.05]**	**[2.8, 1.35]**

The performance of Percentage of Disparity (POD) and Mean of POD is frequently shown in Table 11.

Conclusions

The carrying cost is an essential component of the overall the cost configuration for any firm. The transportation issue was expressed as a linear programming problem, which was then resolved using the usual LP solvers to get the initial basic feasible solutions (IBFS) and the best option. In this research, we use mathematical illustration to describe the approach and effectiveness of our proposed method. 'LINGO' software is used to create the ideal solution. Comparative analysis of the solutions using the suggested method and the other ways already in use, is illustrated using a sample problem. We already have some basic, workable solutions that are closer to the ideal ones, but the suggested method still produces predictable results.

The analysis of transportation issues is made more accessible by the suggested method's reducing the odd cost coefficients to even numbers, providing a solution far superior to other approaches. It affects lowering the cost of transportation in the objective function, which will assist in achieving the goal of maximizing profit. Finally, validating transportation costs utilizing the suggested strategy may produce a unique initial basic achievable solution. It may mark a turning point in removing obstacles that stand in the way of resolving the transport issue.

Acknowledgment

The authors greatly appreciated the reviewers' constructive criticism and recommendations. This study was funded by the NST Fellowship research program 2020–21, registration number 569, and merit serial number 223.

Conflicting interests

The authors acknowledge no potential conflicts of concern.

References

Ahmed MM, Khan AR, Uddin MS and Ahmed F. A new approach to solve transportation problems, *Open. J. Opti.* 2016; 5(1): 22-30.

Akilbasha A, Pandian P and Natarajan G. An innovative exact method for solving fully interval integer transportation problems. *Infor. Medi. Unlocked.* 2018; 11:95-99.

Balakrishnan N. Modified Vogel's approximation method for the unbalanced transportation problem. *Appl. Math. Letters.* 1990; 3(2):9-11.

Bit AK, Biswal MP and Alam SS. Fuzzy programming approach to multi-criteria decision making transportation problem. *Fuzzy sets syst.* 1992; 50(2): 135-141.

Chanas S and Kuchta D. Multi-objective programming in optimization of interval objective functions—a generalized approach. *Eur. J. Oper. Res.* 1996; 94(3): 594-598.

Das SK, Goswami A and Alam SS. Multi-objective transportation problem with interval cost, source and destination parameters. *Eur. J. Oper. Res.* 1999; 117(1): 100-112.

Hitchcock FL. The distribution of a product from several sources to numerous localities. *J. Math. Phy.* 1941; 20: 224-230.

Hong DH. Interval valued solution of multi-objective problem with interval cost, source and destination parameters. *Int. J. Fuzzy Logic Intell. Syst.* 2009; 9(1): 42-46.

Isermann H. The enumeration of all efficient solutions for a linear multiple-objective transportation problem. *Naval Res. Log. Quart.* 1979; 26(1): 123-139.

Ishibuchi H and Tanaka H. Multi-objective programming in optimization of the interval objective function. *Eur. J. oper. Res.* 1990; 48(2): 219-225.

Kirca O and Şatir A. A heuristic for obtaining and initial solution for the transportation problem. *J. Oper. Res. Soc.* 1990; 41(9): 865-871.

Korukoğlu S and Balli S. An improved Vogel's approximation method for the transportation problem. *Math. Comput. Applica.* 2011; 16(2): 370-381.

Mathirajan M and Meenakshi B. Experimental analysis of some variants of Vogel's approximation method. *Asia-Pac. J. Oper. Res.* 2004; 21(04): 447-462.

Murugesan S and Kumar BR. New optimal solution to fuzzy interval transportation problem. *Inter. J. Eng. Sci. Tech.* 2013; 3(1): 188-192.

Uddin MS, Miah M, Khan MA and Arjani A. Goal programming tactic for uncertain multi-objective transportation problem using fuzzy linear membership function. *Alex. Engin. J.* 2021; 60: 2525-2533.

Miah MM, Rashid A, Khan AR and Uddin MS. Goal programming approach for multi-objective optimization to the transportation problem in uncertain environment using fuzzy non-linear membership functions. J. Bangladesh Acad. Sci. 2022; 56(1): 101-115.

Pandian P and Natarajan G. A new approach for solving transportation problems with mixed constraint. *J. Phy. Sci.* 2010: 14: 53-61.

Ringuest JL and Rinks DB. Interactive solutions for the linear multi-objective transportation problem. *Eur. J. Oper. Res.* 1987; 32(1): 96-106.

Soyster AL. Convex programming with set-inclusive constraints and applications to inexact linear programming. *Oper. Res.* 1973; 21(5):1154-1157.

Shore HH. The transportation problem and the Vogel approximation method. *Dec. Sci*. 1970; *1*(3-4), 441-457.

Shimshak D, Kaslik JA and Barclay T. A modification of Vogel's approximation method through the use of heuristics. *Infor. Syst. Oper. Res.* 1981; 19(3): 259-263.

Yu VF, Hu KJ and Chang AY. An interactive approach for the multi-objective transportation problem with interval parameters. *Inter. J. Prod. Res*. 2015; 53(4): 1051-1064.

J. Bangladesh Acad. Sci. 46(2); 165-173: December 2022 DOI: 10.3329/jbas.v46i2.63415

Journal of Bangladesh Academy of Sciences

Journal homepage: http://www.bas.org.bd/publications/jbas.html

Research Article

Changes in morpho-physiological and yield attributes of *Sesamum indicum* under waterlogging at different growth stages

Taufika Islam Anee, Parimal Kanti Biswas and Mirza Hasanuzzaman*

Department of Agronomy, Faculty of Agriculture, Sher-e-Bangla Agricultural University, Dhaka, Bangladesh

ARTICLE INFO

Article History

Received: 13 November 2022
Revised: 12 December 2022
Accepted: 15 December 2022

Keywords: Abiotic stress, Anoxia, Flooding, Hypoxia, Oilseed crop, Reproductive stage

ABSTRACT

To understand the responsive nature to excess water, a pot experiment was conducted at different growth stages of sesame (*Sesamum indicum* L. cv. BARI Til-4). The waterlogging stress at each stage was set to three durations, viz. 2, 4, and 6 days. Twelve different treatment combinations were replicated three times and arranged in a completely randomized design. Different morpho-physiological and yield parameters were measured after the completion of the longest stress duration (6 days). The data revealed that sesame is vulnerable to excess water conditions, and the sensitivity is positively correlated with the stress duration. Plant biomass, leaf area, SPAD value, and the yield attributes recorded are observed to be declined with the increment of stress duration. Another important finding is that among the three growth stages of sesame, the reproductive stage is the most sensitive stage, which hardly withstands waterlogging. The stress at the vegetative stage affect yield parameters minimally.

Introduction

Waterlogging is one of the most devastating abiotic stresses that negatively affect crop production. More than 16% of the cultivated area is globally prone to waterlogging exposure (Ploschuk et al., 2018). In addition, climate change is accelerating the erratic incidence of precipitation, making the situation worse for global crop production. Many natural and anthropogenic causes, such as heavy rainfall, flash flood, unplanned irrigation or drainage, dam failure, etc., are responsible for causing waterlogging (Anee et al., 2019). The effect of waterlogging stress varies depending on crop species, duration, soil type, water level, plant growth stage, and other environmental factors (Hasanuzzaman et al., 2017). Different types of morpho-physiological, anatomical, and biochemical alterations such as growth reduction, leaf senescence, chlorosis, wilting, flower and fruit dropping, delay in maturity, disease infestation, etc., are some of the most common phenomena caused by waterlogging stress (Jia et al., 2021; Pan et al., 2021). Oxygen availability gets reduced proportionately to the magnitude of waterlogging, resulting in hypoxia or oxygen deficiency for short-duration stress and anoxia or absence of oxygen for longer durations (Olorunwa et al., 2022). Plant anaerobic respiration occurs due to a lack of oxygen which reduces energy and gas exchange leading to cell death in crops sensitive to waterlogging and reduced yield (Gibbs and Greenway, 2003; Pan et al., 2021). To minimize the losses, it is necessary to find out the possible mechanisms of plants under waterlogging and to develop varieties tolerant to waterlogging.

Sesame (*Sesamum indicum* L.) is the queen of oilseed crops globally and is categorized as healthy food, especially in Asian countries (Myint et al., 2020). According to FAOSTAT (2021), more than

*Corresponding author: <mhzsauag@yahoo.com>

six million tons of sesame seeds were grown globally in approximately 12 million hectares of land, of which almost 97% of production belongs to Asia and Africa. Sesame is cultivated during the summer season in tropical and subtropical regions and hence faces several environmental adversities that restrict sesame cultivation and cause yield loss. Especially due to its susceptibility to waterlogging, farmers are losing interest in cultivating sesame. This poses a threat to national oil production, and a large amount of foreign currency is paid out to meet the demand. Therefore, it's a prime need to research on developing high-yielding varieties of sesame tolerant to environmental constraints like drought, waterlogging, salinity, etc., as sesame is cultivated during the monsoon it is very likely to get exposed to waterlogging. Several studies have demonstrated different sesame genotypes' waterlogging-induced growth and yield reduction.

Variations in growth stages, stress duration, water level, and genotypes of waterlogging stress have been documented to affect sesame growth and yield negatively. Linh et al. (2021) screened five sesame varieties for waterlogging tolerance and reported a time-dependent reduction of growth and yield parameters. A growth stage-dependent study with sesame revealed that at vegetative and flowering stages, the plant height, stem diameter, and chlorophyll (chl) content were reduced upon exposure to waterlogging for 2 and 3 days (Jung et al., 2019). Despite several similar literatures on sesame under waterlogging, there needs to be more information on duration and growth stage-dependent studies with sesame cultivars. And as an oilseed crop with the scope to be cultivated both in the tropics and sub-tropics, it is necessary to conduct in-depth studies of sesame responses and mechanisms under waterlogging stress. Therefore, this experiment was designed to understand sesame's duration-dependent responses at different waterlogging stages.

Materials and Methods

Experimental Materials, Treatments, and Design

Clean and uniform seeds of sesame (*Sesamum indicum* cv. BARI Til-4) were sown in pots (14 L) and provided with well-prepared soil containing recommended doses of manures and fertilizers. Three different durations (2, 4, and 6 days) of waterlogging were considered at three growth stages: vegetative, reproductive, and maturity stages. Twenty-one days after sowing (DAS) was considered as the starting of vegetative stage, for the reproductive and maturity stages; it was 35 and 55 DAS, respectively. Water was added to create an anoxic condition by maintaining a height 3 cm above the soil level. After completion of treatment, water was drained out from the pots and irrigated as required for the rest of the time. For every three stages, a respective control was irrigated regularly as required, and data were collected after completing the longest waterlogging treatment at each stage. Pots were arranged in a completely randomized design consisting of 12 waterlogging treatments in three replications.

Measurement of Crop Growth Parameters

The height of plants was recorded from the ground level up to the tip of the leaf in centimeters (cm) using a measuring scale. The average height of five plants was considered as the plant height for each pot.

Three sample plants were uprooted from each pot randomly and washed in water. Then the plants were weighed in a balance and averaged to have fresh weight (FW) plant^{-1}. Three sample plants, after weighing for FW was dried in an electric oven, maintaining 60 °C for 48 hours. Then weighed in an electric balance and averaged them to have dry weight (DW) plant^{-1}. The average number of leaves from five plants was considered as the total number of leaves plant^{-1}.

The leaf area plant^{-1} was determined by measuring the length (cm) of 5 leaves, and counting the total number of leaves per plant, applying the following equation, $S=0.3552\times C^2$, where S=leaf area (cm^2) and C=leaf length (cm) and then multiplying the leaf area by the total number of leaves per plant to obtain the total leaf area plant^{-1} (cm^2).

Measurement of Leaf Greenness

Three leaves were randomly selected from each pot. The top and bottom of each leaflet were measured with Soil-Plant Analysis Development (SPAD) meter as SPAD value and then averaged.

Determination of Yield

The total number of capsule plant^{-1} was counted from five randomly selected plants and then averaged. Ten capsules from each pot were selected, and seeds were counted from each capsule and then averaged. One thousand clean sun-dried seeds were counted from the sample plants' seed stock and weighed using an electronic balance.

The grains were separated by threshing, and the plants were sun-dried and weighed. The biological yield was calculated by using the following formula:

Biological yield = Grain yield + Straw yield.

Statistical Analysis

The data obtained for different parameters were statistically analyzed using XLSTAT v. 2015 software (Addinsoft, 2016), and mean separation was done by LSD at a 5% level of significance.

Results and Discussion

The plant height showed no significant changes during the vegetative stage of seedling growth after waterlogging. But it reduced significantly at the reproductive stage when waterlogged for 4 and 6 days. At maturity, plant height decreased by 10 and 17% in plants waterlogged for 4 and 6 days, respectively, compared to the control plants (Fig. 1A).

As plant height showed little changes under waterlogging at the vegetative stage, there was also a lesser effect on above-ground FW plant^{-1}, except the plants were waterlogged for 6 days. But, in the case of the reproductive stage, FW reduced by 33, 50, and 54% after waterlogging for 2, 4, and 6 days, respectively. At maturity, 4, and 6 days of waterlogging duration reduced their FW by 35 and 36%, respectively (Fig. 1B).

As shown in Fig. 1C, DW remarkably reduced in plants waterlogged at the reproductive stage, but at the vegetative stage only affected the longer duration (6 days) of waterlogging treatment with a 37% reduction. However, plants waterlogged only for 4 and 6 days at maturity showed 40 and 50% lower DW, whereas waterlogging for 2 days was about 5% higher (Fig. 1C).

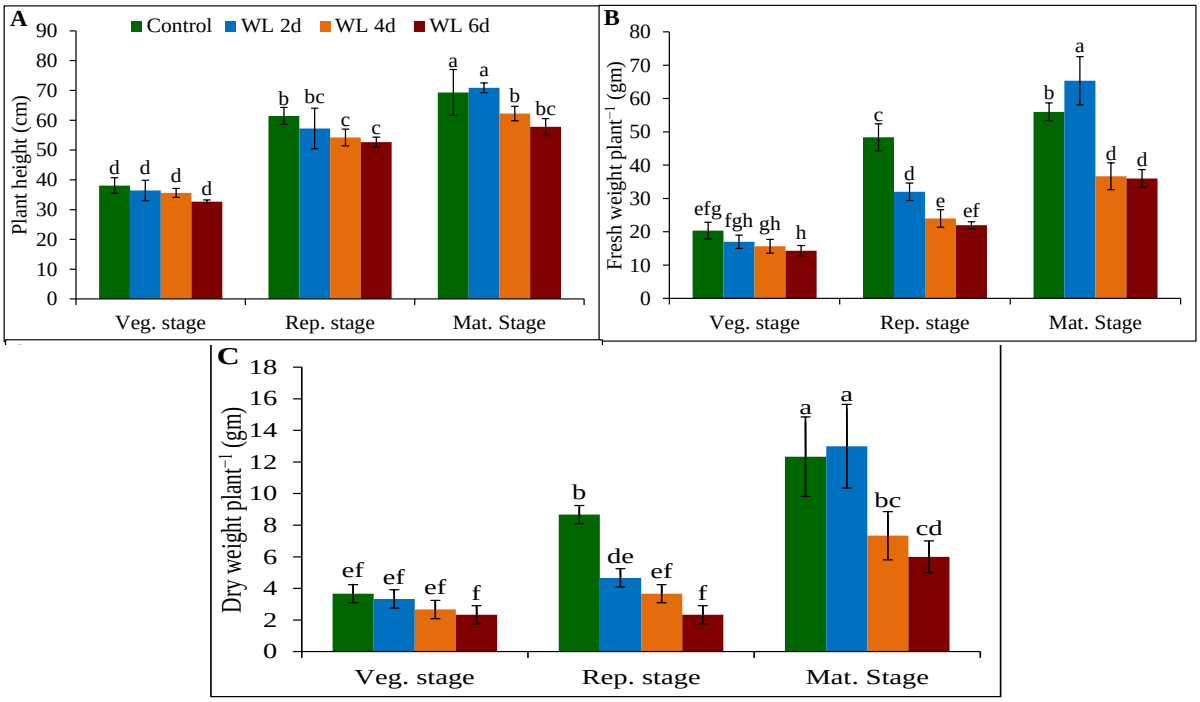

Fig. 1. Plant height (A), above-ground fresh weight (FW) plant^{-1} (B), and above-ground dry weight (DW) plant^{-1} (C) of sesame as affected by waterlogging stress at different growth stages. Mean (±SD) was calculated from three replicates for each treatment. Values in a column with different letters are significantly different at $p \leq 0.05$ applying LSD test.

Significant reduction of leaves plant^{-1} has been observed in plants waterlogged either during the reproductive stage or maturity stage. Waterlogging treatments during the reproductive stage showed a lower number of leaves plant^{-1} by 44, 55 and 59% at 2, 4, and 6 days of waterlogging, respectively, compared to the corresponding well-drained plants (Fig. 2A). Plants waterlogged for 4 and 6 days at maturity stage showed a reduced number of leaves plant^{-1}, but higher in plants waterlogged for 2 days.

Though the leaf numbers were not significantly affected by waterlogging during the vegetative stage, leaf area reduced remarkably in the plants waterlogged for 6 days at this stage (Fig. 2B). This experiment also showed a marked reduction of leaf area by 30, 71, and 77% at the reproductive stage and 11, 70, and 76% at maturity stage in plants waterlogged for 2, 4, and 6 days, respectively, compared to the control (Fig. 2B).

SPAD reading which is the indicator of the chl content of the leaf, showed a lower value in the leaves of waterlogged plants compared to the control plants. In case of the vegetative stage, only 6 days of waterlogging reduced the SPAD values (13%), whereas at reproductive and maturity stages, even 2 days of waterlogging showed a lower SPAD reading and gradually declined with the increment of stress duration. At vegetative stages, 23, 30, and 37%, and at maturity stage 12, 16, and 19%, lower SPAD values were recorded after 2, 4 and 6 days of waterlogging, respectively (Fig. 2C).

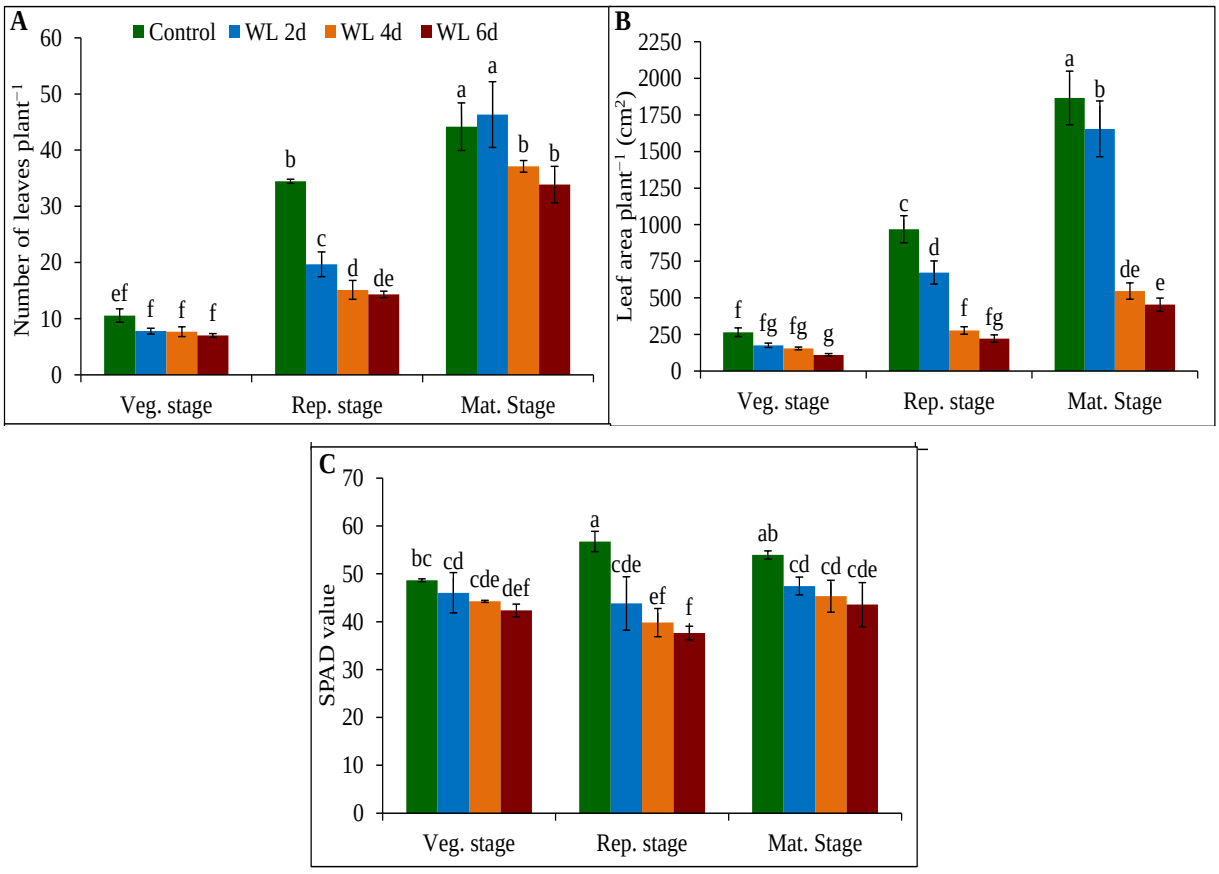

Fig. 2. (A) Number of leaves plant^{-1}, (B) leaf area plant^{-1}, and (C) SPAD value of leaves affected by different durations of waterlogging at different growth stages in sesame crop. Mean (±SD) was calculated from three replicates for each treatment. Values in a column with different letters are significantly different at $p \leq 0.05$ applying LSD test.

Waterlogging significantly reduced the number of capsule plant^{-1} irrespective of the stage and duration at which waterlogging was imposed. The plant waterlogged for 6 days during the reproductive stage showed the lowest number of capsule plant^{-1} (Fig. 3A), which is about 67% lower than the control plants. For 6 days of waterlogging at vegetative or maturity stages number of capsule plant^{-1} reduced by 59%, and for 4 days, it was 47% in both cases compared to the control plants (Fig. 3A).

In this experiment number of seeds capsule^{-1} reduced when waterlogging was imposed at the maturity stage for 2, 4 and 6 days and at the vegetative or reproductive stage for 6 days (Fig. 3B). However, the number of seed capsule^{-1} after 2, 4, and 6 days of waterlogging stress at the maturity stage was respectively 24, 26, and 30% lower than the control plants.

The lowest value of 1000-seed weight was recorded in plants waterlogged at the reproductive stage for four and six days, which were respectively 21 and 25% lower than the control plants (Fig. 3C). Though waterlogging for only 2 days could not affect the 1000-seed weight much, 6 days of waterlogging did the opposite with the lower values at both vegetative (10%) and maturity (11%) stages.

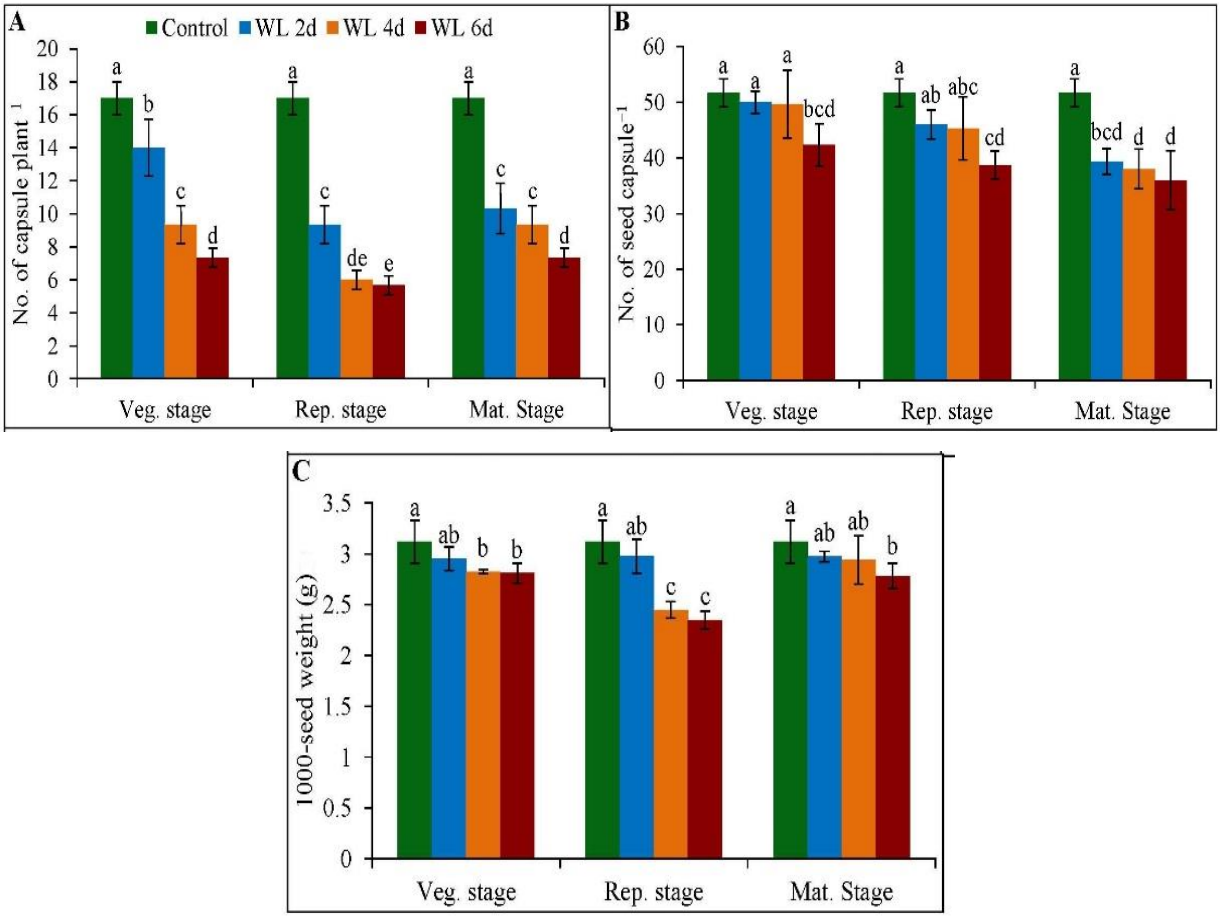

Fig. 3. (A) Number of capsule plant^{-1}, (B) number of seed capsule^{-1}, and (C) 1000-seed weight of sesame affected by different durations of waterlogging at different growth stages. Mean (±SD) was calculated from three replicates for each treatment. Values in a column with different letters are significantly different at $p \leq 0.05$ applying LSD test

The highest grain yield plant^{-1} was observed in the control plant, which was greatly reduced by waterlogging treatments irrespective of growth stages. On the contrary, the lowest value (71% lower) of grain yield plant^{-1} was recorded in plants waterlogged for 6 days at the reproductive stage. Two days of waterlogging exposure decreased grain yield plant^{-1} by 31, 54 and 49%, four days of waterlogging by 45, 67 and 55%; and six days of waterlogging by 59, 71 and 68% at vegetative, reproductive, and maturity stages, respectively (Fig. 4A).

Stover yield plant^{-1} also decreased significantly under waterlogging stress compared to well-drained control plants. The lowest value of stover yield was recorded in plants waterlogged for 6 days, with 47, 24, and 37% lower values at vegetative, reproductive, and maturity stages, respectively (Fig. 4B).

Biological yield means the total grain yield and stover yield plant^{-1}, significantly lessened due to waterlogging stress. The longest waterlogging duration (6 days) resulted in 49, 33, and 43% lower biological yield plant^{-1} at vegetative, reproductive and maturity stages, respectively (Fig. 4C).

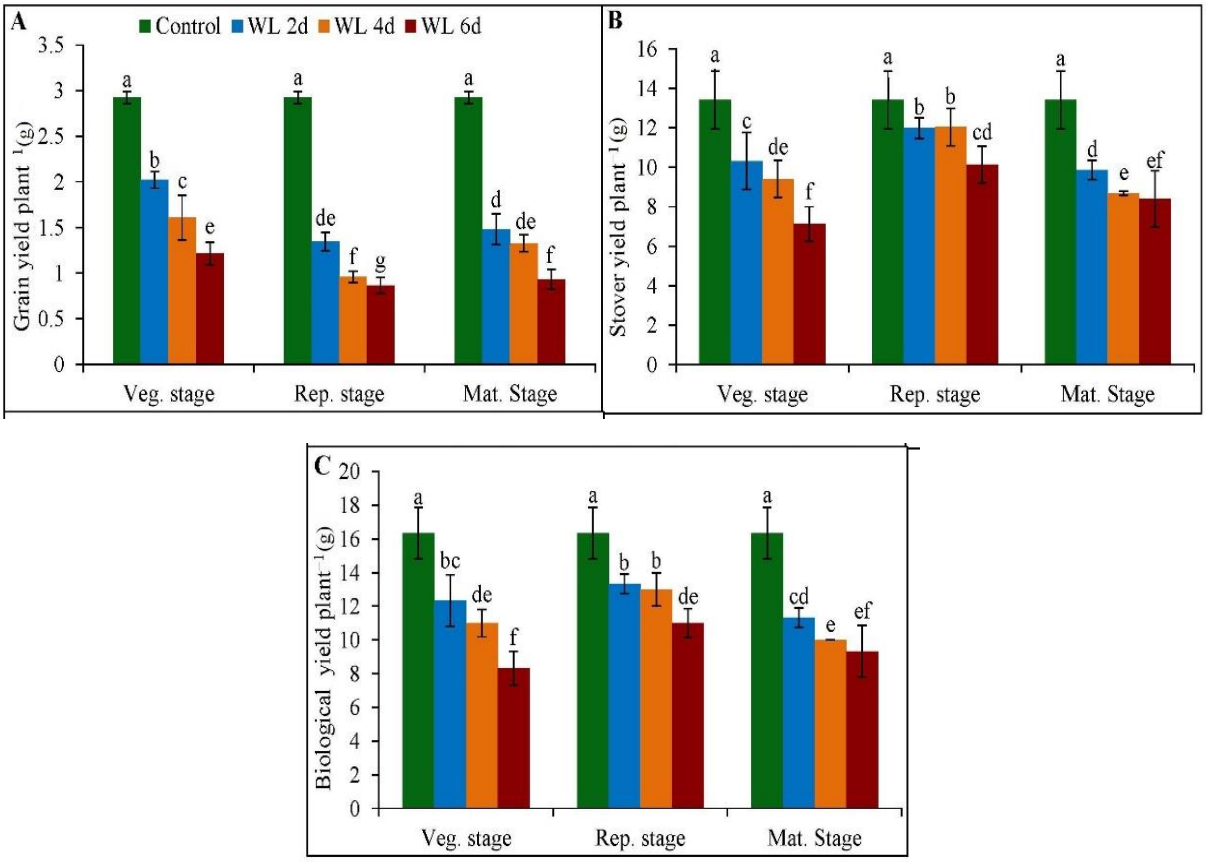

Fig. 4. (A) Grain yield, (B) stover yield, and (C) biological yield of sesame affected by different durations of waterlogging. Mean (±SD) was calculated from three replicates for each treatment. Values in a column with different letters are significantly different at $p \leq 0.05$ applying LSD test.

Waterlogging stress can result in a wide array of morphological and physiological alterations leading to yield reduction of sesame (Wei et al., 2013; Saha et al., 2016; Linh et al., 2021). Moreover, available literature on sesame grown under environmental adversities has forecasted significant yield losses, which may threaten global food security. Therefore, a detailed understanding of sesame responses to abiotic stresses like waterlogging is required. A growth stage-dependent study will facilitate the growers to assume the more critical stage of sesame to keep protected from excess water exposure. So, the study was conducted with the latest variety of sesame available and exposed to waterlogging for 2, 4, and 6 days at vegetative, reproductive, and maturity stages.

Plant exposure to waterlogging stress causes a major impact on morphology which is evident from the changes in plant height, above-ground FW, DW, number of leaves plant^{-1} and leaf area plant^{-1}. According to the morphological parameters measured in this experiment, the reproductive stage showed the most susceptibility, and then maturity and vegetative stages, respectively if compared to their respective controls. Such sensitivity of reproductive stages to waterlogging was previously reported in cotton (Wang et al., 2017) and sesame (Linh et al., 2021). Excess water reduces oxygen availability to plant cells, and negative impacts on leaves reduce photosynthesis, so plant growth is hampered. Reduction in plant height of sesame plants under waterlogging or flooding stress was also reported by several other researchers (Mensah et al., 2006; Wei et al., 2013; Saha et al., 2016). Longer durations of waterlogging are prone to wilting, and reduced FW is obtained, and subsequently reduced DW also. Our findings revealed that at vegetative and maturity stages, only 6 and 8 days of waterlogging could reduce the FW and DW of sesame plants, whereas in the case of the reproductive stage, only 2 days of waterlogging significantly reduced sesame FW and DW. Such findings were also reported in cowpea (Olorunwa et al., 2022), barley (Zhang et al., 2007), and sesame (Mensah et al., 2006; Linh et al., 2021). Waterlogging-induced leaf senescence is a major reason for a reduction in leaf parameters. The number of leaves plant^{-1} decreased due to waterlogging stress in cowpea (Olorunwa et al., 2022), soybean (Hasanuzzaman et al., 2022; Sathi et al., 2022) and sesame (Linh et al., 2021). Waterlogging-induced reduction of leaf area was also previously reported in barley (Zhang et al., 2007), mung bean (Kumar et al. 2013), cotton (Wang et al., 2017), cowpea (Olorunwa et al., 2022), soybean (Hasanuzzaman et al., 2022; Sathi et al., 2022) and sesame (Mensah et al., 2006; Saha et al., 2016). Such decline in leaf area can result from photosynthesis reduction due to stomatal closure in waterlogged condition. Other possible reasons are leaf damage, senescence, inhibited leaf formation and expansion, etc. (Olorunwa et al., 2022).

The waterlogging causes denitrification and rapid volatilization, which reduces the available soil nitrogen (N), leading to the lower content of leaf N, limited N-fixation and nodulation (Bacanamwo and Purcell, 1999; Rasaei et al., 2012). Hence, leaf yellowing or chlorosis can result in reduced photosynthetic pigments. The present study documented a duration-dependent declination of SPAD values irrespective of the growth stages (Fig. 2C). However, compared to their respective control reduction, chl was the highest during the reproductive stage which might be due to the greater sensitivity of this stage to excess water. Excess water-induced reduction of leas chl was also documented in several other studies with different crops (Yin et al., 2010; Wang et al., 2017; Hasanuzzaman et al., 2022; Olorunwa et al., 2022; Sathi et al., 2022) including sesame (Wei et al., 2013; Anee et al., 2019; Linh et al., 2021)

Yield is a result of the integration of metabolic reactions in plants. Any factor that influences this metabolic activity at any period of plant growth can affect the yield. Waterlogging stress has shown mostly negative effects on yield attributes (number of capsule plant^{-1}, number of seed capsule^{-1}, grain yield plant^{-1}, stover yield plant^{-1} and biological yield) of

sesame plants at different stages and durations. With the increasing duration of waterlogging, the damage effects got higher and at the reproductive stage, it was the most prominent. In some other experiments with sesame plants, a reduction in the number of capsule formation was also evident (Mensah et al., 2006; Saha et al., 2016). The number of seed capsule^{-1} was significantly reduced in sesame plants exposed to waterlogging for 3 days at 29 days after seedling emergence (Saha et al., 2016). Thousand-seed weight was not much affected by a shorter duration of stress, but the longest duration (6 days) of waterlogging reduced all yield attributes. Saha et al. (2016) observed that 3 days of waterlogging stress could not alter the weight of thousand seeds in three sesame genotypes which is also evident in our result for 2 days; even for 4 days when stress was imposed at the maturity stage (Fig. 3C). However, other crops like cotton (Wang et al., 2017), and maize (Ren et al., 2014) have also been studied to have decreased 1000-seed weight under waterlogging stress. Such negative effects of waterlogging stress on the yield of sesame were also demonstrated in earlier studies (Saha et al. 2016).

Conclusion

Sesame is well-known not only for its food values but also for its wide range of adaptability. A crop with multidimensional use and cultivation potential should gain more attention, and waterlogging is one of the major constraints to that task. Our experiment shows that sesame plants exhibit a duration-dependent impairment of their morpho-physiology and yield attributes. Such study of sesame varieties under waterlogging will provide researchers with some important information regarding the response or adaptation mechanisms which will open a new avenue in the way of tolerant variety development. In addition, as the present study demonstrated, the reproductive stage is the most susceptible stage of sesame to waterlogging exposure; growers can use proper agronomic practices to protect the crop during that particular period.

Acknowledgments

This work was conducted with the financial support of the Ministry of Science and Technology and the HEQEP project of the University Grants Commission of Bangladesh.

Author Contributions

T.I.A., with the help of M.H. designed the experiment. T.I.A. performed the experiment, with the active participation of P.K.B. and M.H. M.H. did the statistical analysis. T.I.A. has written the manuscript. All the authors critically reviewed, edited and approved the final manuscript.

References

Addinsoft. XLSTAT. v. 2015: Data analysis and statistics software for Microsoft Excel. 2016. Addinsoft, Paris.

Anee TI, Nahar K, Rahman A, Mahmud JA, Bhuiyan TF, Alam MU, Fujita M and Hasanuzzaman M. Oxidative damage and antioxidant defense in S*esamum indicum* after different waterlogging durations. *Plants* 2019; 8(7): 196.

Bacanamwo M and Purcell LC. Soybean dry matter and N accumulation responses to flooding stress, N sources and hypoxia. *J. Exp. Bot*. 1999; 50(334): 689-696.

Food and Agriculture Organization of the United Nations. FAOSTAT Database. Rome, Italy. 2021; Available at: http://faostat.fao.org/ (accessed on 5 December, 2021)

Gibbs J and Greenway H. Mechanisms of anoxia tolerance in plants. II. Energy requirements for maintenance and energy distribution to essential processes. *Funct. Plant Biol*. 2003; 30: 1-47.

Hasanuzzaman M, Ahmed N, Saha T, Rahman M, Rahman K, Alam MM, Rohman MM and Nahar K. Exogenous salicylic acid and kinetin modulate reactive oxygen species metabolism and glyoxalase system to confer waterlogging stress tolerance in soybean (*Glycine max* L.). *Plant Stress* 2022; 3: 100057.

Hasanuzzaman M, Mahmud JA, Nahar K, Anee TI, Inafuku M, Oku H and Fujita M. Responses, adaptation, and ROS metabolism in plants exposed to waterlogging stress. In: Reactive oxygen species and antioxidant systems in plants: Role and regulation under abiotic stress, Khan MIR and Khan NA, eds., Springer, Singapore. 2017; p. 267-281.

Jia W, Ma M, Chen J and Wu S. Plant morphological, physiological and anatomical adaption to flooding stress and the underlying molecular mechanisms. *Int. J. Mol. Sci*. 2021; 22(3): 1088.

Jung H-J, Roy SK, Cho S-W, Kwon S-J, Kun C, Chun H-C and Woo S-H. Proteome analysis of sesame leaves in response to waterlogging stress at vegetative and flowering stages. *Biol. Plant*. 2019; 63: 733-749.

Kumar P, Pal M, Joshi R and Sairam RK. Yield, growth and physiological responses of mung bean [*Vigna radiata* (L.) Wilczek] genotypes to waterlogging at vegetative stage. *Physiol. Mol. Biol. Plants* 2013; 19: 209-220.

Linh MN, Thuc LV, Sakagami J-I, Orgill S, Van TH, Khuong NQ and Nhan PP. Effects of waterlogging on the growth of different varieties of sesame (*Sesamum indicum* L.). *Int. J. Plant Res*. 2021; 11(1): 1-6.

Mensah JK, Obadoni BO, Eruotor PG and Onome-Irieguna F. Simulated flooding and drought effects on germination, growth, and yield parameters of sesame (*Sesamum indicum* L.). *Afr. J. Biotech*. 2006; 5(13): 1249-1253.

Myint D, Gilani SA, Kawase M and Watanabe KN. Sustainable sesame (*Sesamum indicum* L.) production through improved technology: An overview of production, challenges, and opportunities in Myanmar. *Sustainability* 2020; 12: 3515.

Olorunwa OJ, Adhikari B, Shi A and Barickman TC. Screening of cowpea (*Vigna unguiculata* L. Walp.) genotypes for waterlogging tolerance using morpho-physiological traits at early growth stage. *Plant Sci*. 2022; 315: 111136.

Pan J, Sharif R, Xu X and Chen X. Mechanisms of waterlogging tolerance in plants: Research progress and prospects. *Front. Plant Sci*. 2021; 11: 627331.

Ploschuk RA, Miralles DJ, Colmer TD, Ploschuk EL and Striker GG. Waterlogging of winter crops at early and late stages: Impacts on leaf physiology, growth and yield. *Front. Plant Sci*. 2018; 9: 1863.

Rasaei A, Ghobadi ME, Jalali-Honarmand S, Ghobadi M and Saeidi M. Waterlogging and its effects on nitrogen of soil and plant. *Ann. Biol. Res*. 2012; 3: 119-124.

Ren B, Zhang J, Li X, Fan X, Dong S, Liu P and Zhao B. Effects of waterlogging on the yield and growth of summer maize under field conditions. *Can. J. Plant Sci*. 2014; 94: 23-31.

Saha RR, Ahmed F, Mokarroma N, Rohman MM and Golder PC. Physiological and biochemical changes in waterlogging tolerant sesame genotypes. *SAARC J. Agric*. 2016; 14(2): 31–45.

Sathi KS, Masud AAC, Falguni MR, Ahmed N, Rahman K and Hasanuzzaman M. Screening of soybean genotypes for waterlogging stress tolerance and understanding the physiological mechanisms. *Adv. Agric*. 2022; 5544665.

Wang X, Deng Z, Zhang W, Meng Z, Chang X and Lv M. Effect of waterlogging duration at different growth stages on the growth, yield and quality of cotton. *PLoS ONE* 2017; 12: e0169029.

Wei W, Li D, Wang L, Ding X, Zhang Y, Gao Y and Zhang X. Morpho-anatomical and physiological responses to waterlogging of sesame (*Sesamum indicum* L.). *Plant Sci*. 2013; 208: 102-111.

Yin D, Chen S, Chen F, Guan Z and Fang W. Morpho-anatomical and physiological responses of two *Dendranthema* species to waterlogging. *Environ. Exp. Bot*. 2010; 68: 122-130.

Zhang G, Tanakamaru K, Abe J and Morita S. Influence of waterlogging on some anti-oxidative enzymatic activities of two barley genotypes differing in anoxia tolerance. *Acta Physiol. Plant* 2007; 29: 171-176.

J. Bangladesh Acad. Sci. 46(2); 175-183: December 2022 DOI: 10.3329/jbas.v46i2.63416

Journal of Bangladesh Academy of Sciences

Journal homepage: http://www.bas.org.bd/publications/jbas.html

Research Article

Estimation of prolonged lifetimes of excited states of neutral oxygen atom (OI) by time-resolved laser-induced breakdown spectroscopy (TR-LIBS)

Abul Fazal Mohammed Yusuf Haider[1,3], Nabil Md Rakinul Hoque[2], Arifur Rahaman and Zulfiqar Hasan Khan[*]

Department of Physics, University of Dhaka, Dhaka, Bangladesh

RTICLE INFO

Article History

Received: 28 November 2022
Revised: 13 December 2022
Accepted: 15 December 2022

Keywords: Words: LIBS, Upper state, Lifetime, Self-absorption, Radiation trapping

ABSTRACT

Lifetimes of the upper states of excited oxygen atoms corresponding to transitions to the common lower state in the case of the emission lines around 777 nm and 844 nm have been estimated by measuring the line intensities as a function of the delay time between the Q-switching of the laser and the opening of the window of the ICCD. In the case of the emission line around 777 nm, resulting from the transitions from the three very closely spaced upper energy levels, $2s^2\ 2p^3\ (^4S^0)\ 3p\ ^5\mathbf{P_3}$ (777.194 nm), $2s^2\ 2p^3\ (^4S^0)\ 3p\ ^5\mathbf{P_2}$ (777.417 nm) and $2s^2\ 2p^3\ (^4S^0)\ 3p\ ^5\mathbf{P_1}$ (777.539 nm) to the common lower energy level $2s^2\ 2p^3\ (^4S^0)\ 3s\ ^5\mathbf{S_2}$, the lifetime was measured to be 253 ns. Similarly, in the case of the emission-line around 844 nm, resulting from the transitions from the three very closely spaced upper energy levels $2s^2\ 2p^3\ (^4S^0)\ 3p\ ^3\mathbf{P_0}$ (844.625 nm), $2s^2\ 2p^3\ (^4S^0)\ 3p\ ^3\mathbf{P_2}$ (844.636 nm) and $2s^2\ 2p^3\ (^4S^0)\ 3p\ ^3\mathbf{P}_1$ (844.676 nm) to the common lower energy level $2p^3\ (^4S^0)\ 3s\ ^3\mathbf{S_1}$, the lifetime was measured to be 278 ns by this technique. The measured lifetimes in our experiment, for both 777 nm and 844 nm atomic transition lines of oxygen (O), are almost nine times higher than the theoretical value. Self-absorption and radiation trapping are possible mechanisms responsible for the mismatch between measured and intrinsic lifetimes. Last but not least, utilizing the TR-LIBS technique is yet another incredible application to estimate the prolonged lifetime of closely spaced excited states of an atom in the presence of self-absorption and radiation trapping. The average plasma cooling temperature (excitation temperature) lifetime was found to be 1183 ns, which is compatible with the previously reported values.

Introduction

Laser-Induced Breakdown Spectroscopy (LIBS) is a convenient, competent, and fast elemental analysis technique. LIBS can be employed for plasma diagnostics (Haider and Khan, 2012; Hahn and Omenetto, 2010), such as measuring plasma's electron density and temperature by the Saha-Boltzmann plot (Shaikh et al., 2006; Quintero et al. 1997; Aguilera and Aragón 2007). Another novel application of LIBS is the measurement of lifetimes of atomic and ionic states (Haider et al. 2014).

The lifetime of upper states must be taken into account when studying light propagation in atomic line filters (Molisch and Oehry 1998), discharge lamps (Rajaraman and Kushner 2004; Camparo and MacKay 2007), trapped cold atoms (Hillenbrand et al., 1995; Balik et al., 2009), stellar media (Boldyrev and Gwinn 2003), or Laser media (Zhang et al., 2017). In optical applications like scintillators, amplifiers, and display systems, the lifetime is a crucial spectroscopic parameter (Stoita et al., 2010). Lifetime measurements are needed in areas such as astrophysical abundance determinations and plasma diagnostics (Curtis 1976). Lifetimes of different atomic/ionic transitions were estimated using time-resolved laser-induced fluorescence (TR-LIF) (Xu et al., 2004; Mayo et al.,

[*]Corresponding author: <zulfiqarshuvo@du.ac.,bd>

[2]*Biomedical Engineering Department, Washington University, St Louis, USA*

[3]*Department of Mathematics and Natural Sciences, BRAC University, Dhaka, Bangladesh*

2005; Mayo et al., 2006), LIF (Hannaford and Lowe 1983; O'Brian and Lawler 1992), and beam-foil (Pinnington et al., 1988; Berry et al., 1971) technique, high-frequency deflection method (O'Brian and Lawler 1992), and delayed coincidence methods (Smith et al., 1975; King and Adams 1974). The comparison of various techniques demonstrates that no single procedure can be employed to calculate lifetimes for all types of states in atoms, ions, and molecules over a wide spectral region and lifetime. For example, the beam-foil technique of measuring lifetimes is only restricted to the atoms, whereas the high-frequency deflection method can measure the lifetime of ions. In contrast, time-resolved LIBS (TR-LIBS) can be employed for lifetime measurement for different transitions regardless of wavelength and atomic/ionic/molecular states.

In our previous work, LIBS coupled with time-resolved gated ICCD was employed to measure the lifetimes of some excited states of the Nitrogen atom (Haider et al., 2014). In this paper, we extend the same technique to measure the lifetime of excited states of the oxygen atom. The estimated lifetime is 253 ns and 278 ns for the emission lines around wavelengths of 777 nm and 844 nm, respectively, which is about nine times higher than the corresponding theoretical value. This augmented lifetime of oxygen atoms is likely linked with (i) self-absorption of oxygen atoms as the upper states involved are very close together in energy and (ii) radiation trapping.

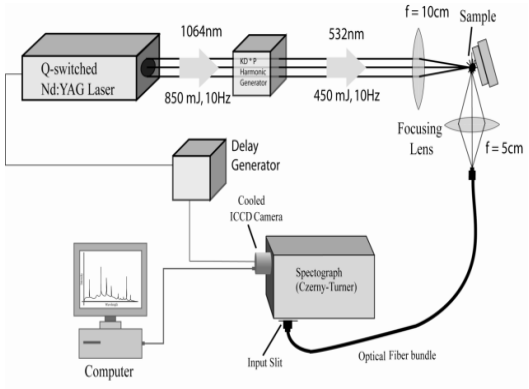

Fig. 1. Schematic diagram of TR-LIBS to find the lifetime of excited states.

Experimental setup

For performing the LIBS experiment, a Q-switched Nd: YAG laser of model Spectra-Physics LAB-170-10 (Figure 1) was focused having the following parameters: wavelength of 532 nm with a pulse duration of 8 ns; and a repetition rate of 10 Hz with a maximum pulse energy of 450 mJ. Additionally, it contained harmonic generators that used KDP crystals to produce the fundamental up to the fourth harmonic. The actual energy of the pulse employed was 40 mJ. Having divergence, Θ<0.5 mrad, the beam maintains a Gaussian shape in the far-field (Haider and Khan, 2012).

The output at 532 nm, i.e., the second harmonic of laser, was used and focused onto the air of the laboratory at room temperature using a convex lens of about 10 cm focal length. Therefore, intense, brief, and weakly ionized plasma is produced, and the resulting emitted radiation is focused by a fused quartz lens (aperture 50 mm) onto multimode silica fiber (length 3 m). The electric field intensity at the focus of the laser beam (about 200 microns in diameter) is sufficient to accelerate the electrons produced by primary ionization. In turn, they produce secondary and tertiary ionization. Thus, a weakly ionized plasma is created via laser ablation where the percentage of electrons is <10% of other species present in the plasma. (Haider et al., 2014).

The optical fiber's output was attached to the slit present at the entrance of a spectrograph in the Czerny-Turner configuration with a 75 cm focal length (Acton Model SP-2758). To provide high- and low-resolution spectra in the wavelength range of 190-880 nm, the spectrograph is fitted with three interchangeable gratings with three different groves (2400, 600, and 300 grooves/mm). A spectrum with a width of about 38 nm and 9 nm can be recorded using a grating with 600 grooves and 2400 grooves per millimeter that are blazed at 500 nm and 240 nm, respectively.

The spectrograph was connected to an intensified CCD (ICCD) camera (Princeton PI-MAX), where a programmable delay generator makes the gating of the spectrograph feasible. The 1024 x 1024 pixel ICCD camera was cooled using Peltier cooling to -20 C to lower noise. The Nd: YAG laser pulse electrically activated the ICCD camera after a programmable time delay. In the current investigations, to measure emission line intensities at different delay times (200 ns-6500 ns), a gate width (t_w) of 50 μs was used. To improve the signal-to-noise ratio, average spectra are recorded from about 40 laser pulses. For each delay time t, three of these averages were used to calculate the line intensity. The manufacturer's software (Win Spec/32) was utilized to operate the Acton spectrograph and gated ICCD camera (Haider and Khan 2012).

Theory

Suppose the number of the excited atom at time t = 0 is N_1^0. Then the number of the excited atoms at time t is

$$N_1(t) = N_1^0 e^{-t/\tau} \quad (1)$$

where τ is the lifetime of spontaneous emission.

For a particular transition, the area under the emission spectrum (I) is proportional to the photon numbers emitted in the interval between t and ∞.

$$I \propto \int_t^\infty N_1(t)\, dt$$

$$\text{or, } I = \mathrm{C} \int_t^\infty N_1(t)\, dt$$

$$\text{or, } I = CN_1^0 \int_t^\infty e^{-t/\tau}\, dt \text{ ; [Using equation (1)]}$$

$$= CN_1^0\, \tau\, e^{-t/\tau}$$

$$= \mathrm{K} e^{-t/\tau}$$

$$\text{or, } \ln \mathrm{I} = \ln \mathrm{K} - \frac{t}{\tau} \quad (2)$$

where C and K both are the proportionality constants and are related as $\mathrm{K} = \mathrm{C}\, \mathrm{N}_1^0\, \tau$

Now, if one introduces a time delay t between the excitation (by laser-plasma) of the upper atomic state and the opening of the detection system (e.g., ICCD) and varies the time delay t and plot logarithm of the integrated intensity (I) as a function of this time delay t, should get a semi-logarithmic plot to estimate the lifetime of the excited state of an atom/ion corresponding to the transition to a lower state.

Again let us consider two energy levels, E_1 and E_0 (E_1 for the upper level and E_0 for the lower level). N_1 and N_0 are population densities of upper and lower levels. The Boltzmann equation gives ratios of level populations as a function of temperature,

$$\frac{N_1}{N_0} = e^{-(E_1 - E_0)/k_B T}$$

$$\text{or, } \frac{N_1}{N_0} = e^{-\Delta E/k_B T} \quad (3)$$

where k_B is the Boltzmann constant and T is the plasma temperature.

Under the local thermodynamic equilibrium (LTE) condition, and considering the plasma to be optically thin and homogeneous, the total intensity of a spectral line from an excited atom or ion is

$$\mathrm{I}\, \alpha\, \mathrm{N}_1$$

$$\text{or, } \mathrm{I} = \mathrm{Q}\mathrm{N}_1 \quad (4)$$

where Q is the proportionality constant. Now from equation (3), we can write,

$$\mathrm{I} = \frac{\mathrm{N}_0 \mathrm{Q}}{e^{\Delta E/k_B T}} \quad (5)$$

From the above equation, it can be seen that when the plasma temperature T decreases, the corresponding intensity of the emission line decreases.

Therefore, in TR- LIBS, the intensity of an emission line will reduce for two reasons, namely (1) the spontaneous decay of the excited state and (2) the cooling of the plasma.

Discussion

Lifetimes of the atomic excited states can be estimated employing time-resolved LIBS, first

reported by Haider et al. (Haider et al. 2014), where they estimated the lifetime of the neutral nitrogen atom. In this technique, the delay between the Q-switched laser pulse and the gating of the intensified CCD (ICCD) window is precisely regulated by employing a delay generator with a suitable program. Finally, the lifetimes of excited states of atomic/ionic species could be evaluated from the plot of Intensity vs. delay (Haider et al. 2014). This same approach for lifetime measurement has been incorporated to observe prolonged plasma lifetime associated with both multidimensional-plasma-grating-induced break-down spectroscopy (MIBS) (Hu et al. 2022) and plasma-grating-induced breakdown spectroscopy (GIBS) (Hu et al. 2020) compared to that of filament-induced breakdown spectroscopy (FIBS). Likewise, employing the same technique, (Yang et al. 2019) estimated the lifetime of the Si I, Ti I, Al I, and Fe I atoms in soil samples, ranging from 1.0 to 2.0 μs. Our paper, investigates the lifetime of the excited state of the neutral oxygen atom (OI) by employing well-established time-resolved LIBS. Fig. 2(a)-(c) shows how the Intensity of spectral lines of Neutral Oxygen Atom (OI) decreases as the delay increases. Fig. 3(a) represents the plot of Intensity vs. Delay time (in the range of 175 ns-6500ns) of the OI line around 777nm. The bi-exponential fit is better matched than the mono-exponential fit (Fig. 3(b)) for the data set because the bi-exponential fit (Fig. 3(c)) has a lower chi-square value (3.8108 vs. 5.5108) and a higher regression coefficient (0.9688 vs. 0.9557). A semi-logarithmic plot confirmed that the data set is indeed bi-exponential for the OI line around 777 nm (Fig 3(d)), from where exponential decay constants can be determined. However, the contribution of the slower decay process has to be deducted from the contribution of the quicker decay process to obtain the accurate value of the decay constant from the semi-log plot of InI vs. Delay. Therefore, the piecewise straight-line obtained for the relatively slow decay process was extrapolated in the 175ns-700ns delay period (Fig. 3d).

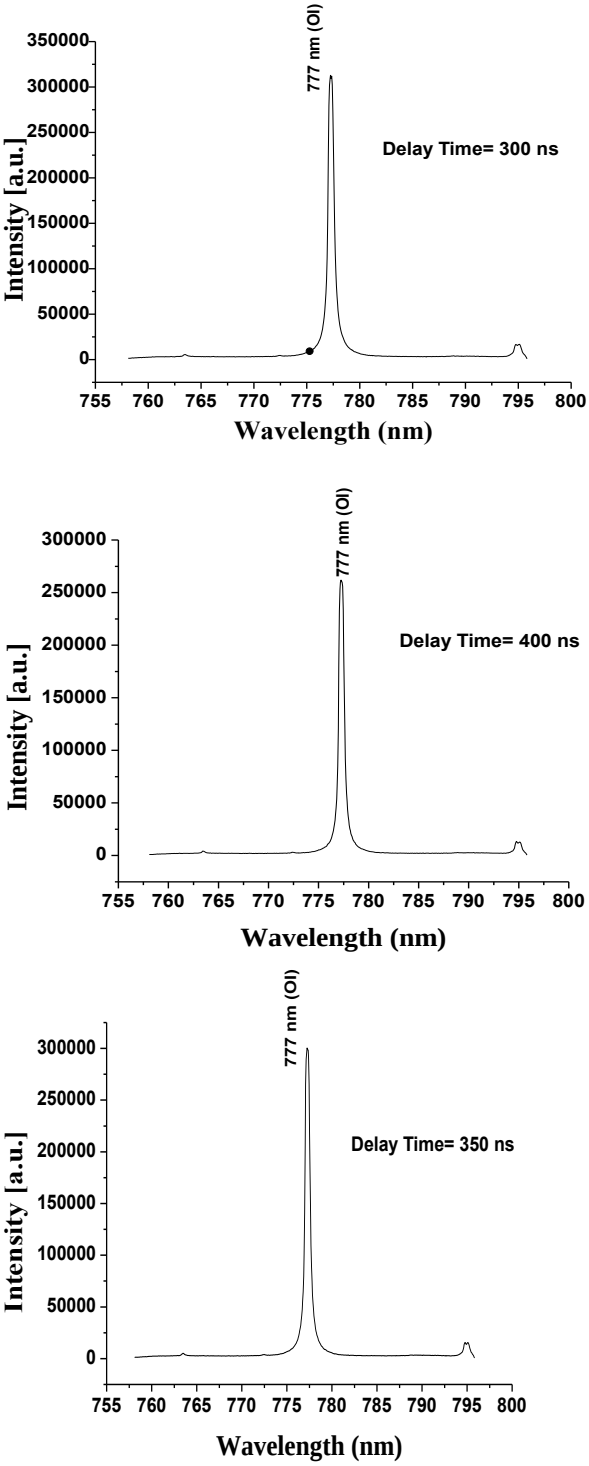

Fig. 2(a)-(c): Spectral emission lines of the neutral oxygen atom (OI) around 777 nm used for the determination of the lifetimes of the upper state at three different delay times t of (a) 300 ns, (b) 350 ns, (c) 400 ns.

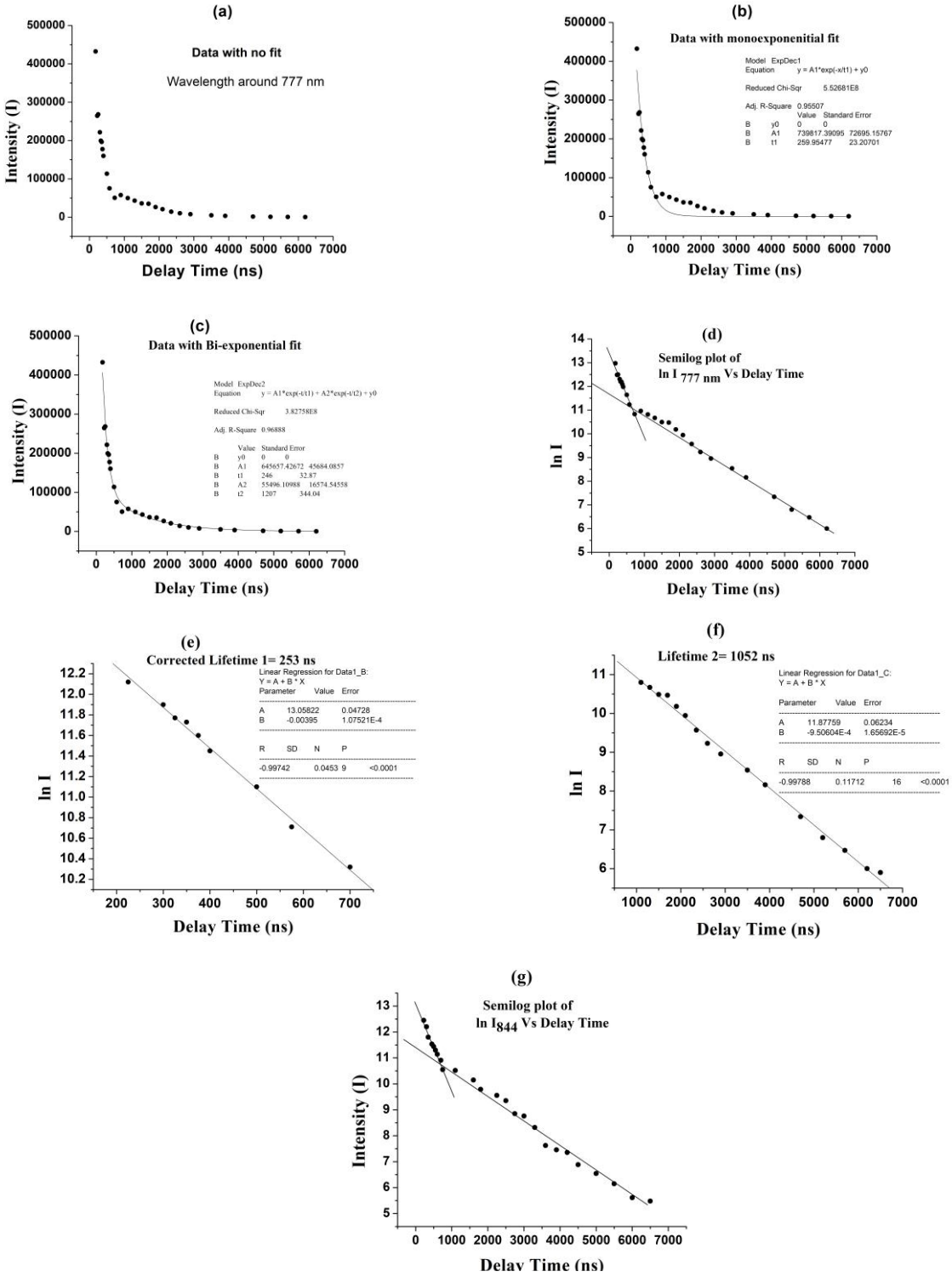

Fig. 3. Plot of the integrated intensity vs. delay time (in the range of 175-7000 ns) of the emission line of OI (at 777 nm) with (a) no fit, (b) mono-exponential fit ((R^2=0.95507)), and (c) bi-exponential (R^2=0.9688). Semi-logarithmic plots (i.e. ln I vs. delay time) of the OI emission line (at 777 nm) with linear fits in the range of (d) 175-6500 ns, (e) 175-700 ns (corrected), and (f) 900-6500 ns. (g) Semi logarithmic plot (ln I vs delay time) with linear fits in the range 175-6500 ns of the emission line around 844 nm.

The quicker decay process contains the contribution coming from the slower decay process, which is removed by subtraction. After this correction, the resulting semi-log plot for the delay range of 175-700 ns is obtained in Fig. 3(e), which has been drawn for OI atomic emission line at 777 nm. For this linear semi-log plot after the correction, the composite lifetime of three very closely spaced upper energy levels, $2s^2\ 2p^3\ (^4S^0)\ 3p\ ^5\mathbf{P_3}$ (777.194 nm), $2s^2\ 2p^3\ (^4S^0)\ 3p\ ^5\mathbf{P_2}$ (777.417nm) and $2s^2\ 2p^3\ (^4S^0)\ 3p\ ^5\mathbf{P_1}$ (777.539 nm), resulting to the transition to the $2s^2\ 2p^3\ (^4S^0)\ 3s\ ^5\mathbf{S_2}$ lower state (Fig. 4), were obtained as 253 ns. The results from the corrected semi-logarithmic plot (253 ns) match well with those obtained by the bi-exponential plot (241ns) (Table 1).

Table 1. Upper state lifetimes estimated for different transitions of OI around the wavelengths of 777 nm and 844 nm

Observed Lines (nm)	Transitions		By semi logarithmic fit			By bi-exponential fit	
	Upper state (Term value with J)	Lower state (Term value with J)	Spontaneous emission Lifetime (ns)		Plasma cooling temperature (excitation temperature) decay time (ns)	Spontaneous emission lifetime (ns)	Plasma cooling temperature (excitation temperature) decay time (ns)
			Uncorrected Value	Corrected Value			
777 (around)	$2s^2\ 2p^3\ (^4S^0)\ 3p\ ^5\mathbf{P_3}$ (777.194 nm) $2s^2\ 2p^3\ (^4S^0)\ 3p\ ^5\mathbf{P_2}$ (777.417 nm) $2s^2\ 2p^3\ (^4S^0)\ 3p\ ^5\mathbf{P_1}$ (777.539)	$2s^2\ 2p^3(^4S^0)\ 3s\ ^5\mathbf{S_2}$	263	253	1052	241	1207
844 (around)	$2s^2\ 2p^3\ (^4S^0)\ 3p\ ^3\mathbf{P_0}$ (844.625 nm) $2s^2\ 2p^3\ (^4S^0)\ 3p\ ^3\mathbf{P_2}$ (844.636 nm) $2S_2\ 2P_3\ (^4S^0)\ 3p\ ^3\mathbf{P_1}$ (844.676 nm)	$2s^2\ 2p^3(^4S^0)\ 3s\ ^3\mathbf{S_1}$	296	278	1136	271	1159

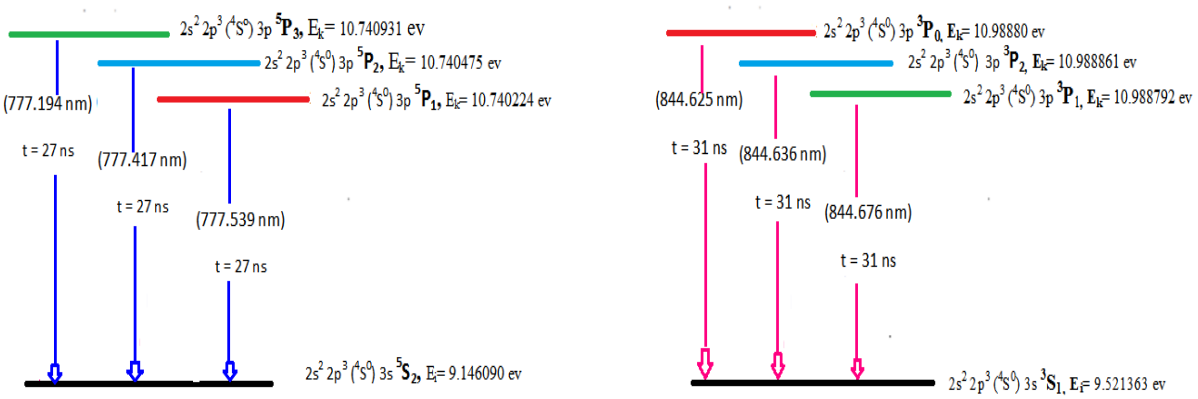

Fig. 4. Schematic diagram (drawn not to scale) of three upper states and associated lower state with relevant lifetimes.

The measured lifetimes in our experiment are much higher than the theoretical values of the lifetime for each transition between the energy levels in the case of 777 nm, which is 27 ns (Sansonetti and Martin 2005). This discrepancy might be linked primarily to the self-absorption between the energy levels where photons spontaneously emitted from the excited higher level of one atom can be absorbed by another atom of the same element in the lower state. In our previous work for determining the lifetime of the upper state of Nitrogen (Haider et al. 2014), three different transitions have three different lifetimes (67 ns, 104 ns, 198 ns), whereas, in this work, three lifetimes are very close (~27 ns). Unlike Nitrogen (Haider et al. 2014), emission lines result from the transitions from the three very closely spaced upper levels to the common lower level. As the emission lines are too close to be spectroscopically resolved, there should be considerable self-absorption for the proximity in energies of the three upper levels for the emission lines around 777 nm. The photon emitted from excited oxygen atoms/ions eventually decays to the ground state, emitting a photon and, after that, can be re-absorbed by another oxygen atom/ion with comparable energy spacing. The absorption-emission cycle can occur at very high rates (~few hundred MHz at room temperature) in a plasma plume temperature lifetime of the hot plasma. The magnitude of the decay constants for plasma cooling (excitation temperature) was measured as 1207 ns for wavelengths around 777 nm. For the OI line at 844 nm, the semi-logarithmic graphs (lnI vs. delay time) in Fig. 3(g) indicate the presence of two decay processes with characteristic slopes in two delay regions. The faster decay in the 175 ns to 800 ns interval of delay represents the lifetime of the higher state. In the case of around 844 nm line, for three upper levels $2s^2\ 2p^3\ (^4S^0)\ 3p\ ^3P_0$ [844.625 nm], $2s^2\ 2p^3\ (^4S^0)\ 3p\ ^3P_2$ (844.636nm) and $2s^2\ 2p^3\ (^4S^0)\ 3p\ ^3P_1$ (844.676 nm), the self-absorbed and radiation trapped lifetime (of the composite upper states) corresponding to the transition to $2s^2\ 2p^3\ (^4S^0)\ 3s\ \mathbf{^3S_1}$ common lower level (Fig. 4) was measured as 278 ns by the same procedure. The measured lifetime is much higher than the theoretical values of the lifetime (31 ns) (Sansonetti and Martin 2005). However, the magnitude of the decay constants for the plasma cooling was measured as 1159 ns for wavelengths around 844 nm, and the average decay constant for plasma cooling (1183 ns) matches well with the previously reported value (Cremers and Radziemski 1989).

Conclusions

In this study, we employed the well-known time-resolved LIBS (TR-LIBS) technique to simultaneously examine the lifetimes of the excited states of the neutral oxygen atom (OI) and the decay time of the laser-induced plasma temperature. The upper states of OI atom's lifetimes were measured by observing the atomic emission intensities as a function of the time interval between the laser's Q-switching and the ICCD's gate opening. The self-absorbed and radiation-trapped decay lifetimes of the excited OI atom for emission lines around the wavelengths of 777 nm and 844 nm are 253 ns and 278 ns, respectively, according to the outcomes from the corrected semi-logarithmic fit of the experimental data.

The measured lifetimes are much higher than the theoretical values (Sansonetti and Martin 2005) because of the self-absorption and radiation-trapping effect between the energy levels. Instead of departing the medium, a photon released spontaneously by one atom can be absorbed by another atom of the same element, resulting in the photon being trapped before it can escape and be detected. As a result, the self-absorption and the radiation trapping mechanism effectively 'delay' the photon's emission, resulting in an apparently much longer lifespan than the natural one.

The amount of time that elapses between the beginning of the laser plasma and the triggering of the laser pulse is significantly influenced by the energy of the laser pulse. Rather than the actual initiation time of the laser-induced plasma, the synchronous Q-switched laser pulse was responsible for the opening of the window of ICCD. Therefore,

shot-to-shot stability is crucial to ensure measurement accuracy, whereas error will be introduced if the laser pulse energy is not constant. Finally, within the limitations stated above, the method can be employed to measure the lifetimes of upper states (actual, self-absorbed, or radiation trapped) corresponding to different transitions of atoms and ions almost in any matrix. The technique works well for atomic emission lines in areas of the spectrum having a weak background originating from the plasma.

Conflicts of Interest

With regard to the publication of this paper, the authors have no conflicts of interest.

Acknowledgement

The experimental work was carried out in the Nonlinear Optics and Laser Spectroscopy Laboratory of the Center for Advanced Research in Sciences (CARS) of the University of Dhaka.

References

Aguilera J. and Aragón C. Multi-element Saha–Boltzmann and Boltzmann plots in laser-induced plasmas. *Spectrochimica Acta Part B: Atom. Spectro.* 2007; 62 (4): 378-385.

Balik S, Havey M, Sokolov I and Kupriyanov D. Optical pumping dynamics and near-resonance light scattering in an ultracold sample of R 87 b atoms. *Physical Review A* 2009; 79(3): 033418.

Berry H, Desesquelles J and Dufay M. Lifetime measurements of autoionizing levels by the beam-foil technique. *Physics Letters* 1971; *A* 36(3): 237-238.

Boldyrev S and Gwinn CR. Lévy model for interstellar scintillations. *Physical review letters* 2003; 91(13): 131101.

Camparo JC and MacKay R. Spectral mode changes in an alkali rf discharge. *J. Appl. Phys.* 2007; 101(5): 053303.

Cremers DA and Radziemski LJ. *Laser-induced plasmas and applications*: United States: Marcel Dekker Inc.1989.

Curtis LJ. Lifetime measurements. *Beam-Foil Spectroscopy* 1976; 63-109.

Hahn DW and Omenetto N. Laser-induced breakdown spectroscopy (LIBS), part I: review of basic diagnostics and plasma–particle interactions: still-challenging issues within the analytical plasma community. *Applied spectroscopy* 2010; 64(12): 335A-366A.

Haider AFMY and Khan Z. Determination of Ca content of coral skeleton by analyte additive method using the LIBS technique. *Optics & Laser Technology* 2012; 44(6): 1654-1659.

Haider AFMY, Ira MK, Khan Z and Abedin K. Radiative lifetime measurement of excited neutral nitrogen atoms by time resolved laser-induced breakdown spectroscopy. *J. Anal. Ato. Spectrom.* 2014; 29(8): 1385-1392.

Hannaford P and Lowe R. Determination of atomic lifetimes using laser-induced fluorescence from sputtered metal vapor. *Optical Engineering* 1983; 22(5): 532-544.

Hillenbrand G, Burnett K and Foot C. Effect of scattered radiation on sub-Doppler cooling. *Physical Review A* 1995; 52(6): 4763.

Hu M, Peng J, Niu S and Zeng H. Plasma-grating-induced breakdown spectroscopy. *Advanced Photonics* 2020; 2(6): 065001.

Hu M, Shi S, Yan M, Wu E and Zeng H. Femtosecond laser-induced breakdown spectroscopy by multidimensional plasma grating. *J. Anal. Ato. Spectrom.* 2022; 37(4): 841-848.

King G and Adams A. An accurate determination of the lifetime of the 63P state in mercury using a new electron-photon delayed coincidence apparatus. *J. Phys. B: Atom. Mol. Phys.* 1974; (1968-1987) 7(13): 1712.

Mayo R, Campos J, Ortiz M, Xu H, Svanberg S, Malcheva G and Blagoev K. Radiative lifetimes of Zr III excited levels. *The European Physical Journal D-Atomic, Molecular, Optical and Plasma Physics* 2006; 40(2): 169-173.

Mayo R, Ortiz M and Campos J. Experimental transition probabilities for lines arising from the 4d5p and 4d5d configurations of ZrIII. *J. Quant. Spectrosc. Radiat. Transf.* 2005; 94(1): 109-116.

Molisch AF and Oehry BP. *Radiation trapping in atomic vapours*: Oxford University Press 1998.

O'Brian T and Lawler J. Radiative lifetimes in BI using ultraviolet and vacuum-ultraviolet laser-induced fluorescence. *Astron. Astrophys.* 1992; 255: 420-426.

O'Brian T and Lawler J. Excited Level Lifetime Measurements. *Experimental Methods in the Physical Sciences*. United States: Academic Press, 1996; 217-254.

Pinnington E, Ansbacher W, Kernahan J, Ahmad T and Ge Z.-Q. Lifetime measurements for low-lying levels in Hg I and Hg II using the beam-foil technique. *Cana. J. Phys.* 1988; 66(11): 960-962.

Quintero M, Rodero A, Garcia M and Sola A. Determination of the excitation temperature in a nonthermodynamic-equilibrium high-pressure helium microwave plasma torch. *Appl. Spectrosc.* 1997; 51(6): 778-784.

Rajaraman K and Kushner MJ. A Monte Carlo simulation of radiation trapping in electrodeless gas discharge lamps. *J. Phys. D: Appli. Phys.* 2004; 37(13): 1780.

Sansonetti JE and Martin WC. *Handbook of Basic Atomic Spectroscopic Data*: American Institute of Physics 2005.

Shaikh NM, Rashid B, Hafeez S, Jamil Y and Baig M. Measurement of electron density and temperature of a laser-induced zinc plasma. *J. Phys. D: Appl. Phys.* 2006; 39(7): 1384.

Smith A, Read F and Imhof R. Measurement of the lifetimes of ionic excited states using the inelastic electron-photon delayed coincidence technique. *J. Phys. B: Atom. Mol. Phys.* 1975; (1968-1987) 8(17): 2869.

Stoita A, Vautey T, Jacquier B and S Guy. Impact of the radiation trapping on lifetime measurement of Er3+ doped glasses. *Journal of Lumin.* 2010; 130(7): 1119-1123.

Xu H, Persson A, Svanberg S, Blagoev K, Malcheva, G, Pentchev V, Biémont E, Campos J, Ortiz M and Mayo R. Radiative lifetime and transition probabilities in Cd I and Cd II. *Physical Review* 2004; *A* 70(4): 042508.

Yang Y, Zhigao L, Deshuo M and Mingjun M. Spectral characteristic of laser-induced plasma in soil. *Plasma Sci. Techno.* 2019; 22(1): 015502.

Zhang Q, Shang Q, Shi J, Chen J, Wang R, Mi Y, Du W, Shen C, Ma R and Qiu X. Wavelength tunable plasmonic lasers based on intrinsic self-absorption of gain material. *ACS Photonics* 2017; 4(11): 2789-2796.

J. Bangladesh Acad. Sci. 46(2); 185-191: December 2022 DOI:10.3329/jbas.v46i2.63417

Journal of Bangladesh Academy of Sciences

Journal homepage: http://www.bas.org.bd/publications/jbas.html

Research Article

Etiologies and antibiotic resistance patterns of acute bloodstream infections by gram-negative bacterial isolates in a tertiary care hospital, Sirajganj, Bangladesh

Mohammad Zakerin Abedin*, Md. Muhaymenul Islam, Md. Babul Aktar, Muhammad Irfanul Islam, Nowshin Tarannum, Laila Jarin[1], Zohora Fatema-Tuz[2] and Ahmed Abdullah Akhtar

Department of Microbiology, School of Biomedical Sciences, Khwaja Yunus Ali University, Sirajganj, Bangladesh

ARTICLE INFO

Article History

Received:1 December 2022
Revised: 19 December 2022
Accepted:20 December 2022

Keywords: Antibiotic resistant, Bloodstream infection, Gram-negative bacterial isolates

ABSTRACT

Bloodstream infections (BSI) are serious, life-threatening, and critical clinical conditions with high global human morbidity and mortality rates. This study aimed to determine the Gram-negative bacterial profiles and antimicrobial resistance patterns of acute bloodstream infections in rural patients. Three hundred forty-six blood samples were collected and analyzed with the BD Bactec™ FX40 automated culture system, selective media culture, and biochemical parameters. Finally, antimicrobial susceptibility testing was performed using the disk diffusion method. The most common age group affected out of 51 cases was 41-60 years, with 20 patients (39.22%), and 1-15 years, with 2 patients (3.92%). Male patients were more susceptible (66.67%) than female patients. Among the isolates, *E. coli* was the most common, with 23 cases (45.1%); Cephradine was the most resistant antibiotic, and Imipenem was the most sensitive. Multiple drug-resistant pathogens were one of the most notable findings in our work. Our study will surely provide the best guide for properly treating antibacterial-resistant bacterial diseases and minimizing their critical mortality and morbidity.

Introduction

Life-threatening bloodstream infections were linked to higher rates of mortality and morbidity, as well as higher medical expenses. (Blomberg et al., 2007). Blood culture is a vital tool for detecting common bacterial isolates that cause BSI and remains the gold standard for bacteremia detection (Vasudeva et al., 2016). The most well-known Gram-negative bacteria isolated from blood cultures are *E. coli, K. pneumoniae, P. aeruginosa,* and *S. paratyphi A* (Zakerin et al., 2021).

Since the early 1950s, there has been a striking expansion in the frequency of bacteremia brought about by members of Enterobacteriaceae and other Gram-negative bacilli (Arora and Devi, 2007). *E. coli,* which was reported to be shared in the past (Vasudeva et at., 2016; Arora and Devi, 2007), has been replaced by other bacteria that resist multiple drugs (Chaturvedi et al., 1989). Infections brought about by Gram-negative bacteria are the most challenging issue for healthcare professionals because of antibiotic resistance.

A crucial technique for active antibiotic resistance surveillance is examining clinical specimens for antibiotic susceptibility (Vernet et al., 2014). Bacterial antimicrobial susceptibility profiles typically differ between populations due to geographical differences, nearby antimicrobial prescribing, and the prevalence of resistant bacterial stains in a given area. Other than these, the accessibility of much less potent products, the utilization of antibiotics for veterinary products, a lack of standardized diagnostic facilities, and the expanded practice of antibiotic self-medication are

*Corresponding author: <zakerin.du2016@gmail.com>

[1]*Department of Microbiology, Chittagong University, Chottogram, Bangladesh*
[2]*Bioinformatics and Environmental Sciences, Science and Math Program, Asian University for Women, Chottogram, Bangladesh*

straightforwardly related to improving antibiotic resistance (Manyi-Loh et al., 2018). Antibiotic resistance is spreading and becoming increasingly widespread globally (Aslam et al., 2020). Antimicrobial therapy is typically started empirically prior to the availability of the results of a blood culture (Ko and Hsueh, 2009). This research was done to identify the Gram-negative bacterial profiles of bacteremia and to evaluate the isolated pathogens' antibiotic resistance profiles. This study's main objective was to support clinicians in starting experimental antimicrobial therapy and creating effective antibiotic strategies.

Materials and Methods

Type of research

A cross-sectional investigation was carried out in a laboratory setting from January to June 2021. The study was approved by the ethical grant committee at Khwaja Yunus Ali University. At KYAMCH, 346 blood samples were collected from patients with fever, indoors or outdoors.

Blood sampling and laboratory investigation

All the samples were taken aseptically for culture in the automated blood culture system. Approximately 1-5 ml of blood collected from 1-12-year-old children were inoculated adequately into the BD Bactec™ FX40 Peds Plus/F culture vial. Adults received an 8-10 ml blood sample inoculated into the BD Bactec™ FX40 Aerobic/F culture vial. According to the manufacturer's guidelines, these vials were inserted quickly into the BD Bactec™ FX40 System at 35±2°C for 5-7 days (Abedin et al., 2020a).

Unloading positive and negative vials

A red and green light on the outside of the drawer indicated that positive and negative vials were waiting for removal. These positive vials were taken for further analysis, and negative vials were considered culture-negative.

Bacteriological culture

A drop of blood from a positive culture vial was placed onto blood agar and MacConkey agar culture plates and then incubated at 37^0C for 24 hours. Bacterial growth on the MacConkey agar plates indicated Gram-negative bacteria. Blood agar cultures were only used to determine whether or not bacteria were Gram-negative.

Identification of bacteria using biochemical assays

Gram-negative bacterial isolates were identified using biochemical indicators. These indicators included alkaline reactions, acidic reactions, hydrogen sulfide (H_2S) production, gas production, motility tests, indole production, and urea hydrolysis. Anti-sera were used only for *Salmonella* identification and gram staining techniques were performed to differentiate between Gram-positive and Gram-negative bacteria (Abedin et al., 2020a).

In-vitro antibiotic sensitivity test

According to CLSI recommendations, all bacterial isolates underwent antimicrobial susceptibility testing using the Kirby-Bauer disc diffusion method on Mueller Hinton agar (MHA) (CSLI, 2019). The antibiotic discs (6 mm, HiMedia, India) were placed in different positions on the plate. Finally, the plates were closed and incubated at 37°C for 24 hours. The zone sizes were interpreted as per the CLSI guidelines. Amoxicillin (10 µg), cefoxitin (30 µg), ceftriaxone (30 µg), chloramphenicol (30 µg), ciprofloxacin (5 µg), gentamicin (10 µg), levofloxacin (5 µg), cephradine (30 µg), imipenem (10 µg), and imipenem (10 µg) were the antibiotics utilized in the test. A control strain of *Salmonella typhi* (ATCC 14028) was used for all culture and antibiotic susceptibility tests throughout the investigation (Abedin et al., 2020b).

Data Analysis

Using Excel 2016 and SPSS version 20, the data was examined. To verify the statistical analysis, descriptive statistics and chi-square tests were used. The significant p-value was determined to be <0.5.

Results and Discussion

The present study was conducted with 346 outdoor and indoor patients who were suffering from bloodstream infections during the period. There were 51 (14.7%) blood culture-positive cases with Gram-negative bacilli among them, and the remaining 295 (85.3%) were reported as negative results. When the prevalence of isolated Gram-negative bacteria was compared between genders, it was found that Gram-negative bacteria were significantly higher in males (34/51) (66.7%) than in females (17/51) (33.3%). Bloodstream infections are standard worldwide, and Gram-negative bacteria predominantly cause them. The distribution and frequency of BSIs caused by Gram-negative bacteria vary according to age and gender. It is critical to evaluate resistant Gram-negative bacteria using a standardized, simple, and reproducible in vitro assay to determine antimicrobial drug activity against isolated strains. Only a few studies have been done in Bangladesh regarding the prevalence of BSIs caused by Gram-negative bacteria and the antibacterial susceptibility of BSI-causing Gram-negative bacteria.

Among 346 total isolates, 51 were tested by BD Bactec™ FX 40 and found 14.7% positive for Gram-negative bacteria. The negative results of the automated system were 85.3% due to the presence of Gram-positive bacteria and the contamination of isolates with non-pathogenic microbes (Fig. 1).

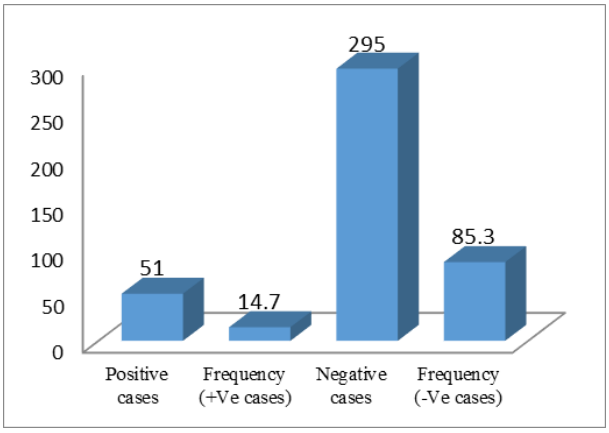

Fig. 1. Number of positive and negative cases of Gram-negative BSIs patient

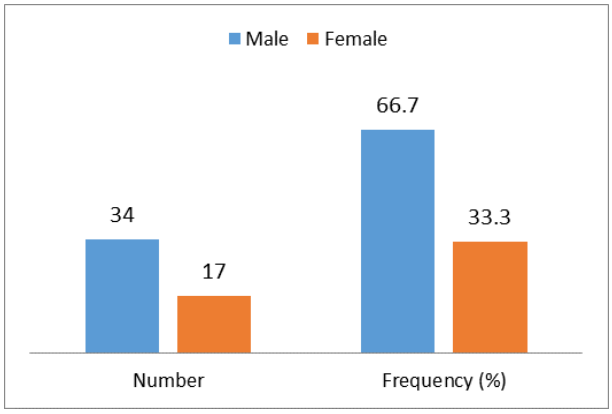

Fig. 2. Prevalence of Gram-negative BSIs patients on gender distribution

Table 1. Age distribution of Gram-negative BSIs patient

Age Range (Years)	Frequency (%)
0-15	2(3.9)
16-25	5(9.8)
26-40	9(17.7)
41-60	20(39.2)
61-Above	15(29.4)

Table 2. Distribution pattern of isolated Gram-negative bacterial species of bloodstream infection (n=51)

Gram-negative bacterial isolates	Total number	Percentage (%)
E. coli	23	45.1
K. pneumoniae	03	5.9
P. aeruginosa	03	5.9
S. typhi	16	31.4
Achromobacter spp.	02	3.9
B. cepacian complex	04	7.8
Total	51	100%

Out of 51 cases, the most common age group affected was 41–60 years with 20 cases (39.2%), followed by 61 and above years with 15 cases (29.4%), 26–40 years with 9 cases (17.7%), and 16–25 years with 5 cases (9.8%), respectively. Besides

these, children aged 1–15 years with 2 cases (3.9%) were the least affected group (Table 1), and males 34/51 (66.7%) were more commonly attended than females 17/51 (33.3%) (Fig.2). This finding is nearly correlated with a previous study showing that being elderly and male are risk factors for acquiring BSI (Uslan et al., 2007; Khan et al., 2019).

In this study, out of 51 Gram-negative isolates, *E. coli* was the most common, with 23 cases (45.1%), and *Salmonella typhi* had 16 cases (31.34%). *K. pneumoniae, P. aeruginosa, Achromobacter spp., and Burkholderia cepacian* complex were also found with 3 cases (5.9%), 3 cases (5.9%), 2 cases (3.9%), and 4 cases (7.8%), respectively (Table2). These results contradict those of a recent report on resistance trends in BSI from China (surveillance study 1998–2017), which identified *E. coli* as the most common BSI-causing pathogen (Musicha et al.,2017) and a study conducted in Australia (Tian et al., 2019). However, a previous study in China's Hubei Province identified gram-negative bacteria, such as *E. coli* and *K. pneumoniae,* as common BSI-causing pathogens. Reports from Malawi in Africa (Uslan et al., 2007) revealed *S. typhi* and *K. pneumoniae* as BSI-causing pathogens, whereas *P. aeruginosa* was more common in Iran (Kreidl et al., 2019). Similarly, Japan has shown a varying pathogenic profile of BSIs, with Gram-negative bacteria, including *E. coli* and *Klebsiella spp.*, as the most common organisms (Keihanian et al., 2018). These varying accounts of BSI-causing pathogens account for regional variances. Our findings closely matched those of a Saudi Arabian investigation that found *E. coli* and *K. pneumoniae* to be the most prevalent generic Enterobacteriaceae isolates (Hattori et al., 2018).

In the current investigation, 51 isolates were evaluated against regularly used antibiotics using the disk diffusion method. Out of 26 isolates of *E. coli* (Table 3), it was observed that Cephradine, Cefuroxime, and Amoxicillin were resistant with 95.7%, 82.6%, and 73.9%, respectively. Other antibiotics showed more than 50% resistance, namely Amoxiclav (69.6%), Ampicillin (60.9%), Azithromycin (56.5%), Gentamicin (60.9%), and Cefixime (60.9%). This study nearly correlated with another in which *E. coli* displayed the highest resistance patterns (Tian et al., 2019).

In the case of *Salmonella typhi,* Cefixime was resistant at 62.5%, followed by Ampicillin (56.3%) and Cephradine (56.3%) (Table 3). The rest of the drug-resistant patterns were higher than 50%, which is correlated with Abedin et al. (2020a).

Levofloxacin, Ceftazidime, and Imipenem were completely sensitive in all three cases of *Pseudomonas spp.* Aside from that, cephradine was utterly resistant. In *Achromobacter* spp., there was 100% resistance to Ampicillin, Azithromycin, Cefixime, Cefuroxime, Cephradine, Ceftazidime, and Gentamicin. In the case of *Klebsiella pneumoniae,* all commonly used antibiotics are 66.7% resistant, namely Ampicillin, Cefuroxime, Cephradine, Ciprofloxacin, and Gentamicin. In the *B. cepacia* complex, Ceftazidime was most sensitive at 75%, while Cefixime, Azithromycin, and Ampicillin were resistant at 100%. Imipenam was the most effective in this study against Gram-negative bacteria that caused BSIs. This study nearly correlated with another study where indicated that significant levels of resistance were reported against Ampicillin, Amoxicillin, Ceftriaxone, and co-Trimoxazole with a pooled resistance range of 52.8-85.7% in Gram-negative isolates (Tianet al., 2019). The current study found that 84.3% and 54.9% of Ampicillin and Amoxicillin were resistant to gram-negative bacteria.

The disk diffusion method is the most simple, reliable, and economical way to perform simultaneous experiments on many organisms. It can be used in clinical laboratories for routine antibacterial susceptibility testing of Gram-negative bacteria isolated from BSI patients.

Table 3. Antimicrobial sensitivity profile of *E. coli* and *Salmonella typhi*

Antibiotics	*E. coli* (23)		*Salmonella typhi*(16)	
	R (%)	S (%)	R (%)	S (%)
Amikacin	7(30.4)	16(69.6)	8 (50.0)	8 (50.0)
Amoxicillin	17(73.9)	6(26.1)	8 (50.0)	8 (50.0)
Amoxiclav	16(69.6)	7(30.4)	8 (50.0)	8 (50.0)
Ampicillin	14(60.9)	9(39.1)	9 (56.3)	7 (43.8)
Azithromycin	13(56.5)	10(43.5)	6 (37.5)	10 (62.5)
Cefixime	14(60.9)	9(39.1)	10 (62.5)	6 (37.5)
Cefuroxime	19(82.6)	4(17.4)	6 (37.5)	10 (62.5)
Cephradine	22(95.7)	1(4.3)	9 (56.3)	7 (43.8)
Ceftazidime	9(39.1)	14(60.9)	6 (37.5)	10 (62.5)
Ciprofloxacin	7(30.4)	16(69.6)	2 (12.5)	14 (87.5)
Gentamicin	14(60.9)	9(39.1)	8 (50.0)	8 (50.0)
Imipenam	2(8.7)	21(91.3)	2 (12.5)	14 (87.5)
Levofloxacin	6(26.1)	17(73.9)	3 (18.8)	13 (81.2)
Meropenem	1(4.3)	22(95.7)	2 (12.5)	14 (87.5)

Note: R=Resistant, S=Sensitive, %= Percentage

Table 4. Antimicrobial sensitivity profiles of other Gram negative isolates

Antibiotics	*B.cepacia complex (4)*		*K. pneumonia (3)*		*Achromobacter spp.(2)*		*Pseudomonas spp. (3)*	
	R (%)	S (%)	R (%)	S (%)	R (%)	S (%)	R (%)	S (%)
Amikacin	3 (75.0)	1 (25.0)	1 (33.3)	2 (66.7)	1 (50.0)	1 (50.0)	2 (66.7)	1 (33.3)
Amoxicillin	2 (50.0)	2 (50.0)	1 (33.3)	2 (66.7)	0	2 (100)	1 (33.3)	2 (66.7)
Amoxiclav	2 (50.0)	2 (50.0)	0	2 (66.7)	0	2 (100)	1 (33.3)	2 (66.7)
Ampicillin	4 (100)	0 (0.0)	2 (66.7)	1 (33.3)	2 (100)	0	2 (66.7)	1 (33.3)
Azithromycin	3 (75.0)	1 (25.0)	0	3 (100)	2 (100)	0	2 (66.7)	1 (33.3)
Cefixime	4 (100)	0	0	3 (100)	2 (100)	0 (0.0)	1 (33.3)	2 (66.7)
Cefuroxime	3 (75.0)	1 (25.0)	2 (66.7)	1 (33.3)	2 (100)	0	2 (66.7)	1 (33.3)
Cephradine	3 (75.0)	1 (25.0)	2 (66.7)	1 (33.3)	2 (100)	0	3 (100)	0 (0.0)
Ceftazidime	1 (25.0)	3 (75.0)	1 (33.3)	2 (66.7)	2 (100)	0	0 (0.0)	3 (100)
Ciprofloxacin	3 (75.0)	1 (25.0)	2 (66.7)	1 (33.3)	0	2 (100)	1 (33.3)	2 (66.7)
Gentamicin	3 (75.0)	1 (25.0)	2 (66.7)	1 (33.3)	2 (100)	0	2 (66.7)	1 (33.3)
Imipenam	2 (50.0)	2 (50.0)	0	3 (100)	0	2 (100)	1 (33.3)	2 (66.7)
Levofloxacin	2 (50.0)	2 (50.0)	0	3 (100)	1 (50.0)	1 (50.0)	0	3 (100)
Meropenem	2 (50.0)	2 (50.0)	0	3 (100)	0	2 (100)	0	3 (100)

Note: R=Resistant, and S=Sensitive

Conclusion

E.coli and *Salmonella typhi* were the most common Gram-negative bacteria isolated from bloodstream infections. Bloodstream infection was predominant among male patients, and the 41–60 age groups were the riskiest. According to a descriptive study of our research, men and older people should be more cautious about bacterial bloodstream infections. During our study, Imipenem and Imipenem were the most effective antibacterial drugs against all isolates except for *Burkholderia cepacia* complex (ceftazidime). Except for *Achromobacter spp.* (cefixime), most bacteria, including *E. coli* (cephradine) and *Salmonella typhi* (cefixime) were Clindamycin-resistant. A multidrug-resistant pathogen was found in our research, which is one of the most remarkable points. We believe that combining imipenem with other drugs can effectively control multidrug-resistant bloodstream infections caused by the subject pathogens. Bacterial infection has emerged daily in developing countries because of the lack of awareness, inappropriate lifestyle, and improper hygiene of the masses. In addition, antibioticresistance is also increasing the problem to a great extent. Our research identified the most potent and prevalent infectious bacterial agents in different age groups and also assessed the responsiveness of currently used antibiotics. This will help physicians to choose appropriate medicinal therapy and guide scientists to screen for multidrug-resistant pathogens.

Acknowledgments

The authors thank the employees at Khwaja Yunus Ali University and KYAMCH's Department of Microbiology for their assistance in the laboratory.

Conflict of Interests

All authors agreed before submitting the article, and there were no conflicts of interest.

Funding

No particular grants from public, private, or nonprofit funding organizations were given to this study.

References

Abedin MZ, Ahmed AA, Hossain MS andAktar MB. Laboratory based diagnosis of bacteraemia among inpatients and outpatients with acute febrile illness at Khwaja Yunus Ali Medical College and Hospital in Bangladesh. *Eur. J. Med. Health Sci.*2020a; 2(3):46-51.

Abedin MZ, Jarin L, Rahman MA and Islam R. Culture positivism exploitation through automated fluorescent-sensor technology from patients with blood stream infections. *J. Adv.Biotechnol. Exp.Ther.*2020b; 3(3):165-170.

Arora U and Devi P. Bacterial profile of blood stream infections and antibiotic resistance pattern of isolates. *JK Science* 2007; 9(4):186-190.

Aslam A, Gajdács M, Zin CS, Ab Rahman NS, Ahmed SI, Zafar MZ and Jamshed S. Evidence of the practice of self-medication with antibiotics among the lay public in low-and middle-income countries: a scoping review. *Antibiotics* 2020; 9(9):597.

Blomberg B, Manji KP, Urassa WK, Tamim BS, Mwakagile DS, Jureen R, Msangi V, Tellevik MG, Holberg-Petersen M, Harthug S and Maselle SY. Antimicrobial resistance predicts death in Tanzanian children with bloodstream infections: a prospective cohort study. *BMC infectious diseases*. 2007; 7(1):1-4.

Chaturvedi P, Agrawal M and Narang P. Analysis of blood-culture isolates from neonates of a rural hospital. *Indian pediatrics*. 1989; 26(5):460-465.

Hattori H, Maeda M, Nagatomo Y, Takuma T, Niki Y, Naito Y, Sasaki T andIshino K. Epidemiology and risk factors for mortality in bloodstream infections: A single-center retrospective study in Japan. *Am. J. Infect. Control*2018; 46(12):e75-79.

Keihanian F, Saeidinia A, Abbasi K andKeihanian F. Epidemiology of antibiotic resistance of blood culture in educational hospitals in Rasht, North of Iran. *Infect. Drug Resist.*2018; 11:1723-1728.

Khan MA, Mohamed AM, Faiz A and Ahmad J. Enterobacterial infection in Saudi Arabia: First record of *Klebsiella pneumoniae*with triple carbapenemase genes resistance. *J. Infect. Dev. Ctries.* 2019; 13(04):334-341.

Ko WC and Hsueh PR. Increasing extended-spectrum β-lactamase production and quinolone resistance among Gram-negative bacilli causing intra-abdominal infections in the Asia/Pacific region: data from the Smart Study 2002–2006. *J. Infect.* 2009; 59(2):95-103.

Kreidl P, Kirchner T, Fille M, Heller I, Lass-Flörl C and Orth-Höller D. Antibiotic resistance of blood cultures in regional and tertiary hospital settings of Tyrol, Austria (2006-2015): Impacts & trends. *Plos one*. 2019; 14(10):e0223467.

Manyi-Loh C, Mamphweli S, Meyer E and Okoh A. Antibiotic use in agriculture and its consequential resistance in environmental sources: potential public health implications. *Molecules*. 2018;23(4):795.

Musicha P, Cornick JE, Bar-Zeev N, French N, Masesa C, Denis B, Kennedy N, Mallewa J, Gordon MA, Msefula CL and Heyderman RS. Trends in antimicrobial resistance in bloodstream infection isolates at a large urban hospital in Malawi (1998–2016): a surveillance study. *The Lancet infectious diseases*. 2017; 17(10):1042-1052.

Tian L, Zhang Z and Sun Z. Antimicrobial resistance trends in bloodstream infections at a large teaching hospital in China: a 20-year surveillance study (1998-2017). *Antimicrob. Resist. Infect. Control* 2019;8(1):1-8.

Uslan DZ, Crane SJ, Steckelberg JM, Cockerill FR, Sauver JL, Wilson WR andBaddour LM. Age- and sex-associated trends in bloodstream infection: a population-based study in Olmsted County, Minnesota. *Arch. Intern. med*. 2007; 167(8):834-839.

Vasudeva N, Nirwan PS and Shrivastava P. Bloodstream infections and antimicrobial sensitivity patterns in a tertiary care hospital of India. *Ther. Adv. Infect. Dis*. 2016; 3(5):119-127.

Vernet G, Mary C, Altmann DM, Doumbo O, Morpeth S, Bhutta ZA andKlugman KP. Surveillance for antimicrobial drug resistance in under-resourced countries. *Emerging Infect. Dis.*2014; 20(3):434-441.

Zakerin A, Zaman MS, Ahmed F, Yeasmin F, Aktar MB, Shilpi RY and Ahmed AA. Bacteriological profile and antimicrobial susceptibility patterns of symptomatic bloodstream infection in Dhaka City. *Biosight*. 2021; 2(1):13-17.

J. Bangladesh Acad. Sci. 46(2); 193-202: December 2022 DOI:10.3329/jbas.v46i2.63046

Journal of Bangladesh Academy of Sciences

Journal homepage: http://www.bas.org.bd/publications/jbas.html

Research Article

Total variation denoising and Euclidean distance based distributed temperature monitoring in Brillouin optical time-domain analysis sensors

Taskin Sakin, Tanbin Ahmed and Abul Kalam Azad*

Department of Electrical and Electronic Engineering, University of Dhaka, Bangladesh

ARTICLE INFO

Article History

Received:1 December 2022
Revised: 18 December 2022
Accepted: 20 December 2022

Keywords: Distributed fiber optic sensors, Total variation denoising, Euclidean distance, Least-squares fitting, Pattern recognition.

ABSTRACT

The performance of Brillouin optical time domain analysis (BOTDA) sensors is largely deteriorated due to the poor signal-to-noise ratio (SNR) of Brillouin gain spectra (BGSs) collected from the BOTDA experiment. The fast monitoring of distributed temperature using BOTDA sensors is also vital for many long-distant applications. To cope with these requirements, this paper proposes total variation denoising (TVD) and Euclidean distance-based pattern recognition (TEPR) for high-performance BOTDA sensors. The performances of TEPR are analyzed explicitly, and rigorous comparisons have been made with traditional nonlinear least squares fitting (NLSF). The experimentally demonstrated results signify that the proposed TEPR can improve the measurement uncertainty by up to ~55% compared to NLSF without worsening the experimental spatial resolution. The signal processing for using TEPR is also ~4 times faster than that for using NLSF. Hence, the proposed technique is an efficient and reliable alternative for the fast and accurate monitoring of distributed temperature in BOTDA sensors.

Introduction

In recent decades, stimulated Brillouin scattering (SBS) based BOTDA sensors have exhibited enormous capabilities in the distributed monitoring of temperature and strain (Motil et al, 2016; Azad et al., 2017; Ba et al., 2016). Such sensors offer high accuracy, good spatial resolution and long-distant monitoring even in hazardous environments (Azad et al., 2017; Wang et al., 2020). For the distributed monitoring of temperature, BOTDA sensors exploit an amplified probe wave which becomes amplified as a result of interaction with the oppositely-directed pump wave through a single piece of optical fiber cable (OFC). The gain in this amplification process is recorded as local Brillouin gain spectrum (BGS) along the OFC. The difference in pump-probe frequency (f_d) for which peak gain is attained in a local BGS is termed in literature as the local Brillouin frequency shift (BFS) (Motil et al, 2016; Zhao et al., 2022). The BFS of a local BGS alters linearly with the surrounding temperature of OFC. In the BOTDA experiment, the local BGSs along the OFC are assembled with BOTDA traces collected by varying f_d step-by-step within a suitable frequency range. In temperature monitoring applications, BFSs of the local BGSs are first determined, which are then mapped to temperature according to the linear BFS-temperature relationship (Azad et al., 2017). To determine such BFSs, NLSF is a widely-used technique (Azad et al., 2017; Haneef et al., 2018).

A single BOTDA trace collected from the conventional BOTDA sensor at a particular f_d is very noisy. The SNR of BGSs formed with such noisy traces is thus very low. The performance of

*Corresponding author: <azad@du.ac.bd>

BOTDA sensors also deteriorates for such low SNR. The SNR of BGSs along OFC can effectively be improved to an acceptable level by adopting a trace-averaging approach. Such an approach requires the gathering a large number of traces (e.g., several thousand) at a particular f_d, which are then averaged to attain one averaged trace at that f_d to be used for constructing BGSs. This averaging approach is time-intensive and thus lengthens the collection of BGSs, especially for long OFC if the number of traces (T_N) averaged is quite large.

For the fast collection of BGSs with improved SNR, several alternative schemes have been combined with conventional BOTDA sensors. The studies (Jia et al., 2010; Angulo-Vinuesa et al., 2012) combined Raman amplification with BOTDA sensors to enhance the sensing performance. Alternatively, the realizations of long-distant sensing using pulse coding techniques have been reported in Ref. (Iribas et al., 2017; Mariñelarena et al., 2018). The combination of Raman amplification and pulse coding technique has also been reported to attain high-performance sensing with improved accuracy and resolution (Soto et al., 2012). However, the combination of such additional schemes to conventional BOTDA sensors makes the BOTDA setup complex and costly due to the use of additional hardware components.

Other than employing the complex, costly and modified BOTDA setup, a viable alternative is to collect much noisy BGSs along the OFC, adopting a small number of trace averaging (i.e., smaller T_N) with conventional BOTDA setup and then using an effective and time-efficient denoising algorithm for denoising such noisy BGSs. To explore this, several signal denoising techniques, such as wavelet transform (Soto et al., 2016; Azad, 2020), Wiener filter (Azad, 2022), non-local means filter (Qian et al., 2017; Soto et al., 2017) and anisotropic diffusion filter (Luo et al., 2020; Zhang et al., 2022) have been proposed and demonstrated to enhance the SNR of the BGSs along the OFC. The study Liu et al.(2022) shows significant improvement in measurement uncertainty by using one-dimensional denoising convolutional neural network (1D-DnCNN) for a 6 km OFC in Raman scattering-based distributed optical fiber sensor. In addition, the use of general regression neural network (GRNN) has proven superior for accurate temperature extraction in BOTDA sensors (Zhou et al., 2021). A comprehensive review of recent research works presented in (Venketeswaran et al., 2021) also reports the advantages of using signal-denoising algorithms to enhance measurement accuracy of fiber optic sensors. However, such a denoising technique includes extra runtime in processing BGSs. Moreover, the determination of BFSs from local BGSs is usually performed by applying NLSF. The operating principle of NLSF is based on the process of iterative optimization, which entails substantial time to determine BFSs if a great number of BGSs is required to be processed for the distributed monitoring of temperature throughout a long OFC. Consequently, high-speed signal processing techniques are essential for fast monitoring of distributed temperature in BOTDA sensors.

Within this framework, we have proposed using total variation denoising (TVD) to improve the SNR of BGSs collected from BOTDA experiment. The SNR improvements due to the use of TVD have been analyzed explicitly for the BGSs collected with ten different T_N. We have also proposed TVD and Euclidean distance-based pattern recognition (TEPR) for distributed temperature monitoring over 38.2 km OFC. The performances of TEPR have been evaluated rigorously in terms of measurement uncertainty, spatial resolution and signal processing speed.

Experimental Setup

The collection of BGSs along the OFC has been accomplished via the conventional BOTDA setup (Azad et al., 2017) shown in Fig. 1.

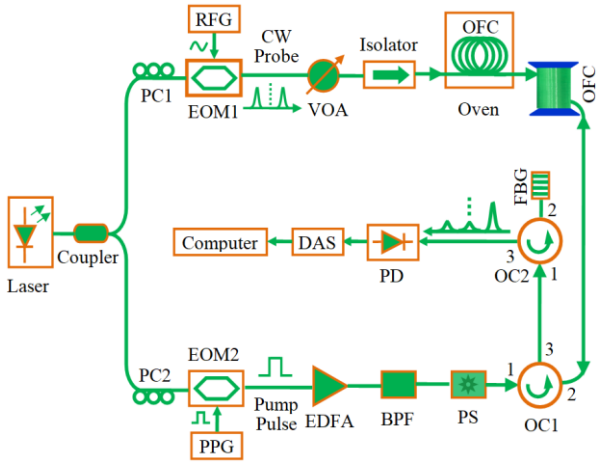

Fig. 1. Setup of BOTDA sensor

As shown in Fig. 1, the beam of light outputted by a CW-laser at 1550 nm is divided by the coupler to launch through the setup. The split beams pass through polarization controllers PC1 and PC2 to control the polarization state of light beams. To form double-sideband suppressed-carrier probe signal in the upper branch, the output of a radio frequency generator (RFG) is inputted to the electro-optic modulator (EOM1). The power of the probe light is tuned with the variable optical attenuator (VOA). Afterward, the isolator restricts the propagation of pump pulses from the reverse path but assists the probe signal to be passed through it in the forward direction to the far end of the OFC.

To generate pump pulses in the lower branch, the second electro-optic modulator (EOM2) is used. This EOM2 is assisted by the pulse-pattern generator (PPG). The pump pulses are next amplified by the erbium-doped fiber amplifier (EDFA). In this amplification process, the spontaneous emission noise also becomes amplified, which is eliminated by the band-pass filter (BPF). The polarization scrambler (PS) in the lower branch helps to diminish fading of Brillouin gain. These pump pulses are then directed from port 1 to port 2 of the optical circulator (OC1) to be launched through the near end of the OFC.

Two oppositely directed signals (i.e., pump and probe) interact inside the OFC via SBS, and both the lower and upper sidebands of the probe signal get amplified. The upper sideband is next nullified by the fiber Bragg grating (FBG) filter connected at port 2 of optical the circulator (OC2) and the photodetector then detects the desired lower sideband. The data acquisition system (DAS) acquires BOTDA traces. These traces are stored in the computer and used to form local BGSs along the OFC. These BGSs are finally processed to monitor the distributed temperature along the OFC.

Operating Principle

In our work, the experimental noisy BGSs collected throughout the OFC have been denoised first by utilizing total variation denoising (TVD). Then, a database comprising relevant ideal BGSs was constructed. Finally, Euclidean distance based pattern recognition has been applied among the denoised BGSs along the OFC and the ideal BGSs in the database to determine the temperature distribution from the experimental BGSs.

Total variation denoising (TVD) is a widely-used technique for reducing the total variation of an image and eliminating undesirable information while maintaining important details, such as edges (Rudin et al., 1992; Tang and Fang, 2016; Kamalaveni et al., 2018; Jin and Luan, 2020). This study considers the combined noisy BGSs along the OFC as a 2D image *B*. Such noisy image comprising experimental BGSs can be modeled as follows:

$$B(p,q) = D(p,q) + n(p,q) \quad (1)$$

Where $D(p,q)$ is the original image corrupted by the noise $n(p,q)$ and (p,q) is the pixel position in image $B(p,q)$. Due to the random nature of $n(p,q)$, the total variation (TV) in $D(p,q)$ is much smaller than that in $B(p,q)$. Consequently, the denoising of $B(p,q)$ is to find an estimate of $D(p,q)$ having smaller TV than that of $B(p,q)$ (Rudin et al., 1992). In such a process of TVD, the estimated image should also be well-matched with $B(p,q)$. This can be accomplished using TVD by minimizing the energy function given by (Liao et al., 2015; Kamalaveni et al., 2018)

$$\min_{B} E(D) = \int_{\Omega} |\nabla D| dpdq + \lambda \int_{\Omega} (D - B)^2 dpdq \qquad (2)$$

where Ω is the total number of pixels in $B(p,q)$, $|\nabla D(p,q)|$ is the gradient magnitude at position (p,q), and λ is the regularization parameter (Kamalaveni et al., 2018). The proper choice of λ controls the balance between the denoising level of $B(p,q)$ and the matching of the denoised image with $D(p,q)$ (Liao et al., 2015).

The denoised image D obtained after applying TVD consists of a denoised version of experimental noisy BGSs in B. The denoised BGSs in D are next processed using Euclidean distance-based pattern recognition to monitor the distributed temperature along the OFC. Such process (i.e., TEPR) is depicted in Fig. 2.

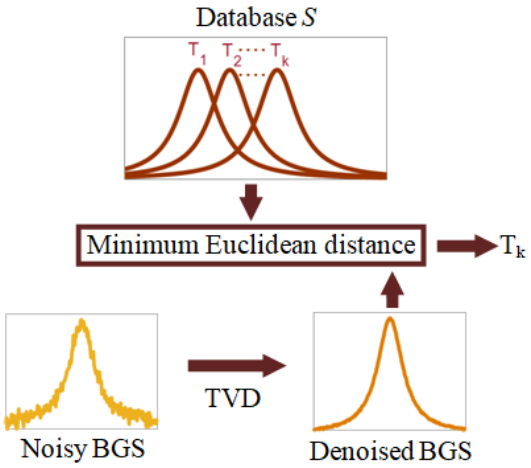

Fig. 2. The process of temperature monitoring using TEPR

As illustrated in Fig. 2, the temperature monitoring using the proposed technique of TEPR uses a database S comprising numerous ideal BGSs associated with known temperature. The process of constructing such a database will be analyzed in detail later in the results and discussion section. To apply TEPR, the experimental noisy BGSs along the OFC are first denoised by TVD. The denoised BGSs in D are then matched with the ideal BGSs in S, as shown in Fig. 2. For each BGS in D, we determine its best match with the ideal BGSs in S. This best match is defined in terms of minimum Euclidean distance. If the BGSs in S and D are represented by vectors s and d, respectively each having m data points, the Euclidean distance (l) between s and d is then given by (Azad et al., 2017)

$$l(s,d) = \sqrt{\sum_{i=1}^{m} (s_i - d_i)^2} \qquad (3)$$

The known temperature associated with the best-matched ideal BGS in S is designated as the temperature associated with the experimental noisy BGS. The process is repeated for all the experimental BGSs along the OFC for the distributed temperature monitoring throughout the 38.2 km OFC.

To compare the performance of TEPR, we also determine the temperature distributions directly from the experimentally noisy BGSs by applying NLSF. Since the BOTDA-measured BGSs are ideally modeled by the Lorentzian function (Azad et al., 2017; Haneef et al., 2018), we have utilized this function in NLSF. Such function is given by

$$g(\upsilon) = \frac{g_B}{1 + 4\left[(\upsilon - \upsilon_B)/(\Delta\upsilon_B)\right]^2} \qquad (4)$$

where g_B, υ_B and $\Delta\upsilon_B$ are termed as the peak gain, BFS and linewidth of the BGS, respectively. In NLSF, the parameters g_B, υ_B and $\Delta\upsilon_B$ of function given by Eq. (4) are updated iteratively to find the best-fit between this function and the BGS in term of least-squares error. The updated υ_B is estimated to be the BFS of the BGS used in NLSF. It is worth to mention that the SNR of experimental noisy BGS as well that of denoised BGS obtained after applying TVD has been calculated (Azad et al., 2017) in this study by

$$\mathrm{SNR(dB)} = 10\log_{10}\left(\frac{g_B^2}{\sigma^2}\right) \qquad (5)$$

where σ^2 is the variance of residuals (i.e., differences between the fitted and observed BGSs) in NLSF.

Results and Discussion

In our experiment, we used a 38.2 km long OFC in the BOTDA sensor shown in Fig. 1. We put ~600 m

fiber from the last part of the OFC into an oven and the temperature of the oven was set at 70°C. To collect local BGSs at every 0.4 m along the OFC, BOTDA-traces have been collected at a sampling rate of 250 MHz. The BGSs have been collected for the frequency range from 10.76 GHz to 11.01 GHz with 1 MHz spacing. The width of pump pulses has been fixed to 20 ns to realize a 2 m spatial resolution. The BGSs along the OFC have been collected by adopting ten T_N (i.e., T_N =100 to 1000 with a step of 100). The experimental BGSs along the OFC obtained for T_N = 100 and their corresponding denoised BGSs obtained after applying TVD are shown in Fig. 3 (a) and (b), respectively.

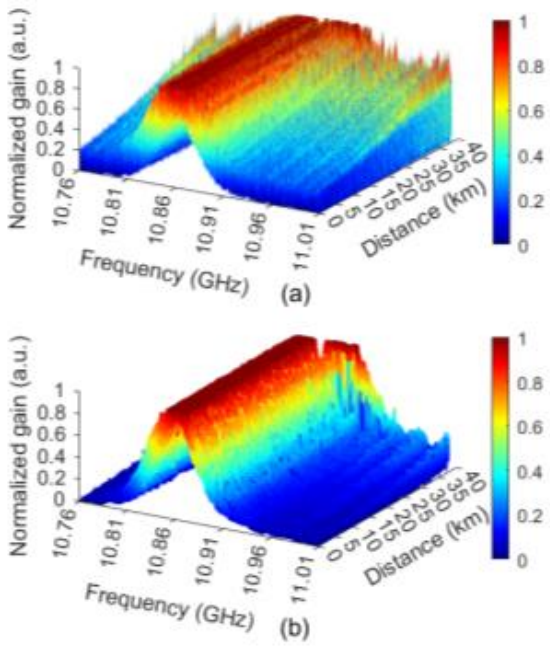

Fig. 3. Distributions of (a) experimental noisy BGSs and (b) denoised BGSs

It is observed that the level of noise in BGSs shown in Fig. 3(a) is much higher, which has been improved radically due to the use of TVD, as shown in Fig. 3(b). To observe the SNRs of noisy and denoised BGSs, we have next computed the SNRs of BGSs along the OFC shown in Fig. 3 by applying Eq. (5). Such SNRs for T_N = 100 are shown in Fig. 4.

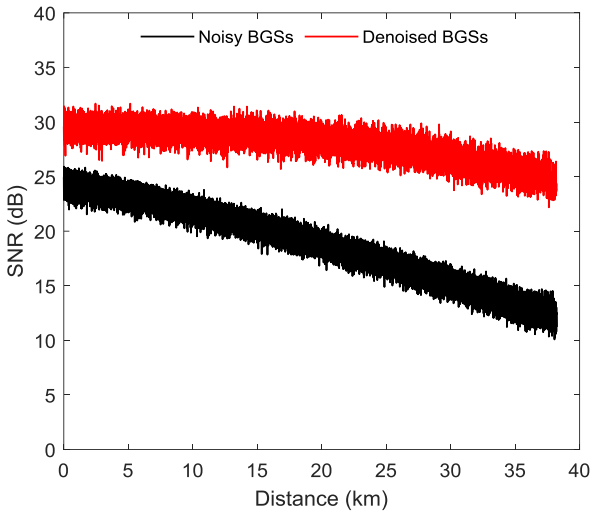

Fig. 4. SNRs of BGSs along the optical fiber

The results in Fig. 4 indicate that the SNRs of experimental noisy BGSs vary along the 38.2 km OFC, notably mainly due to fiber attenuation (Azad, 2022). However, the use of TVD on the noisy BGSs manifests a significant improvement in SNR, especially at the end of OFC, where the SNRs of noisy BGSs are the lowest. To quantify the variation of SNRs with T_N, we have also computed the average SNR of the BGSs along the last 500 m OFC. The results are shown in Fig. 5.

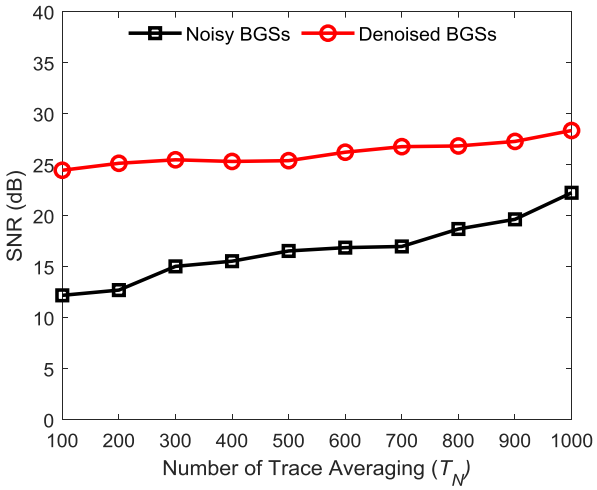

Fig. 5. Average SNR of BGSs along the last 500 m optical fiber

It can be observed in Fig. 5 that the SNRs of experimental BGSs increase if a larger T_N is

adopted to collect BGSs. For instance, the average SNR of experimental noisy BGSs in Fig. 5 varies from its lowest value of 12.21 dB to its highest value of 22.27 dB for adopting T_N = 100 and T_N = 1000, respectively. However, TVD-based NLSF can provide many improved SNRs of 24.48 dB and 28.37 dB for the same T_N of 100 and 1000, respectively. Consequently, TVD can improve the SNR by 12.27 dB and 6.10 dB for the BGSs collected with T_N of 100 and 1000, respectively. Notably, the improvement of SNR at smaller T_N in Fig. 5 is much larger than that at larger T_N. This is because the average SNR of BGSs at higher T_N is already much better as compared to that at lower T_N. For the BGSs having such higher SNR, TVD has a little to improve. The results in Fig. 5 signify that TVD can offer significantly improved SNR, which also helps to improve the measurement uncertainty of the BOTDA sensors.

As mentioned earlier, the operating principle of TEPR is based on the database comprising ideal BGSs. The BGSs in such a database should ideally mimic the BGSs obtained from the BOTDA experiment under various experimental conditions (e.g., fiber length, temperature, and pump-pulse width). In this study, the ideal BGSs in the database are constructed with the Lorentzian function given by Eq. (4). For using Eq. (4), the peak gain of the ideal BGSs is normalized to be g_B = 1. To monitor temperature within the range from 0 ºC to 100 ºC using the BOTDA sensor, υ_B (BFS) of each BGS in the database has been varied within the range from 10.834 GHz to 10.932 GHz (with the BFS spacing of 0.2 MHz) depending on the characteristics (i.e., intercept of ~10.83415 GHz and slope of ~0.97497 MHz/ºC) of the OFC (Azad et al., 2017; Azad, 2022). The linewidth ($\Delta\upsilon_B$) to be used in Eq. (4) has been decided based on the linewidths of the experimental BGSs. To decide so, we have first denoised the experimental noisy BGSs by applying TVD. The linewidths of the denoised BGSs are then determined by utilizing NLSF. For adopting 20 ns pump-pulse during the BOTDA experiment, the linewidths of such denoised BGSs for T_N =1000 (the highest T_N used in this study) are shown in Fig. 6. The average linewidth within every 1 km OFC are also plotted in Fig. 6.

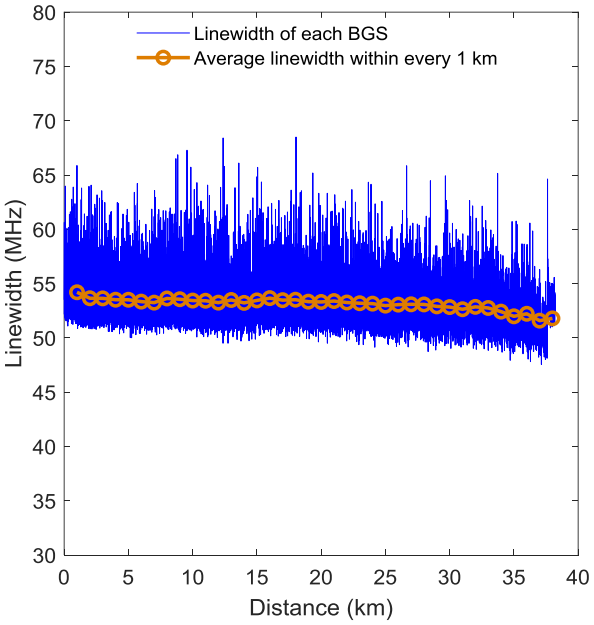

Fig. 6. Variation of the linewidth of BGSs along the optical fiber

It is noticed in Fig. 6 that the average linewidths within every 1 km OFC are ~53 MHz. Consequently, we have set $\Delta\upsilon_B$ = 53 MHz in Eq. (4) for constructing the database. For monitoring temperatures from 0 ºC to 100 ºC, the database thus contains a total of k = 491 ideal BGSs.

Next, we have evaluated the suitability of using TEPR and the constructed database for monitoring temperature distributions from the local BGSs along the OFC collected by adopting different T_N. The process of such a monitoring system is depicted in Fig. 2, in which the experimental noisy BGSs along the OFC are first denoised by applying TVD. Then, we have found the best match between each denoised BGS along the OFC and ideal BGSs in the database based on minimum Euclidean distance. The temperature distribution provided by TEPR for local BGSs collected at T_N = 100 is shown in Fig. 7. The

temperature distribution obtained for applying NLSF on experimental noisy BGSs at T_N = 100 are also shown in Fig. 7 for comparison.

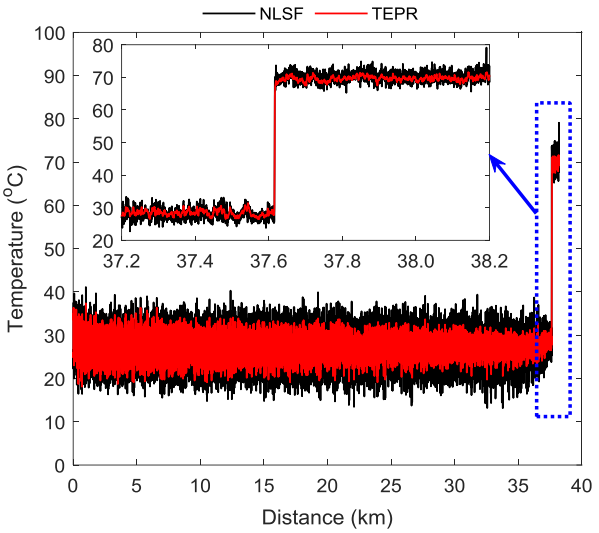

Fig. 7. Temperature distributions along the optical fiber

It is clear from Fig. 7 that the temperature fluctuations provided by TEPR are much smaller than that provided by NLSF. The smaller fluctuations in the temperature distribution due to the use of TEPR offer much reduced uncertainties in monitoring distributed temperature.

The denoising algorithm operation relies on eliminating the signals' high-frequency components (Azad, 2022). For such algorithm in BOTDA sensors, the BGSs along the OFC can be over-smoothed which can also deteriorate the experimental spatial resolution. To examine this, the distributions of temperature provided by NLSF and TEPR are plotted in Fig. 8 along the section of the OFC at which the distributions rise sharply from room temperature to 70 ºC. Such temperature distributions confirm that TEPR can maintain the experimental spatial resolution, which is 2 m in our study for adopting 20 ns pump-pulse.

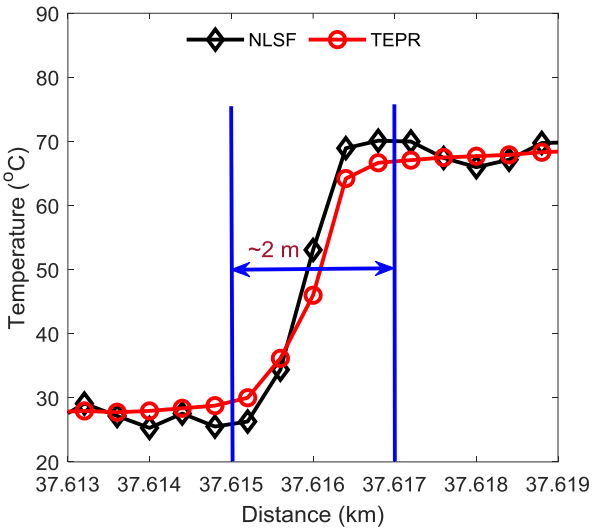

Fig. 8. Spatial resolution of the sensor

The results presented in Figs. 4 and 5 specify that the use of TVD can notably improve the SNR of the experimental BGSs. As a result, the fluctuations in the temperature distributions also reduce significantly as can be seen in Fig. 7. To quantify the reduction of such fluctuations, we have computed the uncertainties in monitoring temperature distributions. The uncertainty for each T_N is defined as the standard deviation of temperatures along the last 500 m OFC heated inside the oven. The results are plotted in Fig. 9.

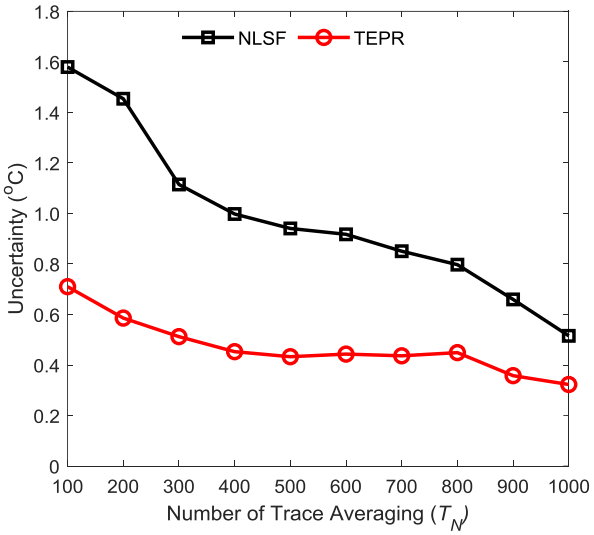

Fig. 9. Uncertainty in temperature monitoring

The results in Fig. 9 confirm that using TEPR provides significantly reduced measurement uncertainties compared to NLSF for each T_N adopted in this study. For instance, the uncertainty provided by NLSF for T_N = 100 is 1.58 ºC for the BGSs along the last 500 m fiber having SNR of 12.21 dB as shown in Fig. 5. For the same T_N, TEPR can provide much-reduced uncertainty of 0.71 ºC. Consequently, using TEPR can improve the measurement uncertainty by 55.06% at T_N = 100, the lowest T_N (i.e., lowest SNR of 12.21 dB) adopted in this study. This improvement in measurement uncertainty is much better than ~44.60% as reported by Zhoua et al.(2021), in which the use of GRNN and curve fitting method (i.e., NLSF) can provide root-mean-square errors of ~0.36 ºC and ~0.65 ºC, respectively, for the BGSs having similar SNR of 12 dB. However, the improvement of uncertainties for adopting higher T_N, such as T_N of 400, 700, and 1000 are 54.61%, 48.68% and 37.36%, respectively. These results suggest that the improvement of uncertainties decreases if a larger T_N is adopted to collect the BGSs from the BOTDA experiment. This is because the SNRs of the local BGSs collected at larger T_N is also larger. In such cases, the denoising of BGSs using TVD can improve the SNRs a little, as the noise level in the experimental BGSs is already much smaller.

Finally, we have compared the speed of NLSF and TEPR in monitoring the temperature distributions along the OFC. To do so, we have computed the runtimes taken by NLSF and TEPR to monitor temperature distributions from the local BGSs collected at different T_N. In the calculation of runtimes of TEPR, we have included the runtime taken by TVD and that taken by Euclidean distance-based pattern recognition. The speed of TEPR is calculated in terms of relative runtimes, which are the ratios of runtimes taken by NLSF to that taken by TEPR for each T_N. The results are shown in Fig. 10.

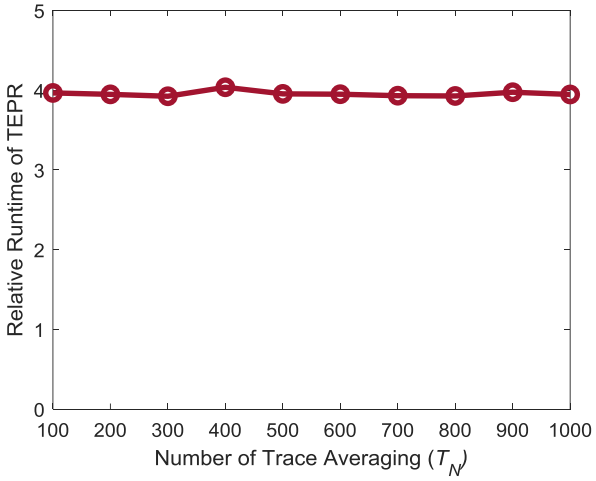

Fig. 10. Relative runtime of TEPR

It is clear from Fig. 10 that the relative runtimes of TEPR for different T_N are almost the same. The results in Fig. 10 signify that the monitoring of distributed temperature using TEPR is ~4 times faster than that of NLSF. It is worth mentioning that the use of GRNN (Zhou et al., 2021) can provide ~7 times faster processing speed over NLSF but can offer a 44.60% improvement of measurement uncertainty which is much lower than that of 55.06% achieved in this study.

Conclusion

This paper represents a rigorous study using TVD and Euclidean distance-based pattern recognition (TEPR) for the distributed temperature monitoring in BOTDA sensors. The TVD is first used to denoise the experimental BGSs. Then, a custom-made database comprising ideal BGSs is constructed and used by the Euclidean distance-based pattern recognition technique to monitor the distributed temperature along a 38.2 km optical fiber cable. The results show that the use of TVD can significantly improve the SNR of experimental BGSs up to 12.27 dB. Consequently, TEPR can improve the measurement uncertainty by up to 55.06% compared to NLSF without worsening the spatial resolution of BOTDA sensors. In addition, the signal processing speed of the proposed TEPR is ~4 times faster than that of NLSF. Therefore, the proposed TEPR can serve as a potential tool for

high-performance monitoring of distributed temperature using BOTDA sensors.

Acknowledgments

The authors are grateful to the University of Dhaka, Bangladesh, for the financial support of this work under the Centennial Research Grant (CRG). The authors also acknowledge the support of the 'Photonics Research Institute' at The Hong Kong Polytechnic University, Hong Kong SAR, for the facility of the experiment.

References

Angulo-Vinuesa X, Martin-Lopez S, Corredera P and Gonz´alez-Herr´aez M. Raman-assisted Brillouin optical timedomain analysis with sub-meter resolution over 100 km. Opt. Exp. 2012; 20(11): 12147-12154.

Azad AK, Khan FN, Alarashi WH, Guo N, Lau APT and Lu C. Temperature extraction in Brillouin optical time-domain analysis sensors using principal component analysis based pattern recognition. Opt. Exp. 2017; 25(14):16534-16549.

Azad AK. Analysis of 2D Discretewavelet transform based signal denoising technique in brillouin optical time domain analysis sensors. Dhaka Univ. J. App. Sci. Engg. 2020; 5(1&2):1-8.

Azad AK. Extraction of temperature distributions in brillouin optical time domain analysis sensors using 2D wiener filter based matched filter detection. Dhaka Univ. J. App. Sci. & Engg. 2022; 6(2): 30-38.

Ba D, Wang B, Zhou D, Yin M, Dong Y, Li H, Lu Z and Fan Z.Distributed measurement of dynamic strain based on multislope assisted fast BOTDA. Opt. Exp. 2016; 24(9): 9781-9793.

Haneef SM, Yang Z, Thévenaz L, Venkitesh D and Srinivasan B. Performance analysis of frequency shift estimation techniques in Brillouin distributed fiber sensors. Opt. Exp. 2018; 26(11): 14661-14677.

Iribas H, Loayssa A, Sauser F, Llera M and Floch SL. Cyclic coding for Brillouinoptical time-domain analyzer using probe dithering. Opt. Exp. 2017; 25(8): 8787-8800.

Jia X, Rao Y, Chang L, Zhang C and Ran Z. Enhanced sensing performance in long distance Brillouin optical time-domain analyzer based on Raman amplification: Theoretical and experimental investigation. J. Lightwave Technol. 2010; 28(11): 1624–1630.

Jin C and Luan N. An image denoising iterative approach based on total variation and weighting function. Multimed Tools App.2020; 79: 20947–20971.

Kamalaveni V, Narayanankutty KA, Veni S and Soman KP. Survey on Total Variation based Image Regularization Algorithms for Image Denoising. Int. J. Pure App. Math. 2018; 118(20): 3723-3730.

Liao CH, Choi JH,Zhang D,Chan SH and Cheng JX. Denoisingstimulated Raman spectroscopic images by total variation minimization. J. Physical Chem. 2015; 119(33): 19397-19403.

Liu Z, Wu H, Du H, Luo Z and Tang M. Distributed temperature and curvature sensing based on Raman scattering in Few-Mode fiber. IEEE Sensors J. 2022; 22(23): 22620-22626.

Luo K, Wang B, Guo N, Yu K, Changyuan Yu C and Lu C. Enhancing SNR by anisotropic diffusion for brillouin distributed optical fiber sensors. J. Lightwave Technol. 2020; 38(20): 5844-5852.

Mariñelarena J, Iribas H and Loayssa A. Pulse coding linearization for Brillouin optical time-domain analysis sensors. Opt. Lett. 2018; 43(22):5607-5610.

Motil A, Bergman A and Tur M. State of the art of Brillouin fiber-optic distributed sensing. Opt. Laser Technol. 2016; 78: 81-103.

Qian X, Jia X, Wang Z, Zhang B, Xue N, Sun W, He Q and Wu H. Noise level estimation of BOTDA for optimal non-local means denoising. Appl. Opt. 2017; 56(16): 4727-4734.

Rudin LI, Osher S and Fatemi E. Nonlinear total variation based noise removal algorithms. Physica D: Nonlinear Phenom. 1992; 60(1-4): 259-268.

Soto MA, Ramírez JA and Thévenaz L. Intensifying the response of distributed optical fibre sensors using 2D and 3D image restoration. Nat. Com. 2016; 7: 10870.

Soto MA, Ramírez JA and Thévenaz L. Optimizing image denoising for long-range Brillouindistributed fiber sensing. J. Lightwave Techno. 2017; 36(4): 1168-1177.

Soto MA, Taki M, Bolognini G and Pasquale FD. Simplex-coded BOTDA sensors over 120 km SMF with 1-m spatial resolution assisted by optimized bidirectional Raman amplification. IEEE Photon. Tech. Lett. 2012; 24(20): 1823-1826.

Tang L and Fang Z. Edge and contrast preserving in total variation image denoising. EURASIP J. Adv. Signal Process. 2016; 13: 1-21.

Venketeswaran A, Lalam N,Wuenschell J,Ohodnicki PR, Badar M, Chen KP, Lu P, Duan Y, Chorpening B and Buric M. Recent advances in machine learning for fiber optic sensor applications. Adv, Intell. Syst. 2021; 4: 2100067.

Wang S, Yang Z, Zaslawski S and Thévenaz L. Short spatial resolution retrieval from a long pulse Brillouin optical time-domain analysis trace. Opt. Lett.2020; 45(15): 4152-4155.

Zhang P, Wang B, Yang Y, Azad AK, Luo K, Yu K, Yu C and Lu C. SNR enhancement for Brillouin distributed optical fiber sensors based on asynchronous control. Opt. Exp. 2022; 30(3): 4231-4248.

Zhao L, Chen Y, Xu Z, Zhang X and Mou Q. Brillouin frequency shift error estimation formula for distributed optical fiber sensing technology based on Brillouin scattering. Appl. Opt. 2022; 61: 4354-4362.

Zhou H, Zhu H, Zhang Y, Huang M and Li G. Fast and accurate temperature extraction via general regression neural network for BOTDA sensors. In: Proceedings of SPIE, Vol. 12057. Ed. Yang Y.Twelfth International Conference on Information Optics and Photonics, 120573O-1;2021

J. Bangladesh Acad. Sci. 46(2); 203-211: December 2022 DOI: 10.3329/jbas.v46i2.63622

Journal of Bangladesh Academy of Sciences

Journal homepage: http://www.bas.org.bd/publications/jbas.html

Research Article

Iron (II) and Zinc (II) complexes of gemifloxacin mesylate: synthesis, characterization, serum binding profiling, and evaluation of antimicrobial activity

Fahima Aktar, Md. Jamal Hossain[1], Md. Zakir Sultan[2] and Mohammad A. Rashid[*]

Department of Pharmaceutical Chemistry, Faculty of Pharmacy, University of Dhaka, Dhaka, Bangladesh

ARTICLE INFO

Article History

Received: 01 December 2022
Revised: 20 December 2022
Accepted: 26 December 2022

Keywords: Gemifloxacin mesylate, TGA, FT-IR, Antimicrobial activity, Drug-protein interaction.

ABSTRACT

Gemifloxacin mesylate is a synthetic fluoroquinolone derived antimicrobial agent. Two metal complexes of gemifloxacin mesylate were synthesized *viz.* gemifloxacin-Fe and gemifloxacin-Zn. The formed complexes were characterized by using TLC, TGA and FT-IR spectra analyses. The formed complexes were then evaluated for antimicrobial activity. The newly formed two complexes were assessed against nine bacterial and one fungal strain, where gemifloxacin (30 µg/disc) was used as a reference standard. The new complexes showed better activity than the standard reference drug against *Klebsiella pneumoniae* among nine bacterial strains. But two bacterial species, *Acinetobacter lwoffii* and *Enterococcus faecium*, and the fungal strain *Candida albicans* showed complete resistance to the newly synthesized complexes and the reference standard. The drug protein interaction with the Bovine Serum Albumin (BSA) was also studied. The interaction mechanism was explored, suggesting that gemifloxacin and its Zn (II) complex interact with BSA via a static process while the Fe (II) complex interacts via a dynamic process and the lower Ksv value also indicated that drug - BSA complexes were formed in ground-state.

Introduction

Gemifloxacin mesylate (GeFo, Figure 1), chemically [(R,S)-7-[(4Z)-3-(aminomethyl)-4-(methoxyimino)1-pyrrolidinyl]-1-cyclopropyl-6-fluoro-1, 4-dihydro-4-oxo-1, 8-naphthyridine-3-carboxylicacid methane-sulfonate] is a broad-spectrum oral antibiotic of fluoroquinolone group (Piam et al., 2012).

GeFo has *in vitro* potent antibacterial activity against respiratory tract infection pathogens because it has good penetration into respiratory secretions, for example, into alveolar macrophages and the epithelial lining fluid, having enough concentrations at the site of the infection (Bolon, 2009; Turel, 2002; Andriole, 2000). GeFo gives activity by inhibiting host DNA synthesis as it inhibits both DNA gyrase and topoisomerase IV enzyme, essential for the growth of Bacteria. Fluoroquinolone antibiotics have also been found to have anti-inflammatory and anticancer effects, as revealed by some recently carried out experiments (Kuhlmann et al., 1998; Uddin et al., 2021). The drug-metal interaction of diverse deprotonated fluoroquinolones has been extensively studied. In many cases. the metal complexes of drugs are found to be more active than the parent compound (Johnson et al., 1999; Grossman et al., 2005; Kan et al., 2013). Considering the fact, two metal complexes (Iron (II) and Zinc (II)) with GeFo have been synthesized as an attempt to assess the physicochemical properties, protein profiling and to investigate their antibacterial properties.

[*]Corresponding author: <arpharm64@du.ac.bd>

[1]*Department of Pharmacy, State University of Bangladesh, Dhanmondi, Dhaka, Bangladesh*

[2]*Centre for Advanced Research in Sciences (CARS), University of Dhaka, Dhaka, Bangladesh*

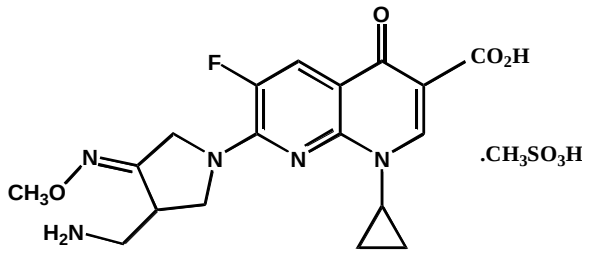

Fig. 1. Gemifloxacin mesylate.

Materials and methods

Chemicals and equipment

Analytical grade solvents and chemicals were used for all experimental purposes. The API of antibiotic gemifloxacin mesylate (purity 100.9%) was received as gift samples from Incepta Pharmaceuticals Ltd., Dhaka, Bangladesh. BSA solution of pH 7.4 was prepared using phosphate buffer. The experimentally used TLC plates (HSF-254) were purchased from Merck, Germany.

Preparation of pH 7.4 buffer solutions

Phosphate buffer was made ready by dissolving 235 ml of 0.01M K_2HPO_4 with 65 ml of 0.01M KH_2PO_4 and the mixture was raised to a volume of 1000 ml with DM water (Hossain et al., 2020a; Saha et al., 2012).

Synthesis of Gemifloxacin mesylate-Fe and Gemifloxacin mesylate-Zn complexes

The solid metal complexes, gemifloxacin mesylate-Fe *(*GeFo-Fe) and gemifloxacin mesylate-Zn (GeFo-Zn), were prepared by mixing a hot methanolic solution of the ligand (1 mM) with that containing the required amount of the appropriate metal chloride (0.5 mM). The reaction mixture was continuously refluxed on a water bath for 6.0-7.5 h at 60 ℃. The solutions were then filtered and left for crystallization at room temperature. In each case, a fine solid product was obtained, which was washed with the solvent. Gemifloxacin mesylate-metal complexes were synthesized with a 1:2 M ratio. Following the formation of the complexes, several chromatographic and spectroscopic analyses were done to characterize the complexes.

Thin layer chromatography (TLC)

To evaluate the formation of metal complexes, TLC was performed using methanol-chloroform-toluene (20:40:40) as the mobile phase.

Thermogravimetric analysis (TGA)

The thermogravimetric analyses (TGA) of the metal complexes were carried out at temperatures up to 600 ^oC by the thermogravimetric analyzer (TGA-50, Shimadzu, Japan). An aliquot of each complex (~3 mg) was heated in an aluminum pan with temperature rising rate at 10 °C/min under a nitrogen gas flow rate of 20 mL/min.

Fourier transform infrared spectrophotometry (FTIR)

The FTIR analyses of metal drug complexes were carried out at the wavelength from 400 cm^{-1} to 4000 cm^{-1}. About 100 mg of pure and dried KBr was added to 1 mg of each dried sample, then homogenously mixed with a mortar-pestle and pressed mechanically to make a pellet under the pressure of 8-10 tons. The prepared disc was placed in the IR beam path to acquire the spectrum.

Fluorescence quenching for profiling ligand-protein binding

The fluorescence studies were conducted at different concentrations of drug at 5 µM, 10 µM, 20 µM and 50 µM while BSA concentration was fixed at 10 µM. Most of the 295-400 nm range of fluorescence emission spectra were reported at 280 nm excitation wavelength. The test tubes containing the solution of BSA and the drug or its complexes were heated at least 10 min before the measurements (in fluorescence spectrophotometer F-7000) (Tanwir et al., 2012; Hossain et al., 2020b; Hossain et al., 2020c).

Antimicrobial screening

To assay the antimicrobial activity, the disc diffusion method (Biemer, 1973; Aktar et al., 2009) was used to evaluate the metal-drug complexes against nine bacteria (five gram positive bacteria viz.

Enterococcus faecium, *Streptococcus pneumoniae*, *Staphylococcus aureus*, *Streptococcus pyogenes*, and *Bacillus subtilis* with four gram-negative bacteria viz. *Acinetobacter lwoffii*, *Pseudomonas aeruginosa*, *Escherichia coli*, *Klebsiella pneumoniae*) and 1 fungal species (*Candida albicans*) collected as pure cultures from the Department of Genetic Engineering, University of Dhaka, Dhaka, Bangladesh. The antimicrobial activity of the drug metal complexes was evaluated by mapping the diameter of the zone of inhibition expressed in mm. Mean values were taken by repeating the experiment thrice times (Khatun et al., 2021; Salve et al., 2022).

Results and Discussion

Characterizations

Both crystalline and amorphous drug complexes were obtained. To prove the complexation, TLC was carried in methanol-chloroform-toluene (20:40:40). Single spot from the two complexes differed from the parent drug were found (Table 1). Each spot indicated the presence of a new complex.

Table 1. R_f values of pure GeFo and two metal complexes GeFo-Zn and GeFo-Fe.

Drug and complex	R_f value
GeFo	0.2
GeFo-Zn	0.4
GeFo-Fe	0.5

TGA of standard GeFo in Figure 2(a) revealed that 13.02% decomposition occurred at 237.80 °C and 46.98% at 490.84 °C. While metal complex GeFo-Zn exhibited 17.36% decomposition at 241.47 °C and 54.15% decomposition at 566.30 °C in Fig. 2(b). Another, the metal complex GeFo-Fe showed 22.24% decomposition at 284.37 °C and 79.49% decomposition at 566.65 °C Fig. 2(c).

FT-IR by providing information about the presence or absence of specific functional groups helps to compare two similar molecular structures. Moreover, when two pure samples display the same IR spectra, they can be described as the same compounds (Aktar et al., 2019). In contrast, any shifts or disappearance of peaks are directed toward the presence of a different compound. The IR spectra obtained after drug-metal interaction demonstrated a new pattern of peaks compared to pure drug powder.

The FTIR spectrum of gemifloxacin mesylate showed a peak at 1043.49 cm^{-1} corresponding to (C-F) bending and at 1463.97cm^{-1} for O-CH_3 bending (Fig. 3), at 1199.72 cm^{-1} for R-COOH Stretching, at 1631.78 cm^{1} for N-H scissoring, at 1716.65cm^{-1} for aromatic -C=O stretching and at 898.83 cm^{-1}due to C-H rocking (Nagasree et al., 2016). In both GeFo-Zn and GeFo-Fe these characteristic peaks of the parent compound were shifted (Serafin and Stańczak, 2009). The complexation may occur as in Fig. 4.

TGA thermograms were obtained from pure drugs and metal complexes. The TGA thermograms are shown in Fig. 2.

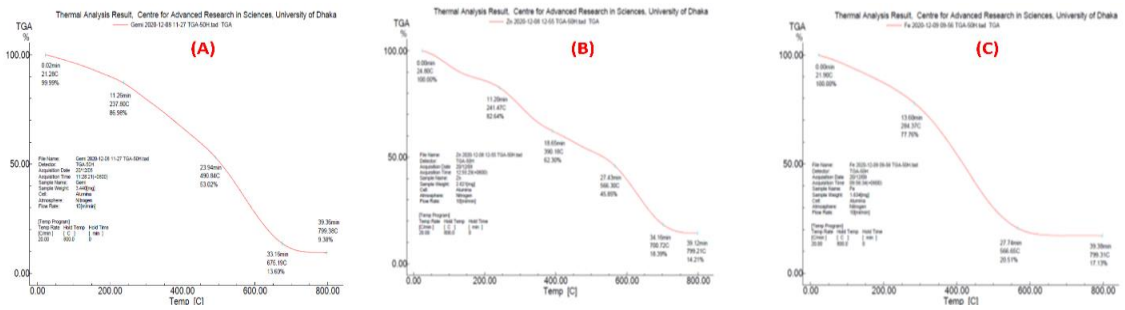

Fig. 2. TGA thermograms of A) pure GeFo, B) metal complex GeFo-Zn, C) metal complex GeFo-Fe.

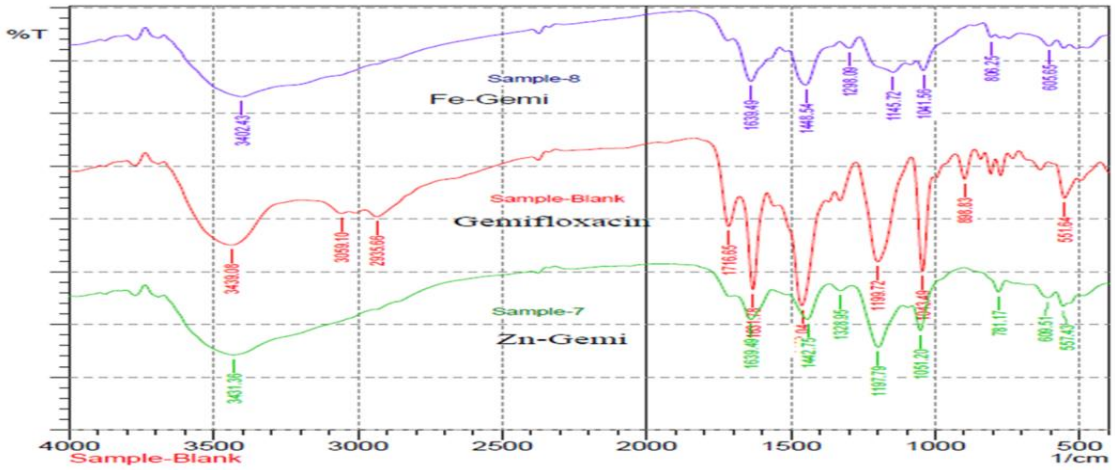

Fig 3. Overlaid FT-IR Overlaid FT-IR spectra of standard drug GeFo, metal complexes GeFo-Zn and GeFo-Fe.

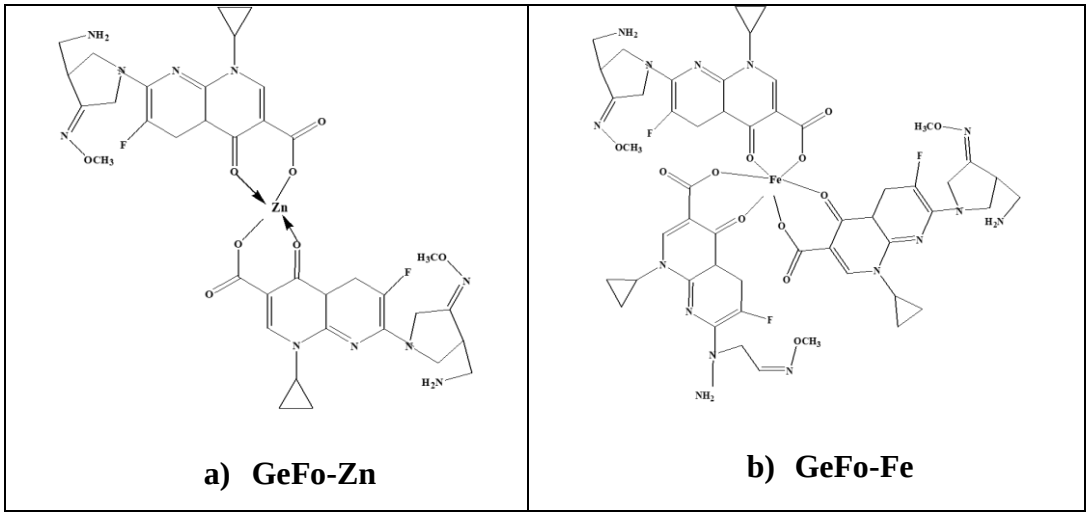

Fig. 4. Postulated structures of a) GeFo-Zn, and b) GeFo-Fe.

GeFo and GeFo-Zn & GeFo-Fe complexes-induced fluorescence quenching of BSA

Due to the fluorescence emission of its phenylalanine (Phe), tyrosine (Tyr), and tryptophan (Trp) residues, BSA has the inherent fluorescence property. Tryptophan is the dominant innate fluorophore as it is sensitive to local environmental changes due to conformational transition, subunit association, complex formation, and denaturation (Ghisaidoobe and Chung, 2014). Fluorescence quenching study provides precious information about the interaction mechanism between protein and ligand (Hossain et al., 2021a). Herein, fluorescence spectra of BSA (10 µM) upon exposure to various concentrations of GeFo and its metal complexes (0-50 µM) were measured and shown in Fig. 5. In the absence of the drug and drug complexes, BSA showed a typical emission spectrum with a maximum peak at 340 nm at 280 nm excitation wavelength. The fluorescence intensity of BSA gradually declined with the increased concentrations of drug and metal complexes.

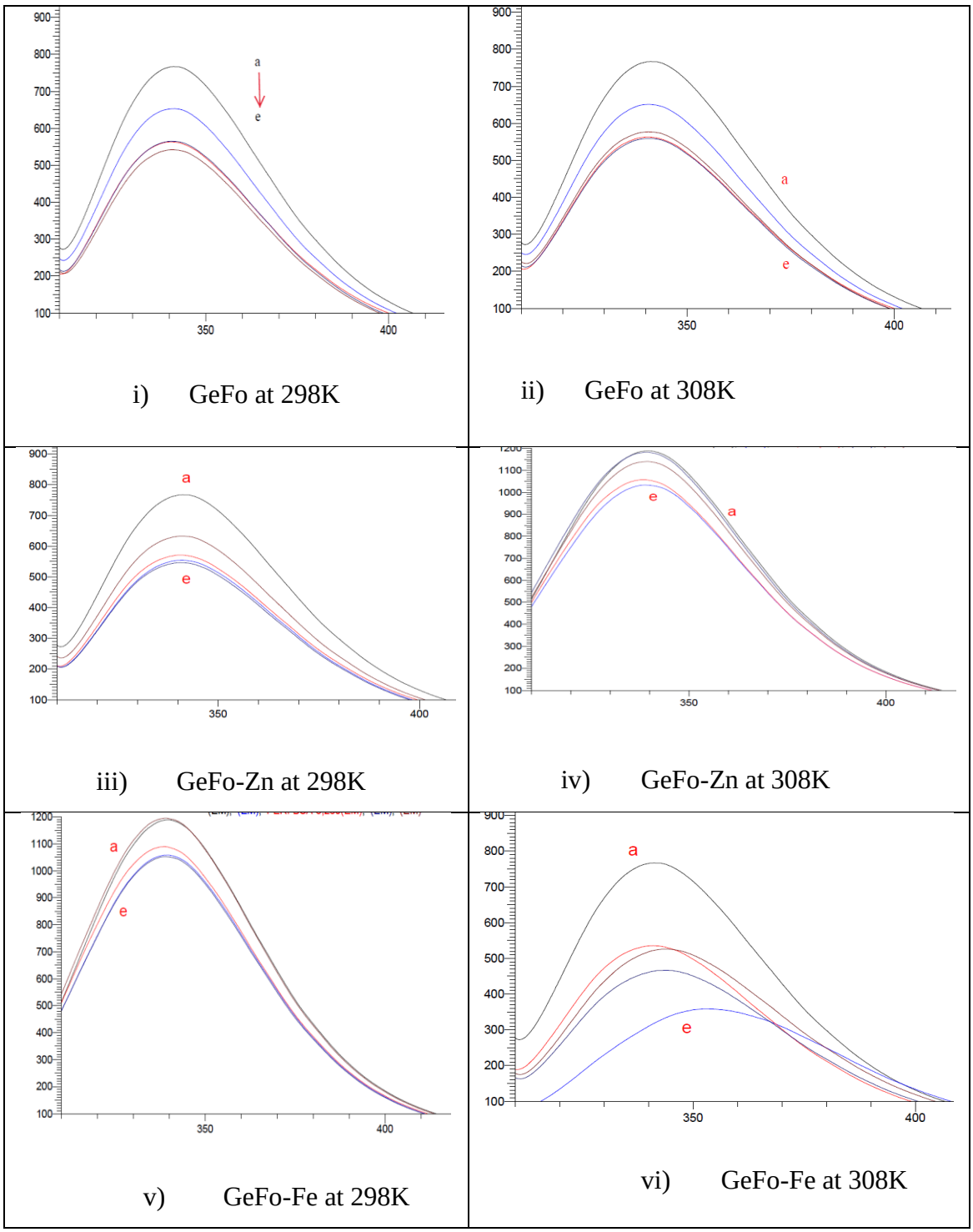

Figure 5. Fluorescence spectra of BSA (10 µM) in the presence of drugs and its metal complexes (a-e: 0, 5, 10, 20, and 50 µM) upon excitation with 280 nm wavelength at 298K and 308 K.

The Stern-Volmer equation (Equation (1)) was applied at the excitation wavelength of 280 nm to the elucidation of the interaction mechanism between BSA and the drugs. The plots of F_0/F versus ligand concentration ([Q]) fitted with the Stern-Volmer equation also help to distinguish between dynamic and static interactions between protein and its ligand. The static mechanism refers to the ground-state complex formation, while the dynamic mechanism means to the collisional encountering process (Hossain et al., 2021b). In the Stern-Volmer plot, a linear trend proposes that the interaction is guided by a single mechanism, either a static or dynamic process. If the Stern-Volmer constant (Ksv) increases with increasing temperature, then the dynamic process is mainly involved in the interaction system. As the temperature rising enhances diffusion and collision of protein and its ligand, that ultimately promotes the dynamic process as indicated by the increased slope of the Stern-Volmer plot. On the other hand, the rising temperature destabilizes the protein-ligand complex and substantially reduces the Ksv in the static quenching process (Hossain et al., 2021b).

$$F_0/F = 1 + Ksv[Q] = 1 + kq\,\tau_o[Q] \quad \ldots\ldots\ldots\ldots\ldots\ldots (1)$$

F_0 and F are the fluorescence intensities in the absence and the presence of quencher (drug and metal complexes), respectively. [Q] stands for the concentration of quencher. Ksv and kq are the Stern–Volmer constant and the biomolecular quenching rate constant, respectively. $\tau_o$is the average lifetime of the fluorophore (BSA) in the absence of quencher [$\tau_o = 1 \times 10^{-8}$s] (Hossain et al., 2021a; Hossain et al., 2021b). In this study, the fluorescence quenching was studied by measuring the fluorescence at an excitation wavelength of 280 nm at two different temperatures (298 K and 308 K). The fluorescence of BSA was dramatically reduced when exposed to the drug and drug complex in a range of 0-50 µM (Fig. 5). The quenching was inversely proportional to the temperature, where attenuation of fluorescence quenching was observed with the rising temperature. The F0/F versus drug and drug metal concentrations plots were perfectly fitted with a linear model of the Stern-Volmer equation (Fig. 6a, 6b and 6c), recommending a single mechanism involved in the BSA-drug interaction.

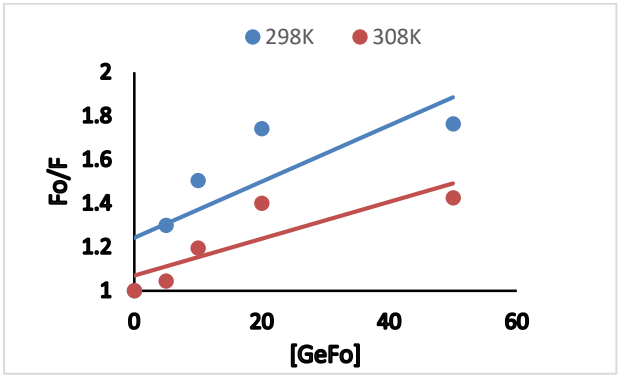

(a) [GeFo]×10^{-6} M

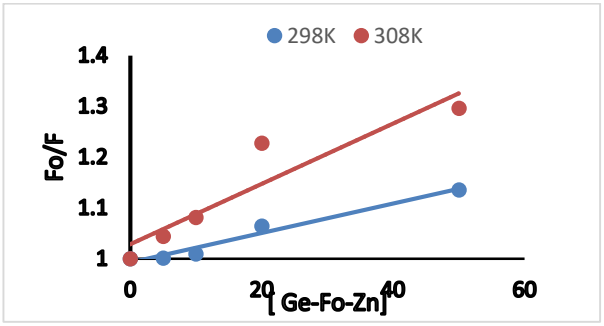

(b) [GeFo-Zn]×10^{-6}M

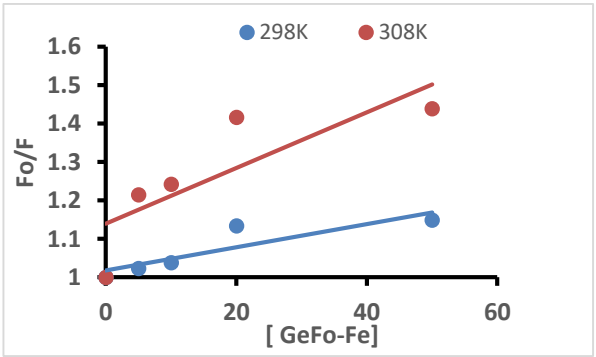

(c) [GeFo-Fe]×10^{-6}M

Fig. 6. (a) Gemifloxacin, GeFo, (b) Gemifloxacin-Zn, GeFo-Zn, (c) Gemifloxacin-Fe, GeFo-Fe the Stern-Volmer plots of bovine serum albumin (BSA) in the presence of drugs at 298 and 308 K. [GeFo], [GeFo-Zn] and [GeFo-Fe]=0–50 µM; [BSA]=10 µM; λex =280 nm.

As the temperatures increased, the Ksv values decreased for GeFo and GeFo-Zn, while for GeFo-Fe complex Ksv value was increased (Table 2), suggesting the primary involvement of static and dynamic quenching processes, respectively. Moreover, the biomolecular quenching rate constants (kq) were found at a level of 10^{12} $M^{-1}s^{-1}$, which was 100 times higher than the maximum scattering collisional quenching constant of various quenchers (2×10^{10} $M^{-1}s^{-1}$) (Liu et al., 2018). Hence, the findings suggested that GeFo and GeFo-Zn interact with BSA via a static process by the ground-state complex formation, while GeFo-Fe interaction with BSA is a dynamic process.

Antimicrobial activities

In antimicrobial activity screening, the metal complexes showed less inhibitory activity than the standard gemifloxacin mesylate (30 µg/disc) except against the *K. pneumoniae.* Against *K. pneumoniae* both the Fe and Zn complexes showed higher inhibitory activity than the standard, which is 17±0.54 mm at dose GeFo-Zn (30 µg/disc), 18±0.32 mm at dose GeFo-Zn (60 µg/disc), 14 ±0.58 mm at dose GeFo-Fe (30µg/disc) and 18±0.15 mm at dose GeFo-Zn (60 µg/disc) while for GeFo it was 12±0.16 mm. Both the standard drug and the Fe and Zn complexes showed resistance against *A. lwoffii*, *E. faecium* and fungal species *C. albicans.* Detailed results are shown in Table 3.

Table 2. Stern-Volmer constants for BSA-GeFo, BSA-GeFo-Zn, and BSA-GeFo-Fe interaction at different temperatures.

Sample	T (K)	1/T	Ksv $\times 10^4$ (M^{-1})	kq $\times 10^{12}$ ($M^{-1}S^{-1}$)
GeFo	298	0.0033	1.29±0.38	1.29±0.38
	308	0.0032	0.84±1.23	0.84±1.23
GeFo-Zn	298	0.0033	0.2± 0.05	0.2± 0.05
	308	0.0032	0.05±0.87	0.05±0.87
GeFo-Fe	298	0.0033	0.3±0.11	0.3±0.11
	308	0.0032	0.7±0.05	0.7±0.05

Table 3. Antimicrobial activity of standard drug gemifloxacin (30 µg/disc), Zn complexes (30 µg/disc, 60 µg/disc), and Fe complexes (30 µg/disc, 60 µg/disc) against ten different micro-organisms.

List of microorganisms	Zone of Inhibition (mm)				
Bacteria	Zn-gemi 30 µg/disc	Zn-gemi 60 µg/disc	Fe-gemi 30 µg/disc	Fe-gemi 60 µg/disc	Gemifloxacin mesylate 30 µg/disc
Acinetobacter lwoffii	R	R	R	R	R
Enterococcus faecium	R	R	R	R	R
Pseudomonas aeruginosa	12±0.23	17±0.54	9±0.54	15±0.56	24±0.34
Streptococcus pneumoniae	13±0.17	20±0.32	12±0.24	18±0.34	28±0.16
Staphylococcus aureus	9±0.32	22±0.32	14±0.21	20±0.23	25±0.25
Streptococcus pyogenes	8±0.21	14±0.65	7±0.43	9±0.65	16±0.24
Escherichia coli	22±0.43	25±0.73	11±0.37	15±0.26	30±0.15
Bacillus subtilis	17±0.57	23±0.12	7±0.43	12±0.12	24±0.14
Klebsiella pneumoniae	17±0.54	18±0.32	14±0.58	18±0.15	12±0.16
Fungi					
Candida albicans	R	R	R	R	R

Note: R indicates the resistances against the corresponding microorganisms.

Conclusion

The newly synthesized two metal complexes of gemifloxacin mesylate *viz.* GeFo-Fe and GeFo-Zn were characterized using TLC, TGA, and FT-IR spectra analyses. The formed complexes were then evaluated for antimicrobial activity. Nine bacteria species and one fungal strain were assessed against the newly formed two complexes using gemifloxacin (30 µg/disc) as standard. Among nine bacteria strains, two species and the fungal strain showed complete resistance to the newly synthesized complexes and the standard. Against *Klebsiella* spp. the new complexes showed better activity than the standard drug. The drug-protein interaction was also studied using BSA. The interaction mechanism among the drug and metal complexes with BSA suggested that gemifloxacin and its Zn complex interacted with BSA via a static process while the Fe complex interacted via a dynamic process and the lower Ksv value also indicated that Drug -BSA complexes were formed in ground-state. Research suggests that the zinc and iron complexes of the antibiotic gemifloxacin mesylate may change the drug's efficacy. The findings open possibility of promoting the production and utilization of metal complexes of antibiotics for treating resistant bacteria.

Acknowledgment

The authors are grateful to Incepta Pharmaceuticals Ltd., Dhaka, Bangladesh, for providing APIs for the research; the Department of Genetic engineering, University of Dhaka, for providing fresh cultures of microorganisms and for providing laboratory facilities for antimicrobial study; Centre for Advanced Research in Sciences (CARS) for instrumental support; Mr. Ali (Lab Attendant, Department of Genetic engineering) and Mr. Konik Kumar Sarkar (Lab attendant, Drug Analysis and Research Laboratory, CARS, DU) for helping us during the research work.

Financial support:

The authors have received no financial support for conducting the research.

Data Availability:

All the data associated with this research are available in the manuscript.

Author contributions:

Fahima Aktar: Conceptualization, study design, methodology, data analysis and interpretation, drafting the original version.

Md. Jamal Hossain: Methodology, data curation, data analysis and interpretation, writing-reviewing and editing.

Md. Zakir Sultan: Methodology, data analysis and interpretation, writing-reviewing, and editing

Mohammad A. Rashid: Conceptualization, super-vision, writing-reviewing, and editing.

References

Aktar F, Kaisar MA, Kabir AH, Hasan CM, and Rashid MA. Phytochemical and biological investigations of *Ixora arborea* Roxb. *Dhaka Univ. J. Pharm. Sci*. 2009; 8(2): 161-166.

Aktar F, Sultan MZ and Rashid MA. In vitro complexation of olmesartan medoxomil with dapagliflozin, vildagliptin and metformin. *Dhaka Univ. J. Pharm. Sci*. 2019; 18(2): 271-280.

Andriole VT. The Quinolones: prospects. Chapter 16, 3rd ed. In: the quinolones. Andriole VT (ed.), Elsevier: New York, USA, 2000; 477-495.

Biemer JJ. Antimicrobial susceptibility testing by the Kirby-Bauer disc diffusion method. *Ann. Clin. Lab. Sci.* 1973; 3(2): 135-140.

Bolon MK. The newer fluoroquinolones. *Infect. Dis. Clin. North. Am.* 2009; 23: 1027-1051.

Ghisaidoobe AB and Chung SJ. Intrinsic tryptophan fluorescence in the detection and analysis of proteins: a focus on Förster resonance energy transfer techniques. *Int. J. Mol. Sci.* 2014; 15(12): 22518-22538.

Grossman RF, Rotschafer JC and Tan JS. Antimicrobial treatment of lower respiratory tract infections in the hospital setting. *Am. J. Med.* 2005; 118: 29-38.

Hossain MJ, Sultan MZ, Rashid MA and Kuddus MR. Does rabeprazole sodium alleviate the anti-diabetic activity of linagliptin? drug-drug interaction analysis by in vitro and in vivo methods. *Drug Res.* 2020a; 70(11): 519-527.

Hossain MJ, Sultan MZ, Rashid MA and Kuddus MR. In vitro interactions of secnidazole and its

iron (ii), copper (ii) complexes with bovine serum albumin by fluorescence quenching method. *Bangladesh Pharm. J*. 2020b; 23 (1): 1-9.

Hossain MJ, Rashid MA and Sultan MZ. Transition metal chelation augments the half-life of secnidazole: molecular docking and fluorescence spectroscopic approaches. *Drug Res.* 2020c; 70(12): 583-592.

Hossain MJ, Islam MS, Shahriar S, Sanam S, Emran TB, Khatun CS, Islam MR, Mitra S and Dhama K. Comedication of rabeprazole sodium causes potential drug-drug interaction with diabetic drug linagliptin: in-vitro and in-silico approaches. *J. Exp. Biol. Agric. Sci.* 2021a; 9: 528-542.

Hossain MJ, Sultan MZ, Rashid MA and Kuddus MR. Interactions of linagliptin, rabeprazole sodium, and their formed complex with bovine serum albumin: computational docking and fluorescence spectroscopic methods. *Anal. Sci. Adv*. 2021b; 2(9-10): 480-494.

Johnson DM, Jones RN, Erwin ME. Anti-streptococcal activity of SB-265805 (LB20304), a novel fluoronaphthyridone, compared with five other compounds, including quality control guidelines. *Diag. Microbiol. Infect. Dis*. 1999; 33(2): 87-91.

Kan JY, Hsu YL, Chen YH, Chen TC, Wang JY and Kuo PL. Gemifloxacin, a fluoroquinolone antimicrobial drug, inhibits migration and invasion of human colon cancer cells. *BioMed Res. Int.* 2013; 2013:159786.

Khatun MC, Muhit MA, Hossain MJ, Al-Mansur MA and Rahman SA. Isolation of phytochemical constituents from *Stevia rebaudiana* (Bert.) and evaluation of their anticancer, antimicrobial and antioxidant properties via in vitro and in silico approaches. *Heliyon*. 2021; 7(12): e08475.

Kuhlmann J, Schaefer HG and Beermann D. Quinolone Antibacterials. Chapter 11. In: Clinical Pharmacology. Kuhlmann J, Dalhoff A, Zeile AJ, (Eds.); Springer, Berlin, Germany, 1998; 127: 339-406.

Liu J, He Y, Liu D, He Y, Tang Z, Lou H, Huo Y and Cao X. Characterizing the binding interaction of astilbin with bovine serum albumin: a spectroscopic study in combination with molecular docking technology. *RSC Adv.* 2018; 8:7280–7286.

Nagasree K, Chowdary GV, Mahendra KCB, Reddy TRM, and Bhikshapathi DVRN. Design and evaluation of gemifloxacin mesylate mucoadhesive microspheres. *Der Pharma. Lett.* 2016; 8 (4): 351-360.

Paim CS, Führ F and Steppe M, Schapoval EE. Gemifloxacin mesylate: UV spectrophotometric method for quantitative determination using experimental design for robustness. *Quim. Nova*. 2012; 35:193-197.

Serafin A and Stańczak A. The complexes of metal ions with fluoroquinolones. *Russian J. Coordinat. Chem*. 2009; 35: 81-95.

Saha S, Begum R, Sultan MZ and Amjad F. *In vitro* interaction of metformin with diclofenac in aqueous medium. *Dhaka Univ. J. Pharma. Sci.* 2012; 11(2):101-106.

Salve P, Vinchurkar A, Raut R, Chondekar R, Lakkakula J, Roy A, Hossain MJ, Alghamdi S, Almehmadi M, Abdulaziz O, Auahyani M, Dablool AS, Sarker MMR and Azlina MFN. An evaluation of antimicrobial, anticancer, anti-inflammatory and antioxidant activities of silver nanoparticles synthesized from leaf extract of *Madhuca longifolia* utilizing quantitative and qualitative methods. *Molecules*. 2022; 27(19): 6404.

Tanwir A, Jahan R, Quadir MA, Kaisar MA and Hossain MK. Spectroscopic studies of the interaction between metformin hydrochloride and bovine serum albumin. *Dhaka Univ. J. Pharm. Sci.* 2012; 11, 45-49.

Turel I. The interactions of metal ions with quinolone antibacterial agents. *Coord. Chem. Rev*. 2002; 232: 27-47.

Uddin TM, Chakraborty AJ, Khusro A, Zidan BR, Mitra S, Emran TB, Dhama K, Ripon MK, Gajdács M, Sahibzada MU and Hossain MJ. Antibiotic resistance in microbes: history, mechanisms, therapeutic strategies and future prospects. *J. Infect. Public Health.* 2021; 14(12): 1750-1766.

J. Bangladesh Acad. Sci. 46(2); 213-217: December 2022 DOI: 10.3329/jbas.v46i2.60444

Journal of Bangladesh Academy of Sciences

Journal homepage: http://www.bas.org.bd/publications/jbas.html

Short Communication

The Reve's Puzzle with single relaxation of the Divine rule

Abdullah-Al-Kafi Majumdar*

Yamanote-cho 17–2, *Beppu-shi* 874-0828, *Japan*

ARTICLE INFO

Article History
Received: 29 March 2022
Revised: 31 July 2022
Accepted: 5 December 2022

Keywords: Tower of Hanoi, divine rule, Reve's puzzle, dynamic programming

ABSTRACT

This paper proposes a new version of the Reve's puzzle, allowing at most one violation of the "divine rule". Letting S(n) be the minimum number of moves required to solve the problem with n(≥ 1) discs, an scheme is given to find the dynamic programming equation satisfied by S(n). A closed- form expression of S(n) is derived.

Introduction

The Tower of Hanoi puzzle, due to the French mathematician Lucas (1883), is as follows: Given are three pegs. Initially, one peg contains $n(\geq 1)$ discs of varying sizes, in a tower (in increasing order, from top to bottom). The objective is to transfer the tower to another peg, in minimum number of moves, where each move shifts only one (topmost) disc from one peg to another peg, under the "divine rule" that, during the transfer process, no disc can ever be placed on top of a smaller disc. It is known that the total number of moves necessary is 2^n -1.

The 4-peg generalization, also called the Reve's puzzle, is due to Dudeney (1958). In its general form, the Reve's puzzle is as follows: There are $n(\geq 1)$ discs d_1, d_2, d_n of varying sizes, and four pegs, S, P_1, P_2 and D. In the initial configuration, the discs rest on the *source peg S*, in a tower. The objective is to transfer the tower to the *destination peg D*, in minimum number of moves, under the "divine rule".

There are several generalizations of the Tower of Hanoi problem and the Reve`s puzzle, for which the reader is referred to Majumdar (2012, 2013) and Hinz et al. (2018).

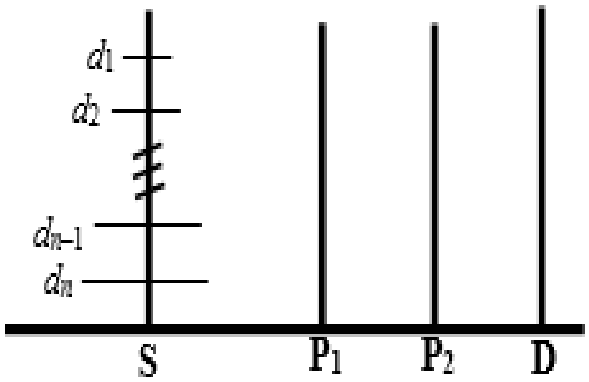

Fig.1. The initial state of the Reve's puzzle

Chen et al. (2007) proposed a variant of the Tower of Hanoi problem which permits (at most) $r(\geq 1)$ violations of the "divine rule". In the new generalization, the objective is to shift the tower from the peg S to the peg D in minimum number of moves, such that, for (at most) r moves, some disc may be put on top of a smaller disc.

A natural generalization of the problem of Chen et al. (2007) to the 4-peg case is the Reve's puzzle which permits single relaxation of the "divine rule". Thus, during the transfer process, at most once, a disc may be placed on a smaller disc.

*Corresponding author: <aakmajumdar@gmail.com>

Let $S(n)$ be the minimum number of moves necessary to solve the Reve's puzzle with n discs and single relaxation of the "divine rule". The third section derives a closed-form expression of $S(n)$, considering all possible cases. The next section gives the background materials, while some remarks are given in the final section.

Background materials

Let the minimum number of moves necessary to solve the Reve's puzzle with $n(\geq 1)$ discs be denoted by $M(n)$. Then, $M(n)$ satisfies the dynamic programming equation below (see, for example, Roth (1974), Wood (1981), Hinz (1989), Chu et al. (1991), Majumdar (1994, 2012) and Hinz et al. (2018): For $n \geq 4$,

$$M(n) = \min_{1 \leq \ell \leq n-1} \left\{ 2M(\ell) + 2^{n-\ell} - 1 \right\}, \qquad (1a)$$

with

$$M(0) = 0, \qquad (1b)$$

$$M(n) = 2n - 1 \text{ for all } 1 \leq n \leq 3. \qquad (1c)$$

Recently, Bousche (2014) claimed an analytical proof of optimality of the scheme leading to the equation (1a).

In what follows, the following results would be needed; for a proof, the reader is referred to Majumdar (1994, 2012).

***Lemma* 1:** For any $n \geq 1$,

$$M(n+1) - M(n) \geq M(n) - M(n-1).$$

***Corollary* 1:** $M(n+1) - M(n) > 4$ for all $n \geq 6$.

***Proof*:** Since for $n \geq 6$ (see Table 1),

$$M(n+1) - M(n) \geq M(7) - M(6)$$

$$= 8 > 4 = M(6) - M(5),$$

the result follows (by virtue of Lemma 1).

The solution of the optimality equation (1) is given below for reference later (for a proof, the reader is referred to Majumdar (1994, 2012), Hinz et al. (2018) and Majumdar (2021)).

***Theorem* 1:** $M(n)$ is given as below:

(1) for $s = 1, 2, \ldots$, $M\left(\frac{s(s+1)}{2}\right)$ is attained at the unique point $\ell = \frac{s(s-1)}{2}$, with

$$M\left(\frac{s(s+1)}{2}\right) = 2^s(s-1) + 1,$$

(2) for $\frac{s(s+1)}{2} \leq n < \frac{(s+1)(s+2)}{2}$, $M(n)$ is attained at $\ell = n - s - 1, n - s$, with

$$M(n) = 2^s \left\{ n - \frac{s(s-1)}{2} - 1 \right\} + 1.$$

In Theorem 1 above, ℓ is the value at which $2M(\ell) + 2^{n-\ell} - 1$ in equation (1a) is minimized. The values of $M(n)$ for some small n are given in Table 1.

Let $S_3(n)$ be the minimum number of moves necessary to solve the problem of Chen et al. (2007) with $n(\geq 1)$ discs and one relaxation of the "divine rule". Then, $S_3(n)$ is given as follows.

***Lemma* 2:** For any $n \geq 1$,

$$S_3(n) = \begin{cases} 2n-1, & \text{if } 1 \leq n \leq 3 \\ 2^{n-2} + 5, & \text{if } n \geq 4 \end{cases}$$

The problem and its solution

The problem considered in this paper is as follows: Given is a tower of $n(\geq 1)$ discs (of different sizes) resting on the peg S, with the smallest disc at the top. The objective is to shift this tower to the peg D, using the two auxiliary pegs P_1 and P_2, in minimum number of moves, under the condition that each move transfers the topmost disc from one peg to another, such that only once, some disc may be put on a smaller one, and in any of the other moves, no disc can be placed on a smaller disc.

Let $S(n)$ denote the minimum number of moves necessry to solve the problem above. The theorem below gives a closed form expression of $S(n)$.

***Theorem* 2:** For $n \geq 1$,

$$S(n) = \begin{cases} 2n-1, & if\ 1 \leq n \leq 4 \\ 4n-9, & if\ 4 \leq n \leq 8 \\ M(n-3)+10, & if\ n \geq 8 \end{cases}$$

***Proof*:** The case $1 \leq n \leq 4$ is trivial. For example, when $n = 4$, an optimal strategy is as follows: Move the smallest disc, d_1, from S to P_1, then shift the disc d_2 (from S) to P_2, next move the disc d_3 (from S) to P_1 (on top of d_1, thereby violating the "divine rule" once). Now, move the largest disc (from S) to D. After shifting the disc d_3 (from P_1) to D, move the discs d_2 and d_1, in this order, to D, to complete the tower on D. This scheme involves 7 moves.

So, let $n \geq 5$. There are three possible schemes, which are described below.

Case 1: The first scheme is as follows:

1. shift the topmost $k(\geq 1)$ smallest discs, d_1, d_2, ..., d_k, from S to P_1 (using all the available four pegs), in (minimum) $M(k)$ moves,
2. move the disc d_{k+1} from S to P_1, violating the "divine rule",
3. shift the tower of remaining $n-k-1$ discs (from S) to D, (using the three pegs available) in (minimum) $2^{n-k-1}-1$ moves,
4. transfer the disc d_{k+1} from P_1 to D,
5. finally, move the tower (of k discs) on P_1 to D, to complete the tower on it.

The above scheme requires minimum

$$\min_{1 \leq k \leq n-1} 2\{M(k)+1\} + 2^{n-k-1} - 1$$
$$= M(n-1) + 2, \qquad (2)$$

moves, where the expression in equation (2) follows from equation (1). Note that, in equation (2), $M(n-1)$ is attained at a point k with $k \leq n-2 < n-1$.

Case 2: The second scheme to follow is as below:

1. shift the topmost $k(\geq 1)$ smallest discs from S to P_1, in (minimum) $M(k)$ moves.
2. move the $n-k$ discs (remaining on S) to D, using the three available pegs, in (minimum) $S_3(n-k)$ moves.
3. finally, shift the tower of k discs from P_1 to D, in (minimum) $M(k)$ moves, thereby completing the tower on D.

The above scheme requires (minimum)

$$2M(k) + S_3(n-k) = 2M(k) + 2^{n-k-2} + 5$$

number of moves, where k is chosen so as to minimize the total number of moves. Thus, the minimum number of moves involved under this scheme is

$$\min_{1 \leq k \leq n-1} \left\{2M(k) + 2^{n-k-2}\right\} + 5$$
$$= M(n-2) + 6, \qquad (3)$$

where in getting equation (3), equation (1) has been used. Recall that, $M(n-2)$ is attained at a point k with $k \leq n-3 < n-1$. Thus, the value of $M(n-2)$ is not affected if the range of k is extended (to $n-1$) in equation (3).

Now, by Corollary 1, for $n \geq 8$

$$M(n-1) + 2 > M(n-2) + 6.$$

Thus, the second scheme is better than the first one for $n \geq 8$.

Case 3: The third scheme is as below:

1. shift the topmost $k(\geq 1)$ smallest discs from S to P_1, (in (minimum) $M(k)$ moves),
2. transfer the disc d_{k+1} (from S) to D,
3. shift the disc d_{k+2} (from S) to P_2,
4. move the disc d_{k+3} (from S) to P_1, on top of the tower of k smallest discs, violating the "divine rule" once,
5. transfer the disc d_{k+2} (from P_2) to P_1, on the disc d_{k+3},
6. move the disc d_{k+1} (from D) to P_1, on the disc d_{k+2}.

After Step 6, there are two towers on the peg P_1, namely, the tower of three discs, d_{k+1}, d_{k+2} and d_{k+3}, on top of the tower of the smallest k discs. Next, follow the steps below.

7. transfer the tower of $n-k-3$ discs, still lying on S, to D, in (minimum) $2^{n-k-3}-1$ moves,
8. move the disc d_{k+1} (from P_1) to S,

9. transfer the disc d_{k+2} (from P_1) to P_2,
10. shift the disc d_{k+3} (from P_1) to D,
11. move the disc d_{k+2} (from P_2) to D,
12. finally,shift the disc d_{k+1} (from S) to D, to complete the tower on D.

The minimum number of moves involved in the above scheme is

$$\min_{1 \le k \le n-1} 2\{M(k)+5\} + 2^{n-k-3} - 1 = M(n-3)+10. \quad (4)$$

Note that, in equation (4), $M(n-3)$ is attained at a point k with $k \le n-3 < n$.

Now, by Corollary 1, for all $n \ge 9$,

$$M(n-2)+6 > M(n-3)+10.$$

Hence, the third scheme is better than the second one when $n \ge 9$. Since for $n \ge 8$, the second scheme is better than the first one, it follows that the third scheme is the only optimal scheme when $n \ge 9$. It now remains to compare the values of $M(n-1)+2$, $M(n-2)+6$ and $M(n-3)+10$ when $5 \le n \le 8$.

Now, since

$$M(4)+2 = 11 = M(3)+6,$$

it follows that the first and the second schemes both are optimal when $n = 5$; again, since

$$M(5)+2 = M(4)+6 = M(3)+10 = 15,$$

$$M(6)+2 = M(5)+6 = M(4)+10 = 19,$$

it follows that, for $n = 6, 7$, all the three schemes are optimal; and finally, since

$$M(6)+6 = 23 = M(5)+10,$$

it follows that, for $n = 8$, the second and the third schemes are optimal. Thus, so far as the number of moves is concerned, the second scheme may be disregarded.

To complete the proof, note that, using Table 1, it may readily be verified that, for $4 \le n \le 7$,

$$M(n-1) = 4n-11,$$

so that the minimum number of moves under the first scheme is simply $4n-9$. Finally, note that, this number remains valid when $n = 8$ as well.

Thus, the theorem is established.

Table 1. $M(n)$ and $S(n)$ for $4 \le n \le 10$

n	4	5	6	7	8	9	10
$M(n)$	9	13	17	25	33	41	49
$S(n)$	7	11	15	19	23	27	35

Remarks

The purpose of the paper is to initiate the study on a new variant of the Reve's puzzle, which permits relaxation of the "divine rule". Interestingly, for the new version, the optimal value function $S(n)$ can be expressed in terms of $M(n)$ only. Therefore, Theorem 1 may be exploited to find the properties and closed-form expressions of $S(n)$. An immediate generalization is the Reve's puzzle with $r(\ge 2)$ relaxations of the "divine rule". Another problem of interest is the bottleneck Reve's puzzle, introduced by Majumdar (1996) and Majumdar et al. (1996), which is still open, though a conjecture about the solution is given in Majumdar (2013). A third generalization of the Reve's puzzle has been treated recently by Majumdar (2016).

Conflicts of Interest

The author declares that there is no conflict of interest regarding the publication of this article.

References

Bouche T. La Quartrieme Tour de Hanoi. *Bulletin Belgian Math. Soc.* 2014; 21: 895-912.

Chen X, Tian B and Wang L. Santa Claus' Towers of Hanoi. *Graphs and Combinatorics*, 2007; 23 (Supplement): 153-167.

Chu XPing and Johnsonbaugh R. The Four-peg Tower of Hanoi puzzle. *SIGCSE Bulletin*, 1991; 23(3): 2-4.

Claus N. (=Lucas, E.) La Tour d Hanoi. *Jeu de Calcul. Sci. Nat.*, 1883; 1(8): 127-128.

Dudeney HE *The Canterbury Puzzles*. Dover, 4th Edition (1958).

Hinz AM, Klavzar S and Petr C. *The Tower of Hanoi -Maths & Myths.* Springer, 2nd Edition, 2018.

Hinz AM. An iterative algorithm for Tower of Hanoi problem with four pegs. *Computing*, 1989; 42: 133-140.

Majumdar AAK and Halder A. A recursive algorithm for the Bottleneck Reve's puzzle. *Surikaisekikenkyusho Kokyuroku*, 1996; 947: 150-161.

Majumdar AAK *The Classical Tower of Hanoi Problem and Its Generalizations, Vol.* 1: *Multi-Peg Generalizations*. Lambert Academic Publishing, U.S.A., 2012.

Majumdar AAK. Some local-value relationships for the recurrence relation related to the Tower of Hanoi problem. *Proceedings Pakistan Acad. Sci.* 2016; 53(2): 187-201.

Majumdar AAK. The Bottleneck Tower of Hanoi problem with four pegs. *Proceedings Pakistan Acad. Sci.* 1996; 33(1-2): 126-127 (Short Communication).

Majumdar AAK. *The Classical Tower of Hanoi Problem and Its Generalizations, Vol.* 2: *Other Generalizations*. Lambert Academic Publishing, U.S.A., 2013.

Majumdar AAK. The generalized four-peg Tower of Hanoi problem. *Optimization*, 1994; 29:349-360.

Majumdar AAK. The Reve's puzzle revisited. *Proceedings Pakistan Acad. Sci.* 2021; 58(2): 11-18.

Roth T. The Tower of Brahma revisited. *J. Recreational Math.* 1974; 7(2): 116-119.

Wood D. The Towers of Brahma and Hanoi revisited. *J. Recreational Math.* 1981; 14: 17- 24.

J. Bangladesh Acad. Sci. 46(2); 219-221: December 2022 DOI:10.3329/jbas.v46i2.63418

Journal of Bangladesh Academy of Sciences

Journal homepage: http://www.bas.org.bd/publications/jbas.html

Short communication

Growth and yield response of Kenaf (*Hibiscus cannabinus* L.) seed production to different sowing times

Manika Rani Debnath*, Md. Maksuder Rahman and Sanjay Kumar Biswas

Agriculture wing, Bangladesh Jute Research Institute, Dhaka, Bangladesh

ARTICLE INFO

Article History

Received: 1 August 2022
Revised: 31 August 2022
Accepted: 5 December 2022

Keywords: Kenaf, Sowing time, Growth, Seed yield, Flowering

ABSTRACT

An experiment was conducted during 2020-21 at Jute Research Substation, Jashore, to study growth and seed yield response of kenaf to different sowing times. Seeds were sown from 15 July to 1 October, an interval of 15 days, as treatment variables under RCBD design with three replications. Greater seed yield was obtained from the 1st September sowing, which was at par with 15 September and 15 August sowings values. So, maximum seed production of kenaf may be ensured with optimum seed sowing between the 1st and 15thof September.

Kenaf (*Hibiscus cannabinus* L) is an important fibre crop with many medicinal values (Cheng, 2001). Kenaf seed contains dietary fibre, oil, and proteins. Anti-oxidant rich oil of kenaf seed has been emerging as an edible oil in recent times(Chan and Ismail, 2009) with high anti-cancer properties(Foo et al., 2011; Ghafar et al., 2012).

It is mainly cultivated for fibre production in our country. We need about 1500 tons of kenaf seed per year for fibre production, of which a major portion is imported from a foreign country.

Results revealed that the ranges of 1st flowering and fruiting were observed between 53 to 83 and 72 to 96 days, respectively, across the sowing dates (Fig. 1). The highest plant height was observed at 15 July 2020 sowing (2.65m), which was statistically identical with 1 September sowing (2.46m) and lowest plant height was observed (1.71m) during 1October sowing (Table1). Agbaje et al. (2011) notice such a plant height trend. The highest pod plant^{-1} was observed at 1 September sowing (32.77) and statistically at par with 15 September, 15 August, and 1 August sowings. The lowest value (21.03) was observed at 1 October 2020 sowing, similar to 15 July sowing. Different time sowings had maximum seeds plant^{-1} (17.83-19.70) except lowest value with sowing 15 August. But a maximum 1000-seeds weight was recorded from 1 August sowing. Elevated seed yield was noted on 1 September (1897.20 kgha^{-1}),which was statistically identical to its 15 days earlier and 15 days late sowing still, the maximum yield values were very closer with 1 September and 15 September sowings. A similar finding was noted by Muchow (1980) with kenaf. Radiation during the reproductive stage was significant from a yield point of view for the mungbean crop (Rachaputi et al., 2015), which can be optimally captured by the plants when they are timely sown. Thus dry matter content of the plant becomes higher to partition it into reproductive units, especially the number of pods obtained in kenaf plants (Muchow and Wood, 1983).

*Corresponding author: <Manika0074@yahoo.com>

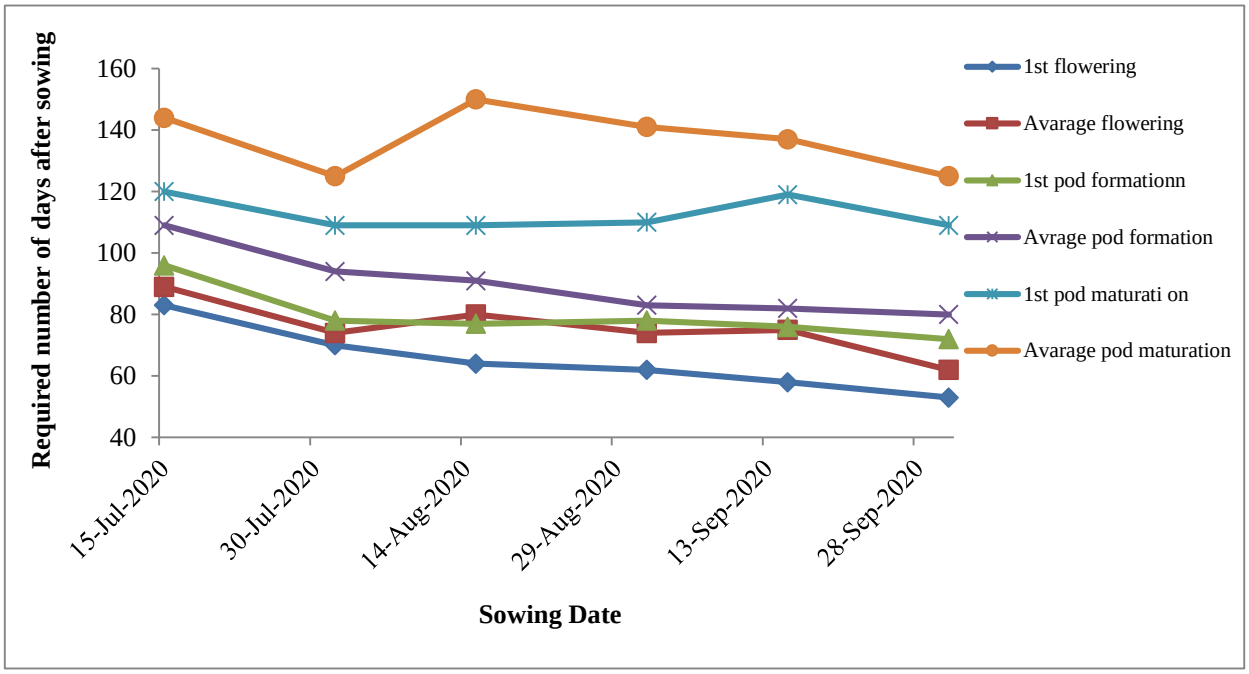

Fig. 1. Timeline for reproductive phenology of kenaf seed production

Table 1. Growth and seed yield-related parameters of Kenaf at different sowing times

Sowing Date (in 2020)	Plant Height(m)	Pods Plant^{-1}(No.)	Seeds Pod^{-1} (No.)	TSW(g)	Seed Yield (kg/ha)
15 July	2.65	24.13	19.70	25.44	1511.10
1 August	2.32	28.80	18.20	26.07	1277.80
15 August	2.34	31.00	14.20	24.50	1775.00
1 September	2.46	32.77	17.83	23.31	1897.20
15 September	2.22	31.93	18.27	22.39	1847.20
1 October	1.71	21.03	18.20	22.90	1619.40
LSD $_{0.05}$	0.22	5.70	2.25	0.50	200.17
CV (%)	5.47	11.09	8.50	1.12	6.65

TSW= Thousand seed weight

It may be concluded that the first fortnight (1 to 15) of September sowing is optimum for the maximum seed yield of the kenaf crop.

Authors contribution

MRD designed and executed the experiment, analyzed data statistically, and wrote the manuscript. MMR helped to get support for conducting the experiment. SKB helped with writing the manuscript. All the authors read the article carefully.

Conflict of Interests

The authors declare that there is no conflict of interest.

References

Agbaje GO, Aluko OA and Olasoji JO. Effect of plant spacing on seed yield and yield components in kenaf (*Hibiscus cannabinus*) variety, Ifeken 400. *Afr. J. Plant Sci.* 2011; 5(12): 718-721.

Chan KW and Ismail M. Supercritical carbon dioxide fluid extraction of Hibiscus cannabinus L. seed oil: A potential solvent-free and high anti-oxidative edible oil. *Food Chem.* 2009, 114(3): 970- 975.

Cheng Z. Kenaf research, products and applications in Japan (in Chinese). *Plant Fiber Produc.* 2001; 23(3): 16-24.

Foo JB, Yazan LS, Chan KW, Tahir PM and Ismail M. Kenaf seed oil from supercritical carbon dioxide fluid extraction induced G1 phase cell cycle arrest and apoptosis in leukemia cells. *Afr. J. Biotechnol*. 2011; 10(27): 5389-5397.

Ghafar SAA, Yazan LS, Tahir PM and Ismail M. Kenaf seed supercritical fluid extract reduces aberrant crypt foci formation in azoxymethene-induced rats. *Exp. Toxicol. Pathol*. 2012; 64(3): 247-251.

Muchow RC and Wood LM. Effect of sowing on the growth and yield of kenaf (*Hibiscus cannabinus*) grown under irrigation in tropical Australia. I. Phenology and seed production. *Field Crops Res.* 1983; 7: 81-90.

Muchow RC. Effect of plant population and season on kenaf (*Hibiscus cannabinus* L.) grown under irrigation in tropical Australia.III. Seed yield and stem yield at maturity. *Field Crops Res.* 1980; 3: 27-32.

Rachaputi RCN, Chauhan Y, Douglas C, Martin W, Krosch S, Agius P and King K. Physiological basis of yield variation in response to row spacing and plant density of mungbean grown in subtropical environments. *Field Crops Res.* 2015; 183:14-22.

INSTRUCTION FOR AUTHORS

The Journal of Bangladesh Academy of Sciences is published four times a year in March, June, September and December. Original research articles, review articles, and short communications of high standards of all branches of Science and Technology are considered for publication in this journal. Review articles are generally by invited authors; however, the Editor welcomes suggestions of potential topics and potential authors.

The following instructions must be followed while preparing the manuscript intended for publication in this journal:

1. **Research Article:** Manuscripts should be concise and consistent with the style of the journal. The manuscript must be typed using Times New Roman font, size 12 on A4 size page, and wide (1 inch) margins on all four sides. The main text must be typed in a two-column format with 1.5 spacing, and for full papers, it should not exceed 10-20 typed pages, including figures, tables, and references. In general, an article may contain the following sub-titles in sequence: **Title, Abstract, Keywords, Introduction, Materials and Methods, Results and Discussion, Acknowledgement (**if any), and **References.**

A. Title: The first page of the paper, the title page, should have the title and the names of the authors. The title should be brief and specific. Abbreviations and formulae should be avoided where possible. The next line in italics should be the authors' affiliation addresses (where the actual work was done) below the names. Indicate all affiliations with a lowercase superscript letter immediately after the author's name and in front of the appropriate address. The corresponding author, along with email address, should be indicated at the footnote with a proper asterisk.

B. The second page should carry the Title of the paper, Abstract, and Keywords. Author(s) name must not be typed on this page.

(i) Abstract: It should not exceed 150 words and should briefly state the purpose of the research, the significant results, and meaningful conclusions. Nonstandard or uncommon abbreviations should be avoided, but if essential, they must be defined at their first mention in the abstract itself.

(ii) Keywords: Immediately after the abstract, provide a maximum of 6 keywords.

C. The next pages (a maximum of 15 printed pages), will contain the main text of the paper.

(i) Introduction: It should be concise and relevant to the objectives of the study. The importance of the research work described should be pointed out. An appropriate review of the current literature should be made to identify the frontier of existing knowledge and point out the need for further work. The knowledge contributed to the study should be mentioned.

(ii) Materials and Methods: Materials used should be mentioned precisely along with their sources and any pre-treatment undertaken.

The description of methods must be brief but clear enough to enable a reader to reproduce the results. References must be considered sufficient for methods described in earlier publications: only relevant modifications should be described.

It is recommended that authors use the nomenclature and symbols adopted by IUPAC document UIFII (S.U.N. 65-3) 1965, symbols, units, and nomenclature in Physics or by IUPAC Manual of Physiochemical symbols,

Terminology and similarly for other disciplines.

(iii) Results and Discussion: This section should include descriptions of results obtained with the help of figures, tables, graphs, and photographs as may be necessary. Tables should have a descriptive title. Large and cumbersome tables should be avoided. Figures and graphs should be prepared and should be properly labelled with bold solid lines such that no further size reduction will be necessary. The paper should contain a minimum number of **Tables, Graphs,** and **Figures.** The same data should not be depicted using both tables and figures. The photographs are to be submitted in JPEG format.

The discussion should include thorough analysis and interpretation of results, and comparison with existing relevant published results, if any, and self-evaluation of the new knowledge contributed, avoiding extensive citations and discussion of published literature.

(iv) Conclusions

The study's main conclusions may be presented in a short Conclusions section, which may stand alone or form a part of the Results and Discussion section.

(v) Acknowledgment: The following support for the research work should be acknowledged:

- Funding by any agency;
- The use of instruments in a laboratory other than those of the authors;
- Individual's help during the research (e.g., providing an interpretation of results, language help, writing assistance, or proofreading, etc.).

(vi) Author contributions

For transparency, we encourage authors to submit an author contribution statement outlining each author's contributions to the paper. The authors should have participated sufficiently in the work to take public responsibility for appropriate portions of the content.

(vii) References and Text Citations:

In the text, references should be cited within brackets quoting the first author's surname followed by et al. if necessary and the year of publication in the appropriate place, e.g. (Bhuiyan, 2020), Khan et al. (2021) or (Khan et al., 2021). In the case of only two authors, surnames of both need to be mentioned, e.g., (Khan and Rahman, 2021). A semi colon should separate two or more references when putting within the same bracket. At the end of the manuscript, references should be listed and arranged alphabetically according to the first author's surname according to the style described below:

(a) Journal article:

In each reference, names of all authors' will have to be given in the same style, e.g., surname followed by initials, lumped together without using a full stop. The names will be followed by the full title of the article and the journal's abbreviated title (in italics). The year of publication will be given next, followed by volume number (issue number) and page ranges. For abbreviations of the names of journals, authors are advised to follow the *World List of Scientific Periodicals.* For online publications, the URL address must be given. Note: Please list ALL authors' names in the list of references, do not use (et al.). **Examples:**

Islam S. The Induced Morphological and Root Anatomical Changes in Lentil. *J. Bangladesh Acad. Sci.* 2019; 43(2):107-112.

James BD and Bennett DA. Causes and Patterns of Dementia: An Update in the Era of Redefining

Alzheimer's Disease. *Annu. Rev. Public Health;* 2019; 40: 65-84.

Moniruzzaman M, Khatoon R and Qamruzzaman AKM. Influence of Plant growth Regulators on Vegetative Growth, Sex Expression and Yield of Summer Bottle Gourd. *Bangladesh J. Agril. Res*. 2019; 44(4): 577-590.

(b) Book or Chapter in a Book:

The place and name of the publisher, year of publication, will have to be given in addition to the name of the author(s), the title of the book (in italics), edition number (if not first), and the number of pages. In the case of an article or chapter in a book or proceedings of a conference, author(s) name and the title of the article or chapter will be followed by the title of the book (in italics), the names of the editors of the book, edition number (if not first), the place and name of the publisher, year of publication and page or page numbers of chapter. **Examples:**

Book:

Carlson BM. *Human Embryology and Developmental Biology*. 4th ed. St. Louis: Mosby; 2009. p. 541.

Cassese A, Acquaviva G, Fan M and Whiting A. *International Criminal Law: Cases and Commentary*. Oxford University Press; 2011, p. 600.

Chapter in an edited book:

Muhammad HFL and Dickinson KM. Nutrients, energy values and health impact of conventional beverages, Chapter 3. In: *The Science of Beverages, Volume 12: Nutrients in Beverages*. Grumezescu AM, Holban AM, eds., Elsevier Science; 2019; pp. 77-109.

Balsam KF, Martell CR, Jones KP, Safren SA. Affirmative cognitive behavior therapy with sexual and gender minority people. In: *Culturally Responsible Cognitive Behavior Therapy: Practice and Supervision*. Iwamasa GY, Hays PA, eds., 2nd edition, American Psychological Association. 2019; p. 287-314.

(c) Proceedings of a Conference:

Luca J and Tarricone P. Does emotional intelligence affect successful teamwork? In: *Meeting at the Crossroads*. Kennedy G, Keppell M, McNaught C (eds.), Proceedings of the 18th Annual Conference of the Australasian Society for Computers in Learning in Tertiary Education, 2001 Dec 9-12; Melbourne: Biomedical Multimedia Unit, The University of Melbourne; 2001. pp. 367-376.

(d) Reports:

Bangladesh Bureau of Statistics (BBS). Population census - 2011. Preliminary report. Bangladesh Bureau of Statistics, Ministry of Planning, Government of the People's Republic of Bangladesh, Dhaka, 2011.

Rowe IL and Carson NE. *Medical manpower in Victoria. East Bentleigh (AU)*: Monash University, Department of Community Practice; 1981. p. 35. Report No.: 4.

2. **Short communication:** Important research findings that may initiate further research in the relevant field may be published in the form of a short communication. This should not exceed three printed pages (900 words), including Graphs, Tables, and Figures. The presentation should be continuous and paragraphed, i.e., without headings like Introduction, Materials, and Methods, etc. A short communication paper should have an **Abstract** containing the gist of the article and should not exceed 60 words, followed by **Keywords.**

3. **Declarations:** While submitting, the corresponding **a**uthor will have to make a declaration mentioning the laboratory/laboratories in which the work was carried out and certifying that the contents of the paper were not published before or submitted for publication in any other journal and that all the co-authors have given their consent for the article to be considered by the Editorial Board for publication in the Journal of Bangladesh Academy of Sciences.

Declaration of conflicting interests

The corresponding author must provide a formal conflict of interest statement for all authors disclosing any financial and personal relationships with other people or organizations that could inappropriately influence (bias) their work. If no conflict exists, please state that 'The author(s) declare(s) that they have no conflicts of interest regarding the publication of this article.'

4. The manuscript should be submitted in pdf or MS Word or LaTex files through online at www.bas.org.bd/publications/jbas.html. Equations generated by using Math Type or Math ML should be incorporated in the text.

   Soft copies of manuscripts with tables, graphs, illustrations, and photographs placed correctly in a printable format are to be submitted. Authors wishing to publish coloured schemes/diagrams/ sketches/photographs in their papers need to pay for the printing charges of one format. This will be charged only after the acceptance of the manuscripts for publication in the JBAS.

   The manuscript submitted should also contain a separate list of tables, figures, illustrations, photographs, and sketches with appropriate captions.

5. Electronic versions of final galley proofs will be sent to authors. No alteration in the title or additions in the text is desirable at this stage.

6. All correspondence for publication should be made on www.bas.org.bd/publications/jbas.html to the **Editor, Journal of Bangladesh Academy of Sciences, National Science and Technology Complex, Agargaon, Dhaka 1207.**

N.B.: No paper will be accepted for publication if it does not conform to the style specified for the journal and approved by the Editorial Board, which has the authority to accept or reject the manuscript of a paper submitted without showing any reason.